JCU ePrints

This file is part of the following reference:

Shankland, Paul (2007) ***From Jets to GEMSS*: pan-spectral detection, observation and characterization of the M-Dwarf Exoplanet System Gliese 876 - and beyond. Transit photometry, radial velocity, and millimeter interferometry to constrain and characterize the nearest multiple planet system.*** **PhD thesis,**
James Cook University.

Access to this file is available from:

http://eprints.jcu.edu.au/10347

JCU
JAMES COOK UNIVERSITY

Chapter 1: Introduction

Understanding extrasolar planets in the context of mankind's role in the universe has become a recent, newsy endeavor as the number of planet detections surpasses 268[6]. However this prevalence has roots in man's ponderings throughout history. A short recapitulation of this discovery history will underscore the thinking process, and help to place the exoplanet transit work here, into the larger context. From there, methodologies, execution, results, and interpretations are covered for the whole of the work performed. Starting with the question of heritage, this thesis answers the question "why?", and then moves on to answer "what", "how", "where", and "when".

Detection of exoplanets has become a fast-growing field since planets were identified about pulsar PSR1257+12 in 1992 (Wolszczan and Frail, 1992). As inferred, however, the interest has been a philosophical and logical pursuit for more than two millennia. A review of these kinds of prominent historical touchstones will be introduced as a first precursor to the current work. Before the Solar System models of Copernicus, Galileo, Kepler and Newton were formulated, questions had been posed regarding whether Earth is a one-of-a-kind entity, and whether its characteristics, indeed habitability for humans, were exceptional. Those questions still cross every person's mind at some point in their life. Today, seeking these answers has finally become an empirical enterprise. Today's science is still based on the logical foundations posited by the 'exo-forefathers', solar system 'traditionalists', and even the progress of instrumentalists (current progress would be impossible without charge-coupled imaging arrays, for example).

From an astronomical perspective, broad treatises have covered decadal exoplanet developments (Perryman, 2000), while prolific additions to the knowledge base can be found in the refereed literature. Of the various methods used to detect exoplanets, photometric detections have particular accessibility and utility, and are the basis for this initial study. Beginning with system-tuning using the now-celebrated transiting exoplanet system HD 209458, the study expanded to a search for any transits about the red dwarf Gliese 876 (or Gl 876)[7], both from use of novel airborne instrumentation as

[6] A current count is maintained at http://exoplanet.eu/
[7] While this star is also found in the later, well-known Gliese-Jahreiß (GJ) catalog, the original "Gl" abbreviation is used throughout this thesis because the GJ catalog is known to be preliminary. As well,

well as using more traditional, ground-based venues. Leveraging a known ~3-hour transit, the flux drop of 1.6% or drop of ~V = 0.02 caused by HD 209458's planet "b" was measured in order to determine the photometric capabilities of a new airborne system called the Tactical Observatory for PHotometry of Astronomical Targets, or TOPhAT. TOPhAT and its terrestrially-based variant, TIP-TOPhAT were then unleashed on a primary candidate Gl 876. Initially a flux detection drop of 0.16 ± 0.04 magnitudes from 2003 Oct. 27.9583 to 2003, Oct 27.9972 (JD 2452940.4583 to 2452940.4972) was identified (figure 2), which precipitated the requirement for follow-up optical and radio validation.

Fig 2: 2003 flux detection for Gl 876 with TIP-TOPhAT; see chapter 5 for details

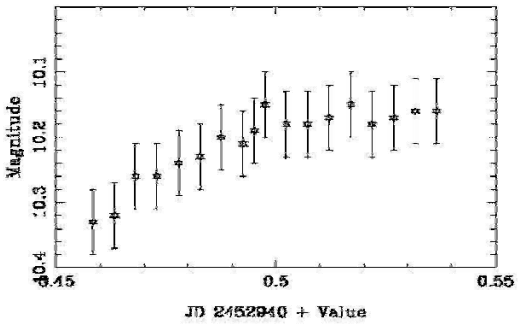

The first follow-up was performed using a large, distributed campaign, with further assessment of Gl 876 via its spectral radial velocity curves. These were done in order to determine whether a transit exists, and then to constrain the orbital dynamics of the system in mass and inclination. Any result also has implications for planet formation theory. Then, in the wake of the optical research, a study of the potential dust disk was also performed at millimeter wavelengths, also in order to understand any inclination, but moreover the dust, even extrasolar system mass. All observations also produced null but constraining result with good confidence.

The distributed photometric network also revealed its own novel potential. Unlike broad survey schemes that other teams have undertaken, this study blended a targeted search with a characteristic-independent survey which could more readily provide detections. The increased likelihood of detecting transits involving M dwarfs was also revealed. The advantage of an effectively distributed collection of modest aperture telescopes was validated through global campaigning, which connected independent colleges, small observatories, and extant teams like TransitSearch and American Association of Variable Star Observers (AAVSO). Following the Gl 876 campaign and radio (dust)

---

the first refereed paper produced from these studies (herein, Chapter 6) was published in *Astrophysical Journal*, whose staff wished the less popular, yet more proper Gl convention be used. For continuity in the thesis, the Gl convention is maintained throughout.

follow-up with the Very Large Array (VLA) and the Australia Telescope Compact Array (ATCA), the efforts to detect transits were indeed broadened, and in the targeted survey paradigm, the Global Exoplanet M-dwarf Search-Survey (GEMSS) was born.

Developing a bias-free but targeted search poses a number of challenges, but fits well in the current scheme to detect and understand those planets -- which exist outside the Solar System. In particular, photometry offers capabilities that can deduce the planetary radius from transit depth using the ratio of planet-stellar radii. Moreover, photometry is responsive to detecting bodies in the habitable zone.

Other means must be used to overcome photometry's weaknesses. Foremost, the orbital plane must be nearly edge-on to detect a transit flux, which produces a generally low (of order 1%) geometric probability of a transit occurring from any one vantage point. While these odds seem low, they are overcome with by one's ability to 'stare' at the target, and to select targets whose orbits are closer-in (where slightly off-edge-on inclinations still occult some portion of the star's observed disk). Close-in orbits also mean more frequent transit opportunities, and with red dwarfs, such an orbit is still likely to be in the dimmer parent's habitable zone. Such odds are statistically worth the risk of lost observing time, if anything because null detections still provide important, constraining results.

Selecting small-radius parent stars like red dwarfs, while intrinsically dim, also allows greater transit depth to go with the merits of networked, small-aperture photometric coverage. M-class stars are at >75% of the Galactic population (Mirzoyan, 1995). This fact makes such a population not only good 'hunting grounds' for detections, it aids in a more accurate galactic census of the exoplanetary makeup by understanding "what" and "how many" are around so many of the Galaxy's constituents. It also begins to lay statistical groundwork to improve the accuracy of theories of planet formation by increasing the *n* number of detections. The remaining population in the Galaxy is found to be ~5% for the K-class, ~3% for the solar-like G-class variety, ~3% for F-class stars, and <1% for the remainder (O, B, and A). All types might support planets, but the red dwarf's numbers and ratios make terrestrial planet detections first likely there.

While precision photometry appears to be more accessible to modest apertures (unlike other detection methods), it can also be 'confused' by phenomena, which make the observational process fraught with the potential for false detections. Alternate photometric phenomena include grazing/occulting eclipsing binaries, star spots, cataclysmic variability, and blended eclipsing binaries with deep eclipses. Significantly, working so close to the noise floor requires special observational rigor and a lot of on-target time, which may or may not eliminate pervasive false positives.

Transit detection is also limited in utility by the periodicity/size relation of a potential planet's transit, especially if an instrument is performing near its limiting magnitude. While this may limit its fidelity at the faint end (ability to detect above a noise floor), a distributed network helps to improve temporal fidelity (ability to cover the characterization of the dynamical events more completely). The reasons will be made clear in the opening rounds of this exposition that follow. The latter is aimed at overcoming the photometric weakness of low probability due to typical geometry. One challenge for all detection methods is actually discerning the type and composition of notional orbiting bodies, which may be brown dwarfs or dimmer red-dwarf companions instead of Jovian or terrestrial planets.

Photometry's weaknesses are largely overcome by combining it with other methods of observation. Imaging a debris disk allows the confirmation of the system mass and inclination[8]; the slope of the radial velocity curves themselves as well produces indications of a transit potential via the Rossiter-McLaughlin effect described shortly. Both methods when combined can provide clues to planet density, composition, and variations can even cull details about potential atmospheres. Such a combination with radial velocity (RV) was used to compliment the initial photometry of Gl 876. Despite the hurdles, a number of photometric transit studies have published their capture of the flux variations for now 34 exoplanets (and growing[9]). The study of Gl 876 contributes to understanding such dynamics for one system, and it affords the opportunity to devise methods to study the red dwarf population at large.

[8] This assumes the exoplanet(s) and disk are largely co-planar.
[9] The number of transit detections is kept current at: http://www.exoplanet.eu/catalog-transit.php

To reconstruct the basis, methods and results of the study of Gl 876 and its foray toward the larger M dwarf population with the Global Exoplanet M-dwarf Search-survey (GEMSS), this thesis is divided into nine chapters.

Chapter 2 reviews the heritage underpinning recent and current studies and explains the basics of detection techniques currently available. This chapter then elaborates on photometry, transits and dust detection methods. It concludes with the rationale for choosing red dwarfs and Gliese 876 in particular.

Chapter 3 discusses visual photometry in some detail to provide a basis for later discussions. This chapter elaborates upon errors, noise, and selection-effects associated with transit photometry.

Chapter 4 covers the instrumentation setup, operation, techniques and limitations – for video photometry using TOPhAT and TIP-TOPhAT, conventional photometry, distributed campaigns, millimeter radio instruments (VLA and ATCA), and Phase One of the red dwarf search-survey GEMSS.

Chapter 5 describes the initial optical flux observation and provides dynamical considerations for why detections were not found in subsequent efforts. This chapter reviews the initial Gl 876 observations, which led to the distributed collaborations discussed next.

Chapter 6 recapitulates the gamut of the initial optical transit work as published in the *Astrophysical Journal.* This includes the global, distributed Gl 876 campaign to detect follow-up transits reported in Chapter 5, as well radial velocity confirmation of any transits (the appendices elaborate further on implementing RV confirmations).

Chapter 7 explains GEMSS Phase One as an initial analysis of the viability of a larger, 3σ distributed campaign that targets higher-probability red dwarfs. The focus is on the initial results for two of thirteen targeted red dwarfs and how this influenced setup for a future phase two from a list of 42 candidates (the lists are found in the appendices).

Chapter 8 recapitulates the millimeter radio studies of Gl 876 with the VLA and ATCA as provided in *Astronomical Journal* for publication.

Chapter 9 summarizes the results and posits implications for constraints on parameter space for Gliese 876 and red dwarfs. The chapter concludes by noting the author's plans for future study.

The appendices offer the reader support data for Gliese 876, its planets, RV reduction methodologies, physical identities and constants, target lists for GEMSS, related future research underway, background references, and a bibliography.

CHAPTER 2: Background

A review of the history and current state of extrasolar research will lay a foundation for the research described in the remainder of this thesis. As with other fields, third millennium exoplanet astronomers may use a wide variety of complementary observational tools, some recently crafted, others steeped in historical development. First the foundation must be laid for defining what a planet is. So, what is a planet? Exoplanet discovery, (particularly for transiting planets) must include an evaluation of what a planet is because low mass objects that can confuse any detection process may have similar attributes, such as size or occultation profile. In addition, discoveries have forced a re-evaluation of what a Solar System planet is, and that result has an effect on how an exoplanet is defined. In most cases the conflicts arise from gray areas in terms of planetary genesis, orbit and size. For the reader who is interested in the International Astronomical Union's (IAU) interpretation of what a Solar System planet should be defined as, the IAU 2006 Prague General Assembly (GA) XXVI Resolution 5A is interesting reading[10].

For the purposes of identifying exoplanets in this research, a simple definition is used. Here, extrasolar planets are simply considered to be opaque bodies that reflect light from their parent stars and whose internal nuclear processes do not support fusion. Practically speaking this comprises objects that are less massive than 13 Jupiter masses (or 1.9×10^{27} kg), and are of some gas or rocky makeup. The more massive brown dwarfs are of course not included as planets. As a result, the Working Group on Extrasolar Planets (WGESP) of the IAU standardized their own IAU definition[11] of a planet. Planets are defined by WGESP as objects with true masses below the limiting mass for thermonuclear fusion of deuterium (thought to be 13 Jupiter masses for objects of solar metallicity); and that these orbit stars or stellar remnants, regardless of formation mechanism. They are not free-floating "sub-brown dwarfs in young star clusters. Generally speaking, WGESP intended to align Solar System masses to extrasolar ones. For the WGESP definition, $M/M_{\odot} > 0.080$ are stars, $0.015 < M/M_{\odot} < 0.080$ are brown dwarfs, and $M/M_{\odot} < 0.015$ are [exo]planets. This particular definition is used for the purposes of this thesis.

The current understanding for exoplanets can be base-lined with these 'going-in' facts, which were also the foundation of this study. Exoplanet astronomers believe the following are true:

---

[10] See http://www.iau.org/iau0601.424.0.html, and note in particular Gingrich's commentary for the proposed Resolution 5. Subsequently, see http://www.iau.org/iau0603.414.0.html for the final definition, resolution 5A.GA Proceedings are forthcoming; until then, see now Resolution B5 at http://www.iau.org/fileadmin/content/pdfs/Resolution_GA26-5-6.pdf and Soter (2007).

[11] Like IAU GA Resolution 5, the WGESP definition has yet to be formalized, but a working variant is at http://www.dtm.ciw.edu/boss/definition.html

(1) Metal-rich stars seem to have planets more often, and those have more planets per parent star (see Robinson (2006) -- this could be an observational bias, discussed in later chapters).

(2) Many exoplanet orbits are very eccentric (Ford Quinn & Veras, 2008).

(3) multiple-planet systems exist (e.g., Goździewski, Konacki & Maciejewski, 2006).

(4) Some binary and triple star systems keep close-in planets (Eggenberger et al., 2008)

(5) Neptune-mass planets are now being found (e.g., Bonfils et al., 2005)

(6) A few terrestrial extrasolar planets are inferred (Rivera et al., 2005), and one (Gl 581; Udry et al., 2007) has been said to be detected.

(7) The radii of small stars, brown dwarfs, giant planets are all confusingly, order-of-magnitude similar, particularly when assessed at current levels of detection fidelity (Ksanfomality, 2004)

(8) Zones of habitability (or regions where liquid water could exist) are found in many places previously unexpected, such as about exo-moons, 'faint-cool stars', and, for tidally-locked stars with atmospheres (Kasting, 1998; and Joshi et al., 1997)

(9) Critical instrumental improvements[12] (subject to Moore's Law[13]) have allowed a geometrically increasing flood of exoplanet detections for fifteen years and both are expected to continue this rate (Perryman, 2001, updated 2007)

(10) Exoplanet observation is potentially rife with observational bias (Kiss &Bedding, 2005; Fridlund, 2008; Benz et al., 2006; and O'Toole, Tinney & Jones, 2008)

As well, it is generall agreed that, "absence of evidence clearly was not evidence of absence" (Sagan and Druyan, 1996). Yes, the Fermi-Pasta-Ulam Paradox asks a good question, that if

[12] hardware advances include: focal plane array designs (primarily advances in charge-coupled devices), computer processing power, optical materials and ray-traced design, robotic capabilities and automation, instrument stability and precision (in fabrication and operation), information transfer rates and bandwidth, networking and synthesis of distributed information, human interface/presentation/efficiencies, more complete wavelength access, broader access to favorable instrument environments, ability to increase complexity, size (nanotechnology/ fabrication, information density, and portability) and other software capabilities (S/N improvement, improved numerical methods, modeling, statistics, accounting effects/biases, efficient processing, parallel/ threaded processing, improved computer languages, interfaces).

[13] See http://www.intel.com/technology/mooreslaw/index.htm.

..."they exist, where are they?" (Ford, 1992) While this thesis is not a discourse on astrobiology and beyond, the exoplanet astronomer should answer the Fermi question to him/herself carefully. As a caveat, this list helps to characterize the current state of the research, but each listing cannot be assumed to be a universal truth, but more a 'progress report', based on incomplete knowledge of all the biases and study foci.

One should bear in mind the current detection sensitivities and the ability to make empirical exoplanet detections, and the biases in existing and developing searches. In that regard, claiming any minimally-constrained survey will be imminently successful in the near term seems to be more an inspiration and less of a practical optimization. Bias is inevitable to some extent anyway, and in the end every survey is truly a variant of a categorical search. While any census does need a lowest-possible biase, the research here instead *opens doors* for such broad surveys. Anchoring the data with initial detections helps to blaze paths for future discovery and the censuses which follow. So narrowing this path to improve the hard-work-Edisonian odds (Hughes, 1977) is the basis for this thesis' culmination and future research, *vis-à-vis* the GEMSS Project.

Before this current state of knowledge, though, a rich heritage existed of astronomers and philosophers alike deducing the existence of these potential other-worlds. Such fore-knowledge is worthy of review, and follows next.

Section 2.A. A Brief Review of Exoplanet Discovery

The epochal founder of the scientific method, Epicurus, wrote the following passage in a letter to Herotodus, well more than two millennia ago (341-270 BC), in what captures a timeless sentiment as regards the notion of worlds beyond Earth:

> …There are infinite worlds both like and unlike this world of ours. For the atoms being infinite in number, as was proved already, are borne on far out into space. For those atoms, which are of such nature that a world could be created out of them or made by them, have not been used up either on one world or on a limited number of worlds, nor again on all the worlds which are alike, or on those which are different from these? (Bailey, 1926).

This perception was in fact one of the tenets held by Greek atomists of that distant time (among them Leucippus and Democritus). Unfortunately, their perceptions were avant-garde for the time, and particularly counter to notions held by Aristotle's and his geocentric model. Aristotle proclaimed that *There cannot be more worlds than one (*Aristotle 384-322 B.C.), a belief that

held sway for two thousand years. A possibility of a plurality of worlds re-emerged as a theory during the Renaissance, and was returned to an atomist-like heliocentric perspective by Nicolaus Copernicus in 1543. Also during this time, heliocentric philosopher Giordano Bruno (1548–1600) purported that infinite stars must therefore harbor infinite terrestrial worlds. In De L'infinito Universo E Mondi, he contends:

> There are countless suns and countless earths all rotating around their suns in exactly the same way as the seven planets of our system . . . The countless worlds in the universe are no worse and no less inhabited than our Earth. (Dick, 1993; Singer, 1950; Vatican Secret Archives, 1597)

Unfortunately he fell prey to the Inquisition, and Bruno was burned at the stake for such declarations, and for those denying Divinity.[14] Even Galileo Galileus Linceus (1564–1642), who possessed more obvious empirical data of other worlds (G. Linceus, 1661) was threatened as an apostate. However Galileus's astronomical spyglass of 1609 was the first significant practical ("instrumental") step toward exoplanet detections of today (G. Linceus, 1610).

Of course, understanding those planets within our Solar system was of first order. Beyond the known visible ones, the outer discoveries include Uranus by William Herschel in 1781, Neptune by Galle and d'Arrest in 1846, and Pluto by Tombaugh in 1930 (Hoskin, 1989)[15]. Of course a litany of minor planets, moons and bodies round out the population of bodies which populate our own solar system. These set the stage for asking what other stars than the Sun might harbor similar (or different) systems.

Christian Huygens (1629-1695) seems to be the first to give an accounting of a real search for exoplanets (Schneider, 1999). Assuredly other, earlier exoplanet searches also existed, though such documentation for these proves to be extremely scarce. The first modern attempt to validate the existence of an exoplanet was performed by astronomer Peter van de Kamp[16] in his protracted (1938-1962) plate studies of the astrometric wobble in Barnard's Star. This M4 dwarf was discovered by Edward E. Bernard in 1916 as a nearby (1.83 pc), old (8-12 Gyr), high proper-motion (nearly 10.3 arcsec yr^{-1}), dim (V = 9.57) flare star in the constellation Ophiuchus (Bernard, 1916; van de Kamp, 1969, 1982). Initially, van de Kamp claimed detection of a 1.6-

---

[14] More recent scholarship suggests that he was not burned at the stake for declaring the plurality of the worlds or denying a God, but was burned because he might have been a spy, or even a fraud (Bossy, 2002).

[15] As previously noted, the 2006 IAU definition of planet has only recently relegated Pluto to dwarf planet status amongst Trans-Neptunian Objects (TNOs), see Resolution 6A at http://www.iau.org/iau0603.414.0.html

[16] Assisted by USNO director and astrometrist Kaj Strand

Jupiter-massed planet, which was later revised to two planets, of 0.7 and 0.5 Jupiter masses, respectively (Trimble, 2004). Despite numerous attempts, his assertions remain unconfirmed by others despite various (perhaps insufficiently comprehensive) attempts. Many attribute his result to instrumental effects. During the same period, Otto Struve paved the way for another methodology, which would result in for the first confirmed detection of a planet detection (in a main sequence system) short of half a century later. His proposal was to detect planets by their Doppler-shifted, spectral radial velocity signatures (Struve, 1952). As well, a number of astrobiologists and SETI-genre scientists (e.g., F. Drake, C. Sagan, G. Coconni, P. Morrison, G. Schiaperelli, P. Lowell, J. Tartar) have offered additional means to detect other worlds with the more adventurous goal of discerning sentient life upon them (Basalla, 2006; Tartar, 2001; Dick, 1996[17]). In depth review of these efforts is beyond the focus of this thesis.

Subsequent to van de Kamp, a number of teams have claimed the title of discoverer of the first known exoplanet. In 1988, Campbell, Walker, and Yang (1988) announced an exoplanet they found orbiting Gamma Cephei that was met with general skepticism owing to their detection limits[18]. In 1991 LaLande 21185 showed odd proper motions that were considered possible exoplanet perturbations, but follow-up observations have not supported that conclusion. But it was not until the 1990's that the existence of extrasolar planets was to be proven through confirmation. With the advent of pulsar timing techniques the prior decade, Aleksander Wolszczan and Dale Frail proclaimed finding exoplanets as small as Earth-mass through such timing (Wolszczan & Frail, 1992, 1994). Even though Campbell's group has vied for first-planet honors, Wolszczan's is popularly known to have that first detection. As it was about a pulsar the detection seemed to garner less attention from the press at the time.

Attention from the press changed with a detection about a main sequence star. In October 1995, Michel Mayor and Didier Queloz carried out a methodical radial velocity survey of 142 local stars, and from this, detected of the first extrasolar planet orbiting a solar-type (G5IV) star, 51 Pegasi. Doppler methods having achieved ascendancy over other detection capabilities by 1996, Geoff Marcy and Paul Butler themselves used radial-velocity (or RV, which is the detection of a periodic Doppler shift of a star's spectral lines, attributed to mass asymmetry) for numerous detections. In that year they began a study of 120 candidates, and found five more exoplanets. Among these was the Tau Bootis system, the first binary star system detection.

---

[17] A short SETI-based technical treatise is offered here - http://astro.berkeley.edu/~gbower/TU_S07/lectures/AY250-SETI.pdf

[18] This skepticism was partially ameliorated in 2003 when instrumentation improvements allowed confirmation of their results. Just prior in 2002, Cochran et al. (2002) made a separate RV-confirmation of a 96-day, 1.7 M $(sini)_{Jup}$ mass planet about this binary, and claimed a first detection for themselves; it was further announce in Hatzes et al.(2003).

Planets were discovered about Upsilon Andromedae and 70 Virginis in 1997 (Murray et al., 1998). Sixteen exoplanets were found by 1998 and by 1999 the number grew to 20, to include the first multi-planet detection around Upsilon Andromedae (Butler et al., 1999; Laughlin & Adams, 1999). As the millennium closed, the planet about HD 209458 became the first transit detection to be clearly observed and measured complementing its RV data section (Brown et al., 2001; Charbonneau et al., 2001; Henry et al., 2000, 1999). This pairing of complimentary methods will be discussed further in the following. Within another year resonant systems were detected (including Gl 876 which is investigated herein), and in 2004, the first-ever direct image may have been taken of the exoplanet-like object[19] "b" orbiting brown dwarf 2M1207 by the European Very Large Telescope (Schneider, 2005).

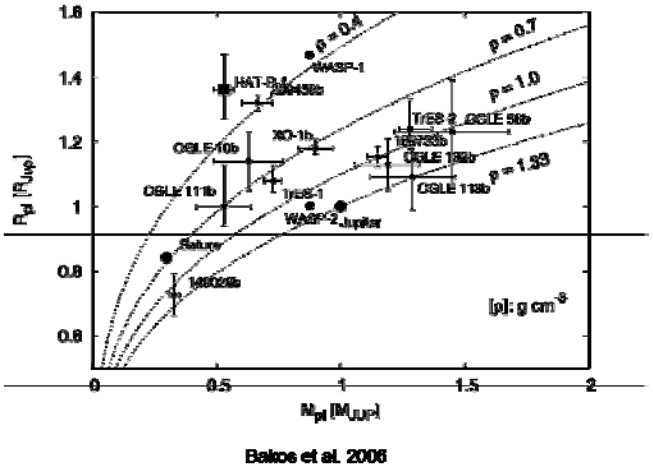

Fig 3: Above: sample of key detections relating mass, radius and density. Detections move to the right with improved schemes; eventually they will move downward as well. *Fig 4. Below:* Detection methodologies related to mass (M sin i) and orbital distance. The graphic indicates the strengths of each to detect certain planet types.

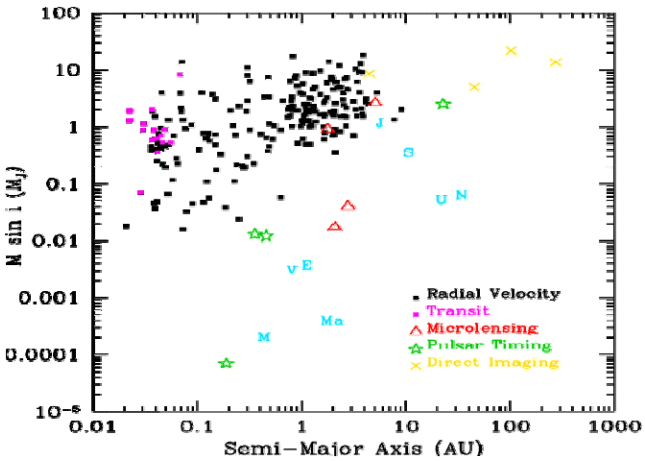

OGLE-TR-56b was discovered in 2002 and became the first planet discovered completely by transit. The system Gliese 876 which is discussed in much of this thesis, was itself discovered in 1998 with a 60 day-period planet (Marcy, et al., 1998). Its resonating 30-day sibling was discovered three years later (Marcy et al., 2001). Its third planet is arguably the smallest-massed planet, depending on its yet-known, real inclination. However, Gl 876d is vying for that title with supposed $< 2\ M_{Earth}(\sin i)$ planet Gl 581c 9.3 pc away (Udry et al., 2007), for which an inclination is also

[19] IAU definitions of a planet notwithstanding. There is some controversy over whether 2M1207b truly is a young planet, which depends critically on both age and mass, as well as how good the atmospheric models are (Chabrier, 2007; Mohanty et al., 2007)

unknown. Gl 876d was detected in 2005 by Rivera et al. (2005), and its red dwarf parent remains among the closest star to the Sun (at 4.72 pc) to have multiple planets to date.[20]

Microlensing has revealed other 62-some more distant (and arguably unrepeatable) detections (Udalsky et al., 2008). Survey methods became more popular and red dwarf stars attention as good candidates by 2003 (Kürster et al., 2003; Bean et al., 2003; and Endle, 2003). Interesting details began to populate the sample; details of an atmosphere were obtained for HD 209458b. Debris detected using radio and IR began to be correlated with planetary systems; this thesis investigated such a correlation for Gl 876 (see Chapter 8). As the field gained relative longevity, longer-period planets were detected. The exoplanet about 55 Cancri with an orbital period of 14 years, is the longest to date, and now also has the title of possessing the most planets in one system, at 5 (Fischer et al., 2007; Marcy et al., 2002). By late 2007, ostensibly 268 exoplanets were reported with creditable detections. Of these, 26 were multiple exoplanet systems[21].

In this century, the rate of detection is increasing geometrically. The number of terrestrial and space-borne searches has also proliferated (see the graphical depictions, figure 3). Some are funded through to productive programs, and some are in development. Figure 4 elaborates on parameter space which specific methodologies attempt to cover (Bakos et al., 2006). As the list of programs is quite dynamic, it is suggested the reader peruse ongoing list of the summary of detections, programs and researchers found at the Exoplanet Encyclopedia website[22]. While not complete, this list represents the scale of increasing effort put into exoplanet detection – detection through a growing diversity of successful methods.

Section 2.B: A Brief Review of Detection Techniques

Made apparent in the historical recapitulation earlier, a diverse collection of detection and characterization schemes are available to the exoplanet astronomer. Importantly, these tend to be complimentary and either fill in different portions of dynamical parameter space, or reduce shortfalls of another detection method. Each helps to cover some portion to the limits of physics and technology (see figure 4, a depiction of Schneider's data, in Seager's presentation at the 2007 MSC Exoplanet Workshop[23]). The depiction reveals each primary detection methods' actual strengths in practical terms of mass and orbit size. The clustering of detections particular for RVs and transit detections influenced the direction of this thesis.

---

[20] This honor has recently gone to Epsilon Eridani at 3.2 pc away, with a second, yet-to-be confirmed exoplanet in its Solar-like dust disk (Greaves et al.,2002). This was modeled to possibly exist at 0.8-M_{Jup} masses and 260 years by Quillen & Thorndike (2002).
[21] See the latest at Jean Schneider's catalog, www.exoplant.eu, or at the mirror, http://www.cfa.harvard.edu/planets/.
[22] See http://exoplanet.eu/people.html, and http://vo.obspm.fr/exoplanetes/encyclo/searches.php.
[23] http://msc.caltech.edu/workshop/2007/Seager_mr.pdf

Observational methods are thwarted by the fact that exoplanets are notoriously dim sources as compared to their host stars. In the visible, for example, the brightness ratio can be more than 10^8 to 10^{12} times, in terms of absolute brilliance. The planet is usually merely reflecting parent-star light), which invariably becomes washed out in the parent's glare. This glare can be overcome somewhat with a smaller ratio of radii for bigger planets and with greater lateral separation from the star. However, the latter creates detection problems for a number of *indirect* detection methods instead. Loosely related to radius is mass, which also depends on density.

An exoplanet's mass ratio to its parent is generally of order $1{:}10^{-3}$ to $1{:}10^{-5}$, so the gravitational influence of a planet over its host is very difficult to measure. In addition, the point-of-view from which an observer views an orbiting exoplanet in relation to its parent star, the inclination of its orbital plane, affects observations, particularly indirect methods. The illustration of how the inclination affects direct versus indirect classes of observations is graphically in figure 5. For a number of detection methods, this kind of dynamical inference is the path to the detection.

All observation methods of course have some bias due to the nature of the detection, the instrumentation, the target, the typical environment, and the type of data. Nevertheless, one has to "start somewhere". In fact, assessing the clustering of detections to assess bias and planetary characteristics (culling the two from each other is a difficult process), gives a summary and graphical indicator of how methods tend to support detections.

Fig 5 : depiction of dynamical methods of detection: astrometry, Doppler detection, and Transit photometry

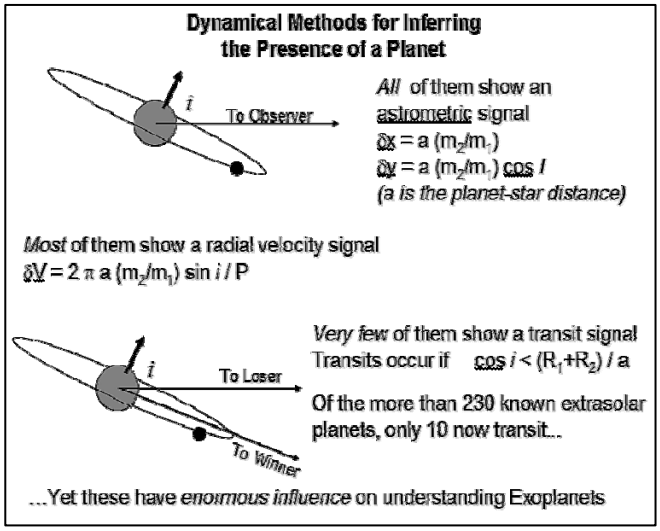

The observational methods available to the astronomer are best depicted in Michael Perryman's recent 2007 update to his frequently referenced relational diagram[24] (Perryman, 2000):

[24]Latest version at: http://www.rssd.esa.int/SA-general/Projects/Staff/perryman/planet-figure.pdf. (Figure 6)

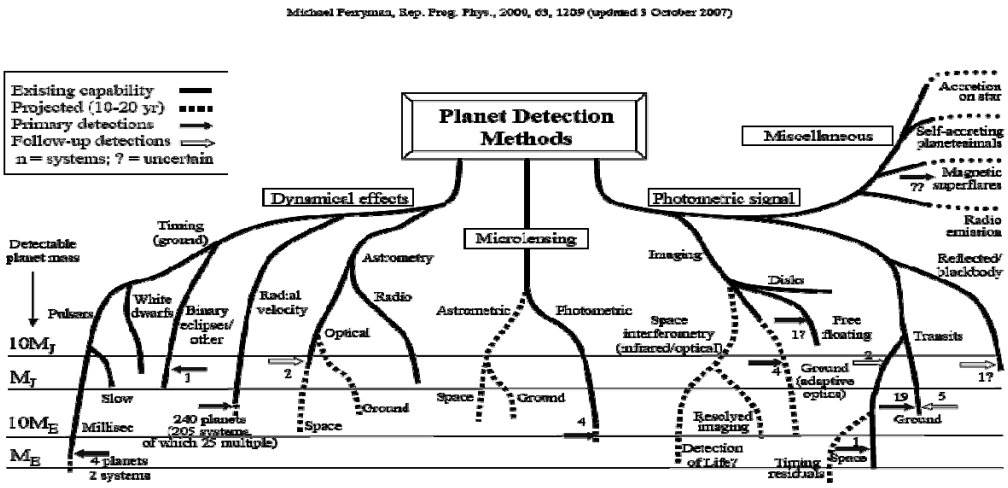

Fig 6: A relational depiction of the various detection schemes available to the exoplanet researcher

Prevalent detection methods are discussed below.

2.B.1. Astrometry.

The first well-publicized approach to detecting planets was astrometry (for example, such as with Barnard's Star). Simply, the observer images the visible and periodic gravitational effects as described by Newtonian physics. The weakness of this method is the amount of motion observable on the plane of the sky is very small as, exemplified in Shao's depiction of a notional view of the solar reflex motion due to Jupiter as might be seen from 10 pc (figure 7). In this case the orthogonal motion is 0.8 milli-arcsecond (later abbreviated *mas* or *MAS*). For this reason, a mere single detection, not discovery, has been attributed to astrometry – that by the *Hubble Space Telescope* (HST) when it was used to observe Gl 876 in 2001.

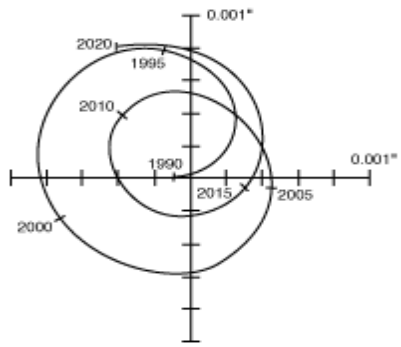

Fig 7: Astrometric solar displacement due to Jupiter, as would be seen at 10 pc. (Shao, 1991)

Currently, ground-based astrometry can approach 10 mas for bright stars; space-borne missions, (such as Hipparcos in 1990-1991) have achieved 1 mas (Leeuwen, 2007). The USNO Joint Milliarcsecond Pathfinder survey (J-MAPS), is anticipated to launch in 2013 and produce 1 mas astrometry for stars

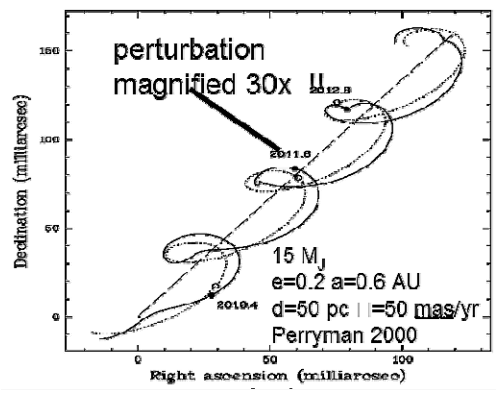

Fig 8: Example of classic astrometric planetary effect. Perryman (2000) models a star at 50 pc at 50 mas yr yr^{-1} proper motion M_p=15 M_j, e = 0.2 and a = 0.6 AU. Barycentric motion is dashed, dotted line is parallax, solid line is the gravitational effect.

brighter than V = 11 (separate to the research herein, the author plays a principle role in J-MAPS programmatics). Other faint-star missions such as OBSS (Origins Billion Star Survey), SIM-Planetquest and Gaia have been planned, so that these missions can achieve tens of micro-arcsec (μAS) level accuracies. They are, however, exceedingly complicated and expensive undertakings, primarily because their apertures are interferometric, and / or use very advanced-but-unproven focal plane technologies.

However to observe astrometric effects of gravity at present requires much of the entire wobble's period to be observed to obtain sufficient resolution. This means long period planets become poor astrometric candidates. Perryman's (2000) illustration (figure 8) offers a notional example of typical astrometric behavior ascribed to a 15-M_{Jup} planet gravitationally displacing its more massive parent as the planet and the star orbit a common barycenter. Since the mass of the star (M_*) will be much greater than the mass of the planet (M_p), that barycenter for a planet will most certainly be found within the parent star mass, causing the much larger star to scribe a much tighter circular path (notwithstanding additional effects such as proper motion, eccentricity, and inclination). For this astrometric motion, angular velocity (Ω), velocity of the star (v_*), and astrometric angular wobble ($\Delta\theta$) are given by:

$$\Omega = \sqrt{\frac{G(M_* + M_P)}{a^3}},$$

$$V_* \approx \left(\frac{M_P}{M_*}\right)\sqrt{\frac{GM_*}{a}},$$

and

$$\Delta\theta = 0.5\left(\frac{q}{10^{-3}}\right)\left(\frac{a}{5AU}\right)\left(\frac{d}{10\,pc}\right)^{-1} milliarc\ \sec$$

where M_* and M_p are the respective masses, a is the semi-major axis, g is the gravitational constant, d is distance to the star from Earth, and mass ratio $q = M_p/M_*$. Astrometric detections allow the actual mass be derived unlike radial velocity approaches discussed next.

2.B.2. Radial Velocity.

Planet detection can be done by observing changes in radial velocity (RV). This technique uses Doppler spectroscopy to measure small, regular variations in the line-of-sight speed of a star via its red and blue shifts. RV astronomers found most extrasolar planets that have been detected to date, and most of the remainder were confirmed by the RV method.

This technique can be very effective for main-sequence stars of spectral types F5 through M. Stars of earlier type (O, B, A and F0 - F4) generally rotate faster and often pulsate, which make

measurement difficult[25]. The limitations of this technique are also the need for unusual precision and the extreme sensitivity required to achieve any meaningful result. Sufficiently sensitive spectrometers, usually Echelles (Vogt et al., 1994), are large, heavy, and expensive; they also use Iodine reference cells, and they require a stationary (Coudé or Nasmyth) focus. Smaller, cheaper <15 m s^{-1} Doppler spectrometers capable of wide employment would be a tremendous boost to exoplanet detection and follow-up capabilities[26].

RV observations are particularly useful for potential exoplanet detections in the middle of the main sequence – from F5 to early M. While still good RV candidates in general, M stars begin to show a 'temperament' that means these stars need to be reviewed for any unpredictable behavior. The latest stars (M6 through T) are also often variable, or have starspots, or are subject to flares, and are variables/CVs. In addition, later stars are faint. Measuring outside the middle of the main sequence (MS) requires close evaluation of the star.

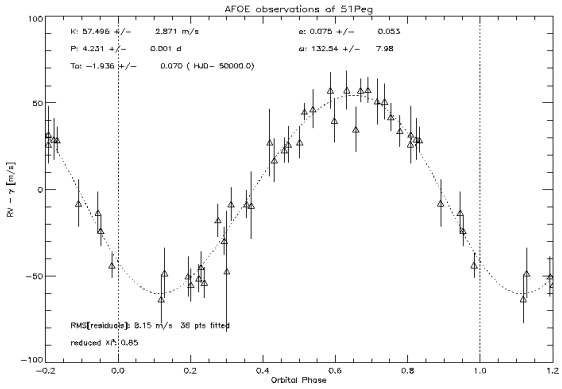

Fig 9: Classic representation of an RV Curve, here of 51 Peg, first exoplanet to be discovered about a solar-like star, with an RV of 57 m sec^{-1} and period of 4.2 days; Mayor et al (1995), Mayor & Queloz (2003).

Although unusual precision is required to discern RV variations, the distance to the star does not affect the method, although there is a photon limit for distant, faint targets. The precision of radial velocity measurements is at present best-achieved using Echelle spectrometers (an example of an Echelle RV curve is of 51 Peg, obtained by Mayor & Queloz, figure 9), such as with the Keck HIRES (High Resolution Echelle Spectrometer) and the European HARPS (High Accuracy Radial Velocity Planet Searcher) spectrometer. These instruments produce RVs down to 1 m s^{-1} to produce most of their latest detections. This detection of any RV at best only infers the radial velocity effect with respect to the line of sight (LOS) – meaning it can only give a minimum possible value for mass M_{Planet}. This value is expressed as M sin (i), because RV amplitudes do not account for any inclination, known as i. It should be noted though, that a certain amount of inclination *might* be inferred through studying the RV curve itself, through what is known as the Rossiter-McLaughlin effect. This effect, and the detection procedures, are discussed in detail in Appendix C.

[25] Hot Jupiters have been found around some A stars. While the stellar lines are broad, a few have been found (Desort, 2007).
[26] For example see Ge, Erskine & Rushford (2002), and Hajian et al. (2007).

RV detection is performed by comparing the red and blue shifting spectral lines in cadence with the planet's orbit as portrayed in the generic cartoon, figure 10. The RV for a given star does not remain constant, but instead varies as a function of the angle between line of sight and the exoplanet's velocity by this form:

$$\nu_{s,r} = \nu_s \cdot \cos\theta \ ,$$

where v_s is the velocity, and θ is the changing angle between the planet's velocity in its orbit (the closing/opening vector component), and LOS.

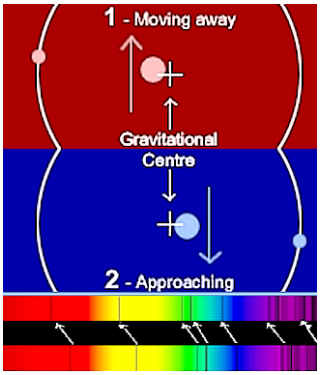

Fig 10: Cartoon depiction of how observer-bound photons red and blue- shift relative to the LOS, due the gravitational wobble of the star-planet center of mass. This reveals itself in the spectral lines (owed to the chemical composition of the star) which shift left and right (to the red and blue ends) as the Doppler Effect makes itself known.
Fine shifts are less apparent and and must be compared to an overlaid set of lines to see the shifts.

To do this and achieve better than 5 m s^{-1} precision, one compares the forest of emission or absorption lines using a good reference set of lines. Most Echelle spectrometers use an iodine cell to superpose the cell's forest of very narrow spectral lines. iodine was chosen because it broadly and evenly intersperses its own lines over the target's spectrum, even at very high resolution. Echelle spectrometers then provide the necessary optical resolution (at the aforementioned material cost). Consequently as suggested, Echelle spectrometers frequently reside at the more stationary Naysmith or Coudé foci of large-aperture optical telescopes.

Despite limitations on discerning inclination, RV observations solve for a number of parameters to describe many components of an exoplanet system's orbital dynamics. Working at a curve such as the 51 Peg example above, the period P is easily gleaned from the peak-to-peak measurement on the RV curve. Applying Kepler's Third Law, the planet's RV-derived distance from the star (r) is found in:

$$r^3 = \frac{GM_{star}}{4\pi^2} P_{star}^2 \ ,$$

such that G is the gravitational constant, and M and P are stellar mass and observed period, respectively. From this, Newton's law of gravity gives

$$V_{PL} = \sqrt{GM_{star} / r} \ ,$$

where the planet's velocity is V_{PL} . The planet's mass (sin *i*) can then be found (not true mass, which would require other detection methods) from the calculated velocity of the planet:

$$M_{PL}(\sin i) = M_{star} \frac{V_{star}}{V_{PL}} \ ,$$

using the parent star velocity, V_{star}. The relationship reveals that for the RV method, the more massive the planet, the better. The more inclined the orbit toward edge-on at 90°, the easier the detection, and sin *i* approaches unity. Determining inclination is done with other methods such as transit detection. In such a combination, one can then characterize the system's orbital dynamics completely.[27]

2.B.3. Pulsar timing.

A deceptively straightforward and the first successful detection technique, pulsar timing observes variations in the otherwise very regularly spaced, clock-like pulses of a pulsar. A pulsar's primary attribute is to emit such radio 'ticks' due to misalignment of its magnetic and spin axes subsequent to its collapse during its supernova. These ticks are more precise on short timescales than the Cesium standards used for atomic clocks. As a result, any variations stand out, as cartoon figure 11 and data example (figure 12) depict. These can be phase-timed by Fourier modeling (producing a Lomb-Scargle periodogram), then counting a starting time, say called T_0, onward and noting deviations from the root spin frequency, period and any of its harmonic-like derivatives. Overlaying sinusoidal Newtonian effects of a notional planet are revealed as residuals that can become evident during a reduced fit, similar to the least-squares (LSF) curve-fitting used with other methods. Effectively, exoplanet detections about pulsars are due to temporal deviations as opposed to positional ones in astrometry, or spectral space deviations of Doppler spectroscopy.

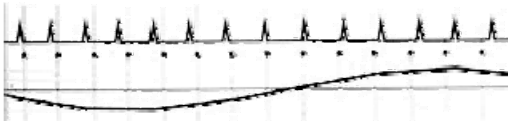

In the above cartoon illustration *(fig.11),* a periodic shift in the pulse amplitude (y-axis) arrival times (x-axis) of a pulsar's very regular milli-second period can be extracted to reveal a net variation caused by gravitational effects. Very accurate pulse time measurement lends far greater precision to an orbital solution than similar methods such as Doppler spectroscopy and astrometry. Real data, below *(fig.12),* from Wolszczan & Frail (1992) shows the specific effect of the planet discovered around PSR1257 + 12.

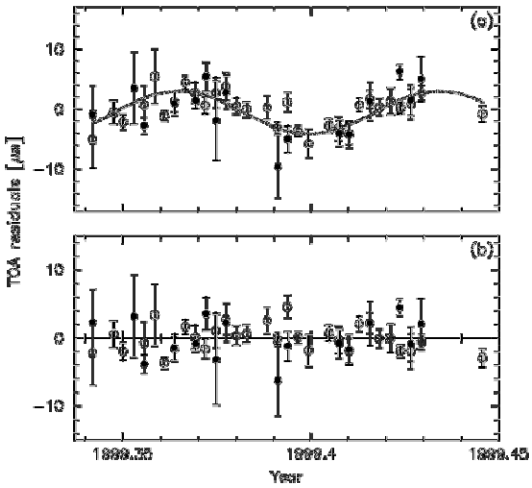

Six pulsar planets have been declared, then retracted or declared doubtful. To date, two detections have remained intact: a three-planet system around PSR 1257+12, and a single planet around PSR B1620–26. Of course these are likely dead planets owing to the parent's intense radiation, and are thought to have been formed after the parent star's SNe (survival through

[27] Other methods must also be used to then infer planet radius, and in turn, derivation of likely density and even composition.

supernovae being unlikely). See Cassen, Guillot & Quirrenbach (2007), and the latest listing of pulsar planets at the Paris Observatory Exoplanet Encyclopedia[28]

2.B.4. Debris Disks.

Exoplanets should be holistically examined as part of an entire extrasolar system. Accordingly, the formation of exoplanets and their ongoing interactions with their smaller cousins should be taken into account when attempting to detect or model an exoplanet system. Planetesimals, including minor planets, non-primordial dust and other gravitationally-affected rubble, may signal the presence of planets themselves. They certainly contribute to the accurate understanding of the orbital dynamics of any exoplanets in orbit about a star. Chapter 8 will review debris and dust disks in more detail.

Debris disks, sometimes termed Kuiper belts, in approximation to their named Solar System counterpart, have been seen encircling a number of stars; more than 15% have been found around nearby sun-like stars (Greaves et al., 2003). Non-primordial dust may signal ongoing regenerative collisional processes, and various inhomogeneities may be caused by the gravitational influences of planet(s). Such dust is detectable because it usually re-emits, and to a minor extent reflects, its parent's starlight. In the case of absorption, black body-like re-emission occurs at lower energies. As the particles absorb the parent star's light it is re-emitted as infrared or millimeter radiation; there are ongoing debates as to how cool (10- 140K) this emission is, and is further discussed in Chapter 8. Generally, emission is loosely dependent upon the particle size, because the particles behave as many small, frequency-dependent, resonating dipoles. The efficiency of this radiation process allows disks with a sufficiently large enough total surface area to outshine its parent star in the lower re-emission.

The Infrared Astronomical Satellite (IRAS)'s 1983 dust detections were the first of their kind. The means to detect IR emissions with enough sensitivity has also been achieved with Hubble Space Telescope (HST) Near - Infrared Camera and Multiobject Spectrometer (NICMOS), and now the Spitzer Space telescope, which can go deeper into the infrared of the two. A number of radio telescopes can detect millimeter radiation from dust. This thesis for example describes millimeter efforts using VLA (Very Large Array) and ATCA (Australia Telescope Compact Array)[29]. Several other instruments are becoming viable as millimeter telescopes; the Atacama Large Millimeter Array (ALMA) will certainly be a *tour-de-force* in this waveband. That telescope is slated to be available for use sometime in 2011. Section 2.E and Chapter 8 will discuss planetary system dust and millimeter detection in more depth.

---

[28] See http://exoplanet.eu/catalog-pulsar.php.
[29] The VLA and ATCA, used herein, are characterized in Chapter 4.

This is a good place to mention the need to continue to broaden detection methods across the electromagnetic (E-M) spectrum. In 2007, a decadal study of exoplanet schemes and studies was performed by the U.S. National Science Foundation's (NSF) Astronomy and Astrophysics Advisory Committee (AAAC). The AAAC commissioned the Exoplanet Task Force (ExoPTF) to review eighty-five white papers.[30] The list purported a wide assortment of proposed or ongoing methods and programs in order to recommend detection direction. This "variation on a parameter-space illustration" reveals where direct detection schemes fit in terms of known astronomical signatures of solar-like systems, and planets. Unlike Bakos' (2006) representation of primarily optical means shown earlier, the ExoPTF's representation reveals the yet-to-be heavily scrutinized portions of the E-M spectrum, where decadal efforts will be best served. In spite of a wide variety of available schemes to detect exoplanets optically, the ExoPTF showed that emphasis should also be placed on the associated dust, and emissions outside the visible range. Similar reasoning guided efforts herein toward a pan-spectral assessment of the Gliese 876 system, including its associated dust disk (or lack thereof).

Visualization of the ExoPTF's review is reproduced as figure 13, which was obtained from the review, online[31]. Note the significant parameter space attributed to disks and dust.

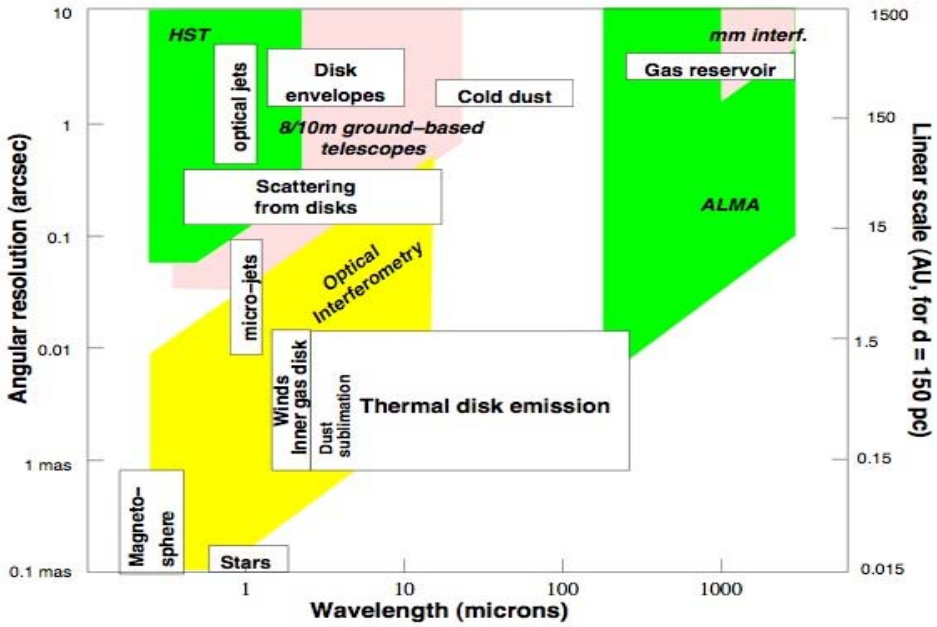

Fig.13. Graphical illustration of of the primary sections of parameter space which should be the focus of search efforts, as posited in the decadal review of the AAAC Exoplanet Task Force[29]. Dust and disk searches remain central to detecting and understanding exoplanets and their formation.

[30] seen here: http://www.aura-astronomy.org/nv/Lunine_ExoPTFInterimReport.pdf.
[31] See http://www.nsf.gov/events/event_summ.jsp?cntn_id=108113&org=AST.

2.B.5. Gravitational Microlensing.

Akin to transit photometry, gravitational microlensing occurs when the gravitational field of a star acts as a relativistic lens, magnifying the light of a distant background star. Possible planets orbiting the foreground star can cause detectable spiking and movement of relative photons. Cartoon figure 14 reveals the technique's basics. Figure 15 is an example of the notional result – with the spike which is detected overlaying the photometric curve. Light-curves from stellar micro-lensing are usually smooth, so when a companion of ample brightness moves behind the 'lens', a sharp perturbation results which can be detected photometrically. Good treatises on lensing can be found in Schneider, Ehlers & Falco (1999).[32]

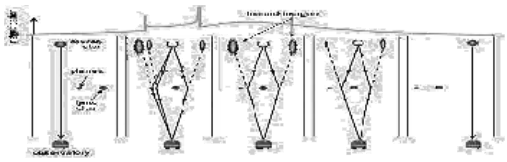

Two simple illustrations to portray Gravitational lensing. Top (*Fig.14*) shows the optical distortions attributed to the relativistic bending of the beam, and the bottom (*Fig. 15*) shows the resultant photometric curve-with

A lensing detection would be assessed from apparent motion of the lens across the sky with its Einstein radius, θ_E, also called the Einstein angle. The Einstein radius is determined using

$$\theta_E = \sqrt{\frac{4GM}{c^2}\frac{d_S - d_L}{d_S d_L}}$$

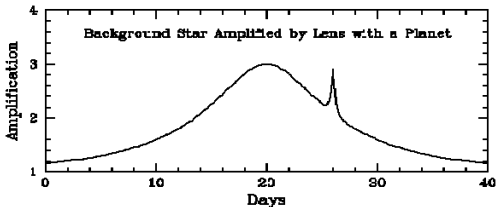

where M is lens mass, and d_L, and d_S are the lens and source distances, respectively. During microlensing, the brightness of the source is amplified by the amplification factor (A), which solely relates d to the alignment alignment of the observer, lens, and the exoplanet. The angular separation of the lens and the source (u), is divided by θ_E, to give the relationship

$$A(u) = \frac{u^2 + 2}{u\sqrt{u^2 + 4}} \quad .$$

This value has a number of ramifications beyond the scope of this discussion which can be found in general literature. For the purposes of a short review, note that the value u changes rapidly over short intervals to produce the central characteristic of characteristic of microlensing. This interval of time is called the Einstein time (t_E), and is defined by the traverse of θ_E. The Pythagorean Theorem is then used to relate u related to this time u(t) in this form:

$$u(t) = \sqrt{u_{min}^2 + (\frac{t - t_0}{t_E})^2} \quad .$$

Here, the minimum separation (u_{min}) determines the maximum brightness.

[32] Another useful review is found reading Petters., Harold, & Wambsganss (2001).

Terrestrial planets may be detectable by gravitational microlensing, but bent light makes statistical estimates of the properties of such planets and often of the host star difficult, unless the system is at least 1500 pc away. Such distant systems, however, are difficult to resolve. In addition, great distances make accessibility to such exoplanets beyond human imagination for a good while yet. Microlensing is most of all, non-cyclical. The chance alignment never reoccurs. For this reason, follow-up observations with other methods are not currently possible, although concurrent observations may help to validate the event. In any event, microlensing studies do offer a statistical census of earth-massed planets populating the galaxy. The Warsaw-Princeton Optical Gravitational Lensing Experiment (OGLE) group are using this technique and have made six distant detections since 2002. Eight other teams currently study lensing events fin search of exoplanets.[10]

2.B.6. Direct Image/Coronal Nulling.

Direct imaging would be definitive proof of exoplanets, but is extremely difficult to perform. It requires overcoming an enormous star-to-planet flux (and radius) ratios and it demands significant resolution, both due to intense glare. Coronography 'improves' the ratio by blocking the stellar photosphere to "see" exoplanets. The resolution is further improved by nulling interferometry and adaptive optics. Generally, direct imaging favors exoplanets much more massive than Jupiter, exoplanets with large semi-major axes, and hot exoplanets that emit some internally generated radiation.

A few current telescopes can direct-image exoplanets including the Gemini telescope, the Very Large Telescope (VLT), and the Subaru telescope. VLT was used in 2004 to make the first direct image of the exoplanet-equivalent mass about the brown dwarf 2M1207 (Chauvin et al., 2004)[8]. This mass was confirmed in 2005. Three other possible exoplanets have been ostensibly observed directly, and yet have not been confirmed.

2.B.7. Transit Photometry.

Through this technique, an astronomer uses a photometer -- which is usually nowadays a CCD focal plane array -- to measure small, regular variations in the apparent brightness of a star. These variations are induced by the occultation passage of the suspected planet across the stellar disk. Take note of figures 16 and 17, where the planet's orbital path (relative to the observer) takes it through point 1, then point 2, where it transits the limb of the parent star and begins to occult. Occultation continues at point 3 in the illustration, and the planet continues until it re-crosses the stellar limb on the right edge. The flux variation detected by the CCD or photometer during this transit would then reveal a curve similar to the one also shown at right (points 1, 2 and 3 are comparable). To make detections comparable and additive, and to increase signal-to-

noise (S/N or SNR), passband filters are used that center on the parent star's blackbody curve according to Wein's law. The transit technique represents the bulk of the technique used in this thesis. Chapter 3 discusses transits in detail.

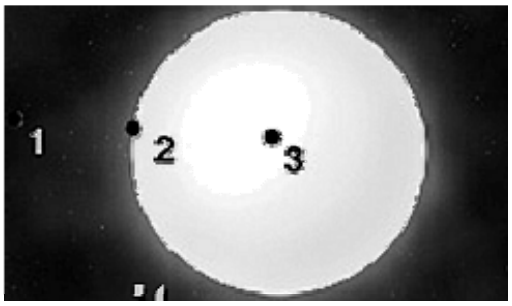

Above (*Fig 16*), simple representation of that occurs as a planet occults (or eclipses) the face of its parent star. Note that for this to take place the orbital geometry must have an inclination near i = 90° for the star's disk to be occulted. Below (*Fig. 17*), the hypothetical photometric curve which would result from observations of the above transit. Note the Points 1 (prior to ingress), 2 (limb passage), and 3 (full transit) in both illustrations.

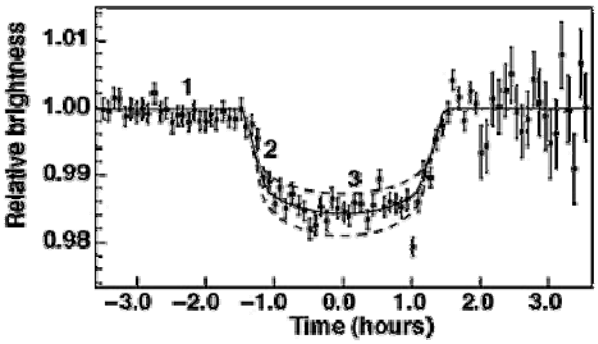

To observe a transit, the inclination of the exoplanet's orbit must be close to 90°, which is a serious limitation. The general probability is 1-3% that the necessary geometry will occur for a given target to show a transit to an Earth-bound observer. The likelihood of a transit is also based on additional dynamical factors in the orbital geometry. The nature and likelihood of a transit is the function of the planet's period, semi-major axis, and planet and star radii ratio. A further difficulty is that the planet produces a relatively small occultation of the flux of its parent star, so that any flux variation will be small. This has been typically expected to be less than 1% drop for Sun-like stars, but more like a 10% variation is possible for smaller, dimmer stars. The latter was a major influence in the selection of Gl 876 for observation, as discussed later. Unfortunately, this technique can suffer from high false detection rates because of other causes of stellar variability, which will also be discussed un subsequent sections.

Light curves from transits such as above right give additional data about planetary diameters and orbital inclinations that can be further combined with data obtained from other techniques (often radial velocity) -- to infer about the planet's composition and structure. When combined with good RV data, a genuine mass and density can be gleaned. If adequate fidelity is available for a target, an observer may further discern and study an exoplanetary atmosphere as is done for HD 209458, where less-sharp, subtle variations and spectral lines on the 'slope' of ingress and egress (e.g., point 2 in figures 16 and 17) indicate a gas envelope and the planetary limb, and the possible indication of elements. Back-side ingress and egress studies can also be performed. Varying transit times, slopes and characterizations of ingress/egress curves, all can be matched to subtle variations in spectral RV curves and vice versa.

Variations in RV curves can sometimes reveal whether a planet will transit (discussed in Chapter 6 and Appendix C; further reading is found in Charbonneau et al., 2007).

Transit photometry technique can be optimized to be both a targeted technique for high probability stars and a method to conduct broad surveys, or any combination of both. Improving the metrics in this particular method has yielded a rate of detection which is now growing. As of late 2007, 34 planets have been detected or observed by photometric transit[33]. This technique will be explored in detail through much of the remainder of this research.

2.B.8. Miscellaneous Detection Techniques.

Various derivative methods precipitate from the basic ones, most notably: eclipsing binaries, orbital phases, polarimetry, and interferometry. In-depth discussions on these can be found in the literature[34].

In an eclipsing binary, the 'clean' periodicity of the primary (and secondary) eclipses is disturbed if a binary counterpart tugs to offset the barycenter. Here the cadence changes are timed (and in some cases disturbed radial velocities measured) and the curves are fitted to discern the orbital dynamics of the two stars along with their planets. Using photometric methodology, orbital phases may be observed to vary subtly with inclination. Such an approach requires a photometric capability on par with that required to detect transits of Earth-like planets. In polarimetry, unpolarized parent starlight is differentiated from the light reflected from or passing through exoplanetary atmospheres, Kuiper-like dust disks, and other polarizing molecules in the system, which indicates their presence and allows composition studies. This was recently shown to be a successful detection method, when Catala et al.(2007) detected the effects of a giant planet embedded in the magnetosphere of its star with the ESPaDOnS spectropolarimeter on the Canada-France-Hawaii Telescope (CFHT).

Interferometry can be applied spatially to an astrometric instrument to allow a synthesized observation of high resolution. Radio astronomers already do this, although optical devices are much harder to make work than radio interferometers. This is partly because the optical frequencies demand much greater precision than radio does. But optical interferometers are being made and used, and all bands are used for for astrometric and direct observation detections in the radio, IR and optical. Fourier devices can operate in temporal or even spectral phase space. The latter allows for a precise RV-capable instrument, albeit with

---

[33] The latest tally is found at http://exoplanet.eu/catalog-transit.php.

[34] Further discussion on these methods is found in Doyle & Deeg (2006), Jenkins & Doyle (2003), Schmid et al. (2006), and Colavita & Shao (1994), respectively.

throughput, complexity and alignment challenges. USNO's dispersed Fourier Transform Spectrometer (dFTS) is an example of a metrologically calibrated variant (Hajian et al., 2007; Nordgren & Hajian, 1999), while University of Florida's Exoplanet Tracker (ET) is calibrated with an Echelle-like iodine cell (Ge, 2002; Ge et al. 2003). Optical interferometry can also be used to perform direct imaging and astrometry of exoplanets (Armstrong et al., 2004). Of course the Space Interferometry Mission (SIM) and subsequent spaceborne missions will be included in the list of forefront exoplanet interferometers when built (McCarthy, Fischer & Marcy, 2007).

Doubtless, new techniques and methods will emerge in the endeavor to detect and characterize exoplanets. Capitalizing on the best combinations serves to give observers the most-ready exoplanet detections sought.

Section 2.C: Details of Basic Transit Photometry

As noted in the previous section, transit photometry poses inherent challenges to those who undertake it, but the method carries sufficient merit and sensitivity to make it the second-most successful observational method to date behind the RV method. Despite the rigor required along with geometrically low odds for detections, the opportunity to perform transit photometry successfully is available to modest and varied instrumentation if a number of basics and exactitudes are kept in mind.

Occulting photometry is the earliest indirect method available for detecting other worlds. Johannes Kepler was the first to predict transits within solar system (Chapman, 1998), and then Pierre Gassendi used Kepler predictions to be first to observe transit of Mercury in 1631 (Teets, 2003)[35]. For exoplanets *beyond* the Solar system, Otto Struve not only was the first to suggest RV spectroscopy as a means to detect planets as noted earlier, but was also the first to advance the concept of transit photometry a viable means to detect exoplanets. Anticipating ~1M_{Jup} discoveries of exoplanets at small semi-major axes, Struve's 1952 predictions came true nearly half a century later, with transit observations of HD 209458b. As he described, "It is not unreasonable to expect that a planet might exist at a distance of 1/50 astronomical unit…. there would, of course, also be eclipses -- the loss of light in stellar magnitudes is about 0.02" (Struve, 1952; Perryman, 2000). His prediction turned out to be both accurate and prophetic.

[35]An interesting review of the 1631 transit observations of Venus is found here: http://www.nao.rl.ac.uk/nao/transit/V_1631/.

Transit photometry exhibits a number of noteworthy and useful characteristics which are important to understand. The method favors edge-on orbits. It favors large and close-orbiting planets. It favors small-radius parent stars. It can be used to survey large numbers of stars at once or conversely target special candidates, or it can perform a combination of these. It is a well-suited to follow-up RV detections, and it constrains mass, and generally density, of any RV detection. Transit photometry might further assess mass, composition, density, rings/belts/dust, atmosphere, temperature, Moons, and habitability.

2.C.1 Introduction: Why Photometry

As noted, transit photometry not only conveys an ability to detect terrestrial planets, it allows determination of size, it is useful in the study of the entire range of main sequence stars, and it provides a periodic, differential signature independent of the semi-major axis. It can accomplish this while using devices of modest aperture and complexity. In such a quest, transit photometry must answer five questions about detecting exoplanets. How will photometry successfully detect them? What will the results reveal about their physical structure and formation history? What can be learned about their habitability, including potential atmospheres? How can photometry be optimized to make the first detection of a habitable planet beyond the Solar system? How can it be used to produce a beginning census and from this characterize the number of "habitable Earths", a parameter identified as $\eta_{\mathbf{Earth}}$?

The answer to "why photometry?" can be distilled to a single reason: terrestrial planets can be better detected by using the transit method than by any other means. This is more so even for M stars, due to their abundance, transit depth and probability for transits. The question that must be answered is, could enough stars be surveyed with sufficient precision and for enough nights to attain full phase coverage in either targeted or survey studies? That answer can be "yes".

Transit studies are sensitive certain to aspects of celestial mechanics which are very helpful to understanding the larger characteristics of the system. First, the intervals between successive transits of a planet on a fixed Keplerian orbit are constant. However, these intervals will gradually change for orbits that precess, likely owing to the oblateness of the central star, general relativity, or the presence of other masses in the system (Miralda-Escude 2002). Further, tidal dissipation will alter both the semi-major axis and eccentricity of a close-in planet, thereby changing the transit timings (Sasselov 2003). The short-term interactions with other planets have the most important influence on the intervals between successive transits,

as has been suggested for HD 209458b (Bodenheimer et al 2004). Limb darkening is also a factor, and will be discussed in Chapters 3 and 6.

2.C.2. Photometry Basics

Three types of photometry were specifically used in the optical observations taken in the studies reflected in this thesis. Each of these types is named as to how particular data is gleaned from its source imagery, and the three are interrelated, and *not* mutually exclusive. Aperture photometry is the most common extraction technique. It is done, as its name suggests, by placing an annulus aperture about stellar images to be measured for variations in photon flux. This photometric aperture is then compared to apertures encircling selected comparison, or check, stars to determine any comparative fluctuations brightness, relative to these standard (and hopefully stable) stars. Such comparison is known as differential photometry. Usually differential photometry compares the target to one or more nearby stars within a single, common field of view (FOV). Within this FOV, most sky and instrument variations are eliminated in the inter-comparison procedure. One must further standardize measurements and reduce noise by ensuring sequential (or distributed) measurements are made using the same check stars and filters. When the FOV just does not have suitable check stars within it, one may resort to ensemble photometry. Ensemble photometry is a stitching together of two or more fields of view when suitable check stars are not found in one (Honeycutt, 1992).

The fundamental characteristics of a planetary transit can be described by essentially three variables: the fractional change in stellar brightness, the transit's duration, and the periodicity of the transit. A number of additional attributes can be found, or derived, as well. Scaling laws apply to transit geometry, so that transit discovery depends on the planet (mass, radius, orbit size), on the star (mass, radius, luminosity, distance, galactic latitude[36], dust extinction), and on experimental parameters (aperture, FOV, quantum efficiency, bandwidth, angular resolution, sky brightness, duration, and duty cycle). Scaling laws help optimize targeting and survey acquisitions. Also, Kepler's Third Law (defined in Appendix D) is used in order to calculate the semi-major axis as discussed earlier. In calculations herein, the transit is presumed to cross the center of the star and limb darkening is ignored, except for the effects discussed later. The transit depth infers the planet's size, because the brightness, or transit

[36] Galactic latitude is important because transit photometry requires a sufficiently dense FOV to include check stars for inter-comparison, so regions must be chosen with sufficient populations. As well, for those conducting surveys galactic latitude will additionally reveal the best regions for more numerous targets in a given spectral class.

depth, changes are equal to the ratio of the planet's disk area to the parent star's disk area. Transit duration, however, only relates to an exoplanet for a single given orbital distance. The transit depth is related to ratio of areas, and the star's area can be estimated from its spectral type. This flux depth, $\Delta F/F_o$, can also be estimated using $\Delta F/F_o = (r_P / R_*)^2$, where r_P and R_* are the respective planet and stellar radii.

Fidelity in making an observation is critical to observing it. An instrument must have a range and depth of detection capability to detect subtle variations when operating close to a noisy signal floor, and this expanse of depth is the number of bits the detected intensity can "range across"; bit levels are analogous to their computer counterpart which describes information bandwidth. For photometry, 16-bit CCDs can detect better than 1% variations as a rule-of-thumb, and 8-to-10-bit instruments can detect a photometric flux variation of ~10%. For a quick initial assessment, one may calculate this probability based on the radii of both the parent and the planet that a transit will occur. Thus follows, that for a planet radius much less than the parent star's radius, a simple period estimate for the notional transit becomes

$$P_T = \sin\theta \frac{R_*}{a},$$

or based on Kepler's third Law,

$$P^2 M_* = a^3$$

where M_* is the star's mass and a is the semi-major axis of the orbit. A small semi-major axis "a" improves the chances for and frequency of exoplanet detection. From a simply-centered transit where $i = 90^o$, duration can be approximated by using time

$$\tau_{Center} = 13\, d_* \sqrt{\frac{a_{AU}}{M_*}}$$

where a is the semi-major axis, d is diameter, and M_* is stellar mass. Also some "foldable"[37] regularity in the repeating transit pattern provides information. In addition to predicting future transits, spotting the periodicity constrains the mass along with inclination. Next, planet radius can be gleaned from the depth of the transit based on limb passage. As a result, flux variation measurements can be used to determine the planet's size, once stellar size is determined. To

37Folding refers to fitting photometric light curves based on many techniques similar to fitting RV curves (see Appendix C): $\chi 2$ minimization, Lomb-Scargle, Bloomfield, Discrete Fourier Transform, etc. Fitting is done using computational algorithms which perform period analysis to find periodicities – transits – in the time-series photometry. Transits are by nature foldable.

summarize, three variables prove to be primary in the initial assessment of a planetary transit: periodicity, duration, and change in luminosity or flux (ΔL_*). P determines semi-major axis, *a,* given that the stellar mass, M_*, is known from the spectral type of the star. From these basics a further, more comprehensive understanding of the transit relationship can be deduced.

Section 2.D: Transit Geometry Relationships

To understand the parameters that define the orbital mechanics of a notional system, an understanding of the astrodynamical relationships in some system provides a basis for "how" and "why" transit observations contribute to characterizing an exoplanetary system. To expand on those introduced previously, transit photometry along with RV, can provide: the semi-major axis a, the period (P), the orbital eccentricity (e), the system inclination (*i*), the longitude of the ascending node (W), the argument of perihelion (w), and the time of perihelion passage (t). Appendix D is available for even further review the dynamical parameters. Figures 18, 19 and 20 clarify key relationships with respect to transit dynamics in particular. The first figure (19) gives an X-Z (orthogonal to the LOS) view, the second below

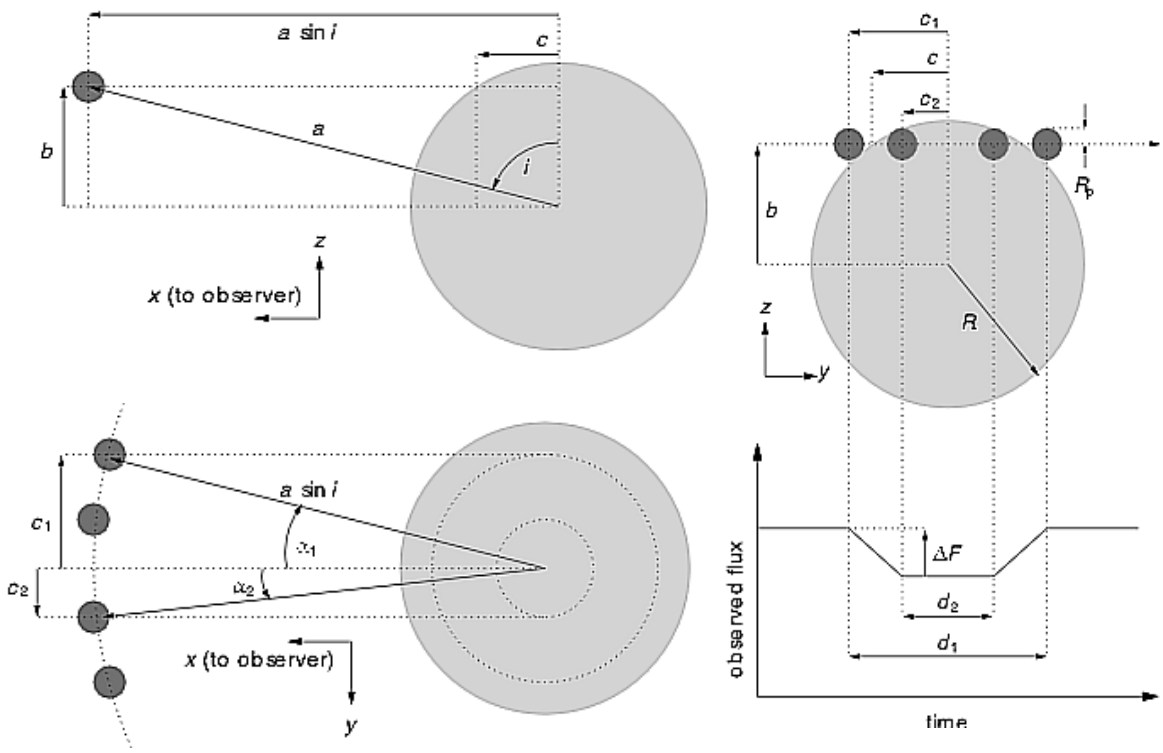

Graphical, 3-view representation of transit geometry. The Z axis is vertical, the X axis is along the FOV, and the Y axis is in the plane of the sky and slices through a polar ($i = 0$) inclination. Upper left (*Fig. 18*) is a "side view" of the light path to Earth, Upper right (*Fig. 19)* is the geometry seen by the observer correlated to a "detection", and lower left (*Fig. 20*) is an overhead depiction. See text

it (20) an X-Y (overhead) view, and the third, right (19), is a Y-Z, Earth-bound view, which is correlated to a temporal graphic that portrays a cartoon transit flux dip. Throughout this section, the mathematics follow Aigran & Pont (2007), Sándor (2006), Charbonneau et al. (2006), Roy (2005), Holman & Murray (2004), Seager & Mallén-Ornelas (2003), Mandel & Agol (2002), and Murray & Dermott (1999).

The angles and lengths labeled in these illustrations provide a visual depiction of the variables used in the equations that follow. In this section, let *i* be the inclination, *a* be the semi-major axis of the orbit, R_* be the stellar radius, R_p is the planetary radius, and ΔF be the well depth, or flux, depth during transit as opposed to the flux *F* observed outside the transit window. Iterations of parameters c and d are the travelled transit distance, which is related to time or transit interval, including transit ingress and egress through the limb of the star. Parameters b and a provide offset for non-ideal transit passages, such that $i < 90^o$. Using the parameters above in the relationships from the equations which follow, we can define the parameters for the orbital mechanics of the notional system (subsequently this leads also to a more accurate assessment of what a good probability might entail). These ignore limb darkening.

Following the progression as in Seager & Mallén-Ornelas (2003), the relationship between the flux dip to the planet-star radii,

$$\frac{\Delta F}{F} = \left(\frac{R_\mathrm{p}}{R_\star}\right)^2$$

where the planet's radius can be determined as:

.

$$R_p = R_* \sqrt{\frac{\Delta F}{F}}$$

this may be combined with the period-mass-orbit relationship,

$$\left(\frac{p}{2\pi}\right)^2 = \frac{a^3}{G\,(M_\star + M_\mathrm{p})}$$

to determine the transit interval at points of first-last limb passage, and the full-occultation interval. This is done by reducing transit flux intervals d_1 and d_2 (see the graphic above) as follows:

$$d_1 = \frac{p}{\pi} \arcsin\left[\frac{R_\star}{a \sin i}\sqrt{\left(1+\frac{R_\mathrm{p}}{R_\star}\right)^2 - \left(\frac{a}{R_\star}\cos i\right)^2}\right] \quad \text{and} \quad d_2 = \frac{p}{\pi} \arcsin\left[\frac{R_\star}{a \sin i}\sqrt{\left(1-\frac{R_\mathrm{p}}{R_\star}\right)^2 - \left(\frac{a}{R_\star}\cos i\right)^2}\right].$$

Then when $R_* << a$, the expression for d_1 and d_2 simplify to:

$$d_1 = \frac{p\,R_\star}{\pi\,a\,\sin i}\sqrt{\left(1+\frac{R_\mathrm{p}}{R_\star}\right)^2 - \left(\frac{a}{R_\star}\cos i\right)^2} \quad \text{and} \quad d_2 = \frac{p\,R_\star}{\pi\,a\,\sin i}\sqrt{\left(1-\frac{R_\mathrm{p}}{R_\star}\right)^2 - \left(\frac{a}{R_\star}\cos i\right)^2}\ .$$

This may be further simplified in central passages ($i = 90^\circ$), as:

$$d_1 = \frac{p\,(R_\star + R_\mathrm{p})}{\pi\,a} \quad \text{and} \quad d_2 = \frac{p\,(R_\star - R_\mathrm{p})}{\pi\,a}\ .$$

Density can be simply derived from planet mass and radius

$$\rho_P = \frac{M_P}{R_P^3}\ .$$

The orbital frequency can also be simply determined using the period (P), as the orbital frequency is $\frac{d\alpha}{dt}$. The broken-plane angular frequency (ϖ) is then simply

$$\varpi = {}^{2\pi}\!/_{P}\ .$$

Do note that the term ϖ used here is not the *longitude of pericenter* (ϖ) described in Appendix D. Next, the semi-major axis a can be derived using

$$a^3 = GM_* \frac{P^2}{4\pi^2},$$

where M_* is the star's mass (much greater than M_P) and G is the gravitational constant. Now, assuming a central transit at an inclination of $i = 90^o$, the normalized semi-major axis a from the star's center to the planet's center, called the impact parameter (k) , is defined as

$$k = \frac{a}{R_*},$$

which is derived from $$k = a\sin\frac{\varpi t}{R_*}.$$

Substituting the additions of radii for the semi-major axis, the impact parameter (k) becomes

$$k = \frac{R_* + R_P}{R_*}.$$

From here the transit intervals can be derived, where time for each of d_1 and d_2 can be shown to be

$$t_{d2} = \frac{\arcsin\frac{R_* + R_P}{a}}{\varpi}$$

or for the entire interval, $$T_{d2} = 2\,t_{d2} = \frac{2\arcsin\frac{R_* + R_P}{a}}{\varpi}$$

$$= \frac{P\arcsin\frac{R_* + R_P}{a}}{\pi}.$$

These are central transits; non-central transits must assess the effect of the cosines of inclination, time and frequency. A good treatise on complex, off-center transits is found in Seager & Mallén-Ornelas (2003), which in general gives the time interval in this case to be

$$T_{i \neq 90_o} = P \arcsin\left(\frac{R_*}{a} \sqrt{\frac{(1+R)^2 - k^2}{1 - \cos^2 i}} \right) \Big/ \pi .$$

In this thesis, transits will be assumed to be at or near center, because both the inclination must be very close to 90° anyway, and the dynamic range of the instrumentation above the noise floor is insufficient to observe the difference.

The small-offset inclinations should still be understood, as an offset lowers probability, transit interval, flux depth, and may make the period vary slightly. So having determined the full-depth portion of the occultation, d_2 over its measured time, T_{d2} one can now use these parameters in concert with other terms (gravitational constant, mass, stellar radius, and period) to derive inclination i, if it is not derived elsewhere. Using this time, mass (M_*), stellar radius (R_*) and orbital period (P_*), Kepler's Third Law can then be used to show that the inclination is

$$i = \arccos\left(R_* k \sqrt[3]{4\pi^2} \Big/ \sqrt[3]{G M_* P^2} \right),$$

while the semi-major axis is determined to be $a = R_* K \big/ \cos i$.

These derivations are without regard to another yet-discussed effect on the ideal photometric transit curve: the effect of quadratic limb darkening. Limb darkening is the reduction of intensity of the disk's intensity at the limb due primarily to its photospheric transparency combined with the angle of the radiation to the FOV. Since limb darkening should be considered in the practical sense, limb darkening approximations, $I(r)$, will be discussed in Chapter 3 and applied to the observations in Chapter 6. Further review of the effect of orbital dynamics will continue throughout this thesis.[38]

<u>*Probability*</u>[39]. A chance for detection of any transit must account for the fraction of photometry-friendly stars, that fraction detectable by the instrument, the fraction which might have a planet (ostensibly an earth-like one), the number of periods vs. observation time to produce 3σ (or ~94% Gaussian) duty cycles for first and confirming transits, the number of observations (transit curves, and the geometric probability. Since the latter relates to the precious discussion

[38] interesting details of the effect of eccentricity e upon transit events can be reviewed further in Barnes, 2007.

[39] Unless otherwise noted, 'P' means orbital period, not to be confused with 'P' when used as a probability term.

and has a central effect on detecting exoplanets, it will be introduced here as a product of the relationships discussed above; the remainder are central to most of the remainder of this thesis. For a very simple prediction estimate, the geometry as it relates to the star-planet occultation ratios is a basis for the geometric detection probability. For an Earth-like planet this ratio is an achievable ~1:10^{-4} ratio (Schneider, 1999) about sun-like stars, and an even better ratio is achievable with red dwarfs. As discussed, transits are only seen if the orbit crosses near the line of sight (LOS), where the pole axis of the given planet is less than d_*/a, with respect to the stellar center and orthogonal to the LOS[40]. Applying the probability over the whole sphere, the opportunities to geometrically transit become $4\pi\, d_*/2a$ total pole steradians on the full sphere. So in broadest terms, the probability a transit to geometrically cross the FOV for any orbit of a planet is approximated by $d_*/2a$, or simpler still, as r_*/a, if one includes grazing occultations (Borucki & Summers, 1984; Koch, 2003).

A more rigorous transit probability is presented in Chapter 6 to support the observing campaign for Gl 876. In this case, the inclination becomes an issue in this system's transit potential. In advance, the probability ($P_{transit}$) of a transit occurring can be most completely defined to be

$$P_{transit} = 0.0045\left(\frac{1AU}{\alpha}\right)\left(\frac{R_* + R_{pl}}{R_\otimes}\right)\left(\frac{1 - e\cos\pi/2 - \varpi}{1 - e^2}\right),$$

where ϖ is the the longitude of pericenter. Here, $\varpi = \Omega + \omega$, where Ω is the longitude of the ascending node and ω is the argument of pericenter; ϖ is in the reference plane from the zero point to the ascending node and then around the orbit). As will be seen, the probability, $P_{Transit}$, becomes important in assessing the utility of a given photometric target.

Section 2.E. Dust as Part of a Planetary System

While infrared (IR) studies began with balloon missions in the 1960's, detection of dust disks began with the Infrared Astronomical Satellite (IRAS)'s 1983 detection of more infrared radiation that would be expected from a nearby main sequence star, Vega (Aumann et. al, 1984). Similar excess detections were made shortly thereafter for Fomalhaut and Beta Pictoris, and later for 55 Cancri, which was the first detection of a disk in a system with a detected planet. This spectral energy distribution (SED) "excess" beyond the Planck / Wein distribution from Vega and the others was fitted to a backbody curve at a temperature of ~85K. This signal

[40] In this section, d is diameter, a is semi-major axis, and r is radius.

fit a dust signature Since then, numerous disks have been identified by radiation excess in the millimeter through infrared (several resolved), where the dust's blackbody radiation peaks.[41] While the primary goal of this thesis is to conduct a visual characterization of the planet(s) about Gl 876, it turns out that dust disk observations can notably enhance the understanding of the planets and the larger system, which is essential for the understudied M dwarf exoplanetary systems.

Further characterization of an exoplanet system can be done by correlating mass other than that of the planets, under the gravitational influence of the parent star. Bodies below the size of planets included a range of smaller bodies; at the small end, dust is a notable contributor to the dynamics of such a system, and it is often detectable by means not otherwise available to discern a planetary system's design. Dust disks are categorized into two general classes, young protoplanetary disks and older debris disks. The former is comprised of youthful material that is in the process of forming into planets. The latter is defined as mature, ~10 Myr – 10 Gyr, and is composed of 1 – 100 μm grain-sized dust, regenerated by collisions. Debris disks, therefore, are not remnants of their predecessor protoplanetary disks. This is because the parent star is old and the dust is small, with radii on the order of 100μm. Small grains have short lives due to collisions, Poynting-Robertson (P-R) drag and radiation pressure. P-R drag is a relativistic, tangential radiation-mass transfer effect, which causes inward spiraling by a subtle mass imbalance, as stellar energy is absorbed by the grains. Drag lifetimes are short at 15 Myr, and the collisions are even shorter, at ~2 Myr. Radiation pressure may blow dust clear of the system at an interval in between these intervals. In mature debris disks, dust is replenished by the grinding of larger bodies in collisions. These collision lifetimes are on the order the age of the star itself. Replenishment is what keeps the disk going, and what was sought in the observations to be discussed in Chapter 8. Details of the technique and results will be discussed there. For the remainder of this discussion, "disk" will be assumed to mean mature debris disk, applicable to the study here.

In addition to the obvious ability of images to indicate structure, debris parameters correlate, influence, and reveal other stellar parameters such as system mass, luminosity, temperature, radius, spectral type, age, metallicity, and the presence of planets. To date ~35% of the nearby systems reveal disks. This makes them a phenomenon to consider in any exoplanetary characterization.

---

41 Good reviews are found reading Moro-Martin (2007), Wyatt et al., (2003), Zuckerman (2001), and Sellwood & Goodman (1999).

Depending on the opacity of the dust within it, a disk may have the ability to infer the inclination *i* of a system, assuming the disk is coplanar to its planets, which will be discussed in detail in Chapter 8. Note that if the disk is optically thin, it no longer can be understood in terms of being a black body. Characterization of dust opacity about parent stars (and for much of this study, for M stars in particular) becomes important to the understanding of extrasolar planetary dynamics and exoplanet formation.

Also, disk systems seem to trend toward several facts. First, low-mass stars' disks last longer. Next, the larger grains in a dust disk seem to carry most of a disk's mass. As well, disks are optically thin. They are independent of uncertainties in dust temperatures, and temperatures, albedo, and thermal re-emission is not fully understood. Mass and spectral slope are often constant over time (possibly excepting gas contributions). Little excess SED attributed to the disk is from the stellar photosphere. Mass inhomogeneities in a disk can further reveal secular perturbations, resonances, librations and eddies attributed to planets or other system masses. Planets may also clear paths in disks, revealing their existence. Dust concentrations may also reveal migration effects, as the dust mass is temporarily trapped during such a migration.

A dust disk, or belt if the inner region is cleared, can be described in a geometric illustration similar to exoplanets shown earlier. The area of such a disk would be simply described by its outer radius (r) and inner radius (r_o), as $2\pi\, r\, (r - r_o)$. This leads to the dust volume, which is simply reduced from

$$4\, \pi\, r^2\, b\, (r - r_o)\ ,$$

where b is the disk cross-sectional radius. From this, volume and density can be derived, and then estimated mass. To do so requires Earth-bound observers to know the distance to the system, its spectral index, flux frequency, the typical dust temperature, the absorption coefficient, the Planck function for the dust mass, and the flux intensity.

Debris belts have held the interest of the astronomical community for the reasons described above. Some of the notable detections have been about 55 Cancrii, rho CrB, Tau Ceti, HD 100546, 141569A, HD 210277, HR 4796, HD 53143, HD 141569, HD 107146, HD 100546, Formalhaut, Stephenson 34, HD 69830, AU Microscopii, DO Tauri, Magellanic R66, R126, HD 53143, beta-Pictoris, HD 139664, and IRC+10216, to name but a few. Interestingly, IRC+10216 is noted for comet water vapor, which is particularly interesting to astrobiologists. The primary target considered here, Gl 876, is a red dwarf star which is considered to be mature (~6.5Gyr, as discussed in Saffe, Gomez & Chavero, 2005) As such, it would be an intriguing candidate for a dust study. As well, any detection would help resolve the inclination of this

system, which is debated in the literature as discussed in Chapter 6. Such a detection would also confirm or refute notions that low-mass stars beget low-mass planets, sweep planetary systems clean of dust disks, or develop resonances similar to Neptune's relationship with Kuiper bodies in the Solar system. Laughlin, Bodenheimer & Adams (2004) predict a low rate of giant planets about M stars – because the initial protoplanetary disks have lower mass than sun-like systems, and hence low escape velocities. Understanding Gl 876 dust would clarify the mass relationships with any disk and the system's three planets. A detection would provide insight to 'accretion' versus 'disk instability', the two predominant planet formation theories. As well a disk discovery would characterize the generally stochastic properties of large disks made of small dust grains. Chapter 8 discusses the thesis search in the millimeter for a dust disk about Gl 876.

Section 2.F: The Target -- The Red Dwarf & Gliese 876

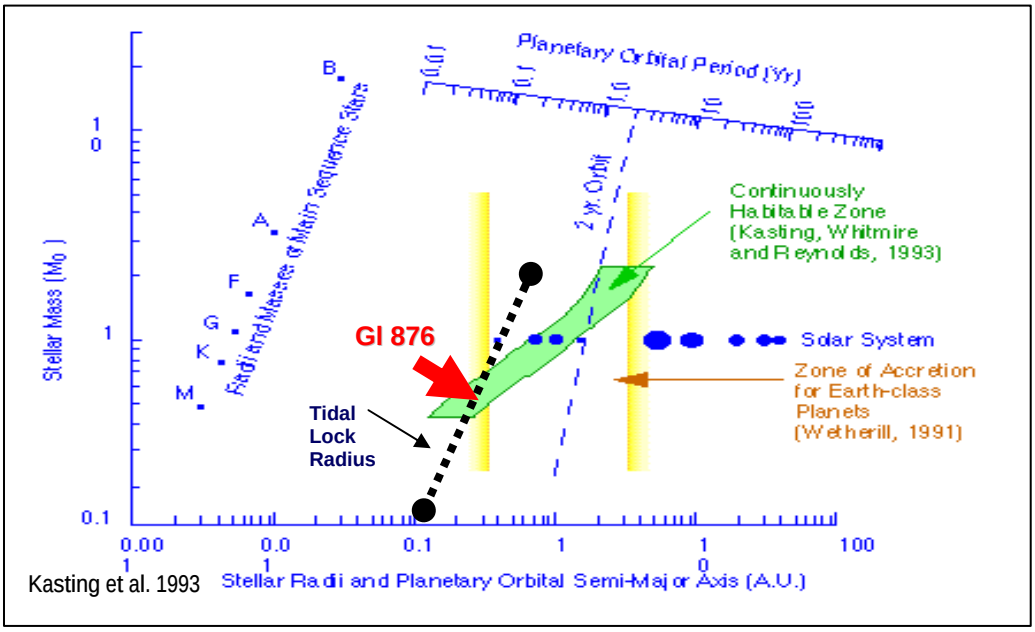

Fig. 21. This graph represents yet another perspective on how best to characterize the parameter space available, focusing on the key places of interest, modified with additional data such as the Tidal Lock Radius (Kasting et al., 1993), HZ's (Kasting, Whitmere & Reynolds, 1993), accretion zones (Wetherill, 1991), and relates them to the Main Sequence, the Solar System planets, stellar mass, radius, and planetary semi-major axis and period. While this graph was originally produced to show the places to seek "earths" about Solar-like stars, it is interesting to see where Gl 876 generally fits in (red arrow).

As main sequence stars M-class red dwarfs, such as Gl 876, still fuse hydrogen, but are not Sun-like. These dwarf stars are small, cool, and quite long lived with lifetimes of order 1×10^{13} (Laughlin, Bodenheimer & Adams, 1997). If they are unlike our Sun, given the consideration for limited human resources at hand to optimize any given study, why study them? Why study

Gl 876? Where would they be useful in defining the phase space depicted in figure 21 (Kasting et al. 1993)?

M stars are quite different from Solar-like stars, but this can provide be an advantage. First acutely, their study optimizes the probability to detect a habitable terrestrial outside the Solar system. Second, chronically, their study begins to develop an empirical, lowest-bias exoplanetary census of this very common spectral type. Red dwarfs are by far the most common spectral type in the galaxy, as an estimated 50 billion M dwarfs exist in the general census (Robin, Reylé, Derrière, & Picaud, 2003).

The commonness of M dwarfs also lends to them to being statistically, and practically, close in proximity (Bean et al. 2007). The closest star to the Sun is Proxima Centauri, and while just 0.11 M_{Solar}, Proxima Centauri's density is almost two orders of magnitude greater than the Sun's, which creates a very opaque interior. Similarly, Gl 876 is also close at a distance of 4.7 parsecs. These M stars require convection to distribute energy unlike the radiative process in Sun-like cores, and therefore quickly mix their hydrogen / helium distribution. The flux peak of a red dwarf's Planck curve is at about half the sun's 5800K surface temperature at 3250K, which combines with the mixing to make red dwarfs very log lived with little alteration in their processes and masses. Large, more massive stars suffer a quicker and more drastic fate. While intrinsically dim owing to this low and steady output, the high numbers of M stars ensure that enough have a relative magnitude less than V = 11, which sufficient for effective, modest aperture transit photometry.

Gl 876 harbors two Jupiter-massed planets, which appear to be rare for this spectral class, as predicted by core accretion theory of planet formation. According to is theory, a solid Jovian core exerts gravitational influence on the surrounding gas accreting it onto its core. Small M stars, however, would take much longer to accrete the mass required. When of sufficient mass, the gas envelope will have dissipated from which to accrete Jovian planets, and instead favor Neptune-like and smaller planets around M dwarfs. Conversely, gravitational instability, the other main planet formation theory, states that planets coalesce equally from gravitational eddies in the spiral-arm-like proto-planetary disks. The production of Jovians then would make them as common as the smaller planets. A proper census of small stars such as M Stars could discriminate between these two theories.

Such a study would also ascertain how Gl 876's two Jovians specifically play into the competing theories makes its particular study all the more useful. Accordingly, this thesis delves into this aspect of M star characterization.

Low-mass planets about red dwarfs would certainly assist in an empirical census. They certainly fan enthusiasm for a real possibility of detecting habitable terrestrial planets about nearby stars. The number of detections has begun to grow already. Along with Gl 876, planetary systems have been found about Gl 436, Gl 674, Gl 849, Gl 581 and GJ 317. Optically, the detection of planets favors red dwarfs as well. As shall be seen, detection in any habitable zone (HZ) will also favor the M spectral type.

The motivations to look at M stars for planets are many, and a review of notional Earth-habitable-zone-solar-like (EHSL) systems compared to Earth-HZ-M-dwarf (which shall be termed EHMD) systems makes this readily apparent. Notionally what defines a 'habitable zone' (HZ), is in its simplest form the belt in which temperatures favor water existing in liquid form. Of course habitability for humans requires more, such as the ability of a planet or region to retain or possess oxygen (or at least some ability to have and retain an atmosphere), or allow rocky composition[42]". In this thesis, the former, simpler definition was used to guide studies here, as this has become the simplest standard first used to narrow searches.

EHMDs have more frequent periods, meaning capturing detection (and following it up) will happen far more quickly -- by ~25 times more quickly than EHSLs. The ratio of the planet-star radii/mass is much larger in EHMDs too, which makes a transit's flux dip, as well as RV curve, more pronounced by ~15 and ~8 times, respectively. This ratio makes detecting them easier with smaller apertures and less sensitive back-end instrumentation, that is to say, cheaper, easier, and faster. M dwarfs are a statistically plentiful spectral class to study. The odds favor EHMDs threefold. This plentitude tends to offset one of the primary detractors to EHMD study, which is that they are generally dim and push limits of instrumentation otherwise suitable. The most optimized and plentiful candidates would be in the V = 15 – 19 range and require apertures larger than 3 meters for good 3-σ detection schemes. However, many good candidates exist at V less than 12, which can be assessed by sub-meter telescopes. GEMSS has, for example, targeted 149 EHMD candidates in this magnitude range.

The geometric probabilities for transits of EHMDs are also threefold higher than for EHSLs. Finally, there exists a qualitative advantage to search EHMDs, knowing the propensity of transit photometry to bedevil effective detections with high false alarm rates. Red dwarfs are generally variable; many are cataclysmic or classed in other similar variable categories. Many possess starspots, flares, flares, and higher rates of jitter. In fact, the primary target here, Gl 876, is a

[42] These additional requirements are not what strictly defines an "HZ"; that sole honor remains with liquid water.

BY-Draconis variable, which means magnitude variations of V ≈ 0.5, owing to axial rotation combined with the starspots and chromospheric activity. However, the quasi-periodic variations are on the order of fractions of a day up to 4 months, and can be effectively discounted as any signal to be confused with a transit flux. On the sub-hour transit windows that would be associated with EMHD systems, even for 2 - 4 hour Jovian transits out at 60 day orbital periods, as is Gl 876b. The shape of flux dips attributed to flairs and spots are more spike-shaped, while the ingress / egress limbs of transits have regular trapezoidal shape. These characteristics are photometrically understood in M stars and transits, generally making the weeding out of flux dips that are unlikely to be transit occultations possible.

The potential to provide a viable HZ is quite real for red dwarfs. Their zone is just much closer to the parent star than for solar-type stars. The energy from an M star is 0.05% of the Solar output owing to meager mass and temperature. To receive sufficient energy to keep water a liquid, an exoplanet comparable to Earth would need to orbit its M dwarf at a semi-major axis of ~0.02 – 0.03 AU. Kepler's 3rd law then allows the conversion of this semi-major axis to period, which is 3 to 4 days for typical M star systems. Planets so close would then be invariably circularized. More foreboding, they would certainly be tidally locked to their parent star. This concern might sound as though it were a death knell to an exoplanet's habitability, but theoretical work-arounds exist which overcome Mercury-like baking and freezing, and the freeze-out of any atmosphere as well on the dark side. Models by Joshi et al. (1997) noted a wide temperature swing, but the atmosphere did not collapse using an Earth – M star model, due to heat circulation of the oceans and atmosphere. The temperature swings, though large, remained by definition, habitable.

The geometry of such a close-in HZ would actually favor transits, up to 2.3% as opposed to ~0.9 – 1.0% for G stars. Posited geometric probabilities in Nutzman & Charbonneau (2007) offer a lower 1.6% and 0.5% respectively, but they made their calculations at 0.074 AU, near the so called *snow line*, or outer edge of the HZ. The geometric probabilities are reduced from the simple *a priori* assumptions noted earlier. Two to three detections would be possible per 100 observed M stars, which would be further improved by GEMSS-style targeting, as will be discussed in Chapter 7.

For the Gl 876 system, the two Jovian planets are participating in a 2:1 mean motion resonance, which is discussed in greater detail in Chapter 6. For Jovian planets "b" and "c", their 30.1- and 60.2- day orbits stray from classical Keplerian motion over the seven years that the Marcy-Butler collaboration (and others, see Chapter 6) have scrutinized the multi-planet radial velocity signature. This resonance makes the inner Jovian planet "c" actually precess some 40° yr^{-1},

which bears out in Monte Carlo fitting (Laughlin et al., 2005); here, the χ^2 fit confirms empirical fits.[43] Also see Appendix C for details. The question remains as to whether the resonance also drives the inclination through seasons as has been suggested in Laughlin et al. (2005) and Shankland et al. (2006). The 2003 transit observation reported herein could be attributed to such a seasonal precession, or it may have been a false positive. Chapters 4 – 6 in part study this question; the consensus remains unclear, however the author assessed that the flux dip observed in Chapter 5 was not a signature produced by any traditional imposter.

This 2003 observation was in fact planned using transit ephemeris predictions that could be produced from the Marcy-Butler RVs (cited in detail in Chapter 6 and Appendix C), using the then-3-body dynamical model available from Laughlin and Chambers (2001). Subsequent transit campaigns were privy to more constrained dynamics from 65 more RVs presented in Laughlin, Butler, Fischer, Marcy and Vogt (2005), which made global coverage of any matching transit window possible to 3σ. Orchestrating such a distributed campaign is worth reporting in its own right, as such a network offers a system of dedicated instruments which can be used to fully cover that 3σ window, and can concentrate on targets which have not otherwise been afforded large aperture telescope time. These merits and challenges to such a program are discussed further in the GEMSS discussions in Chapter 7. A discussion of precursor work, including development of the TOPhAT stratospheric and TIP-TOPhAT terrestrial instruments, is also useful to other programs. This earlier graduate work began at the University of Western Sydney, and laid the foundation, and springboard, for this dissertation. Details will be in Chapter 4 along with the other optical and radio instrumentation used.

Finally, for Gl 876 itself, its inclination is in contention. Benedictet al (2002), claimed it to be nearly edge-on at 84° +/- 6° based on astrometric HST observations of planet "b". Analysis of transit potential in the RVs, accounting for the Rossiter-McLauglin effect as discussed in Chapter 6 and Appendix C, allowed Rivera et al. (2005) and Shankland et al., (2006) to contend an inclination of ~50° is more likely. This inclination may play into any possibility of transit seasons aiding future study of its orbital dynamics. Indeed, Gl 876, as well as the local M dwarf population at large, constitutes not just an intriguing assessment of contentious orbital dynamics. This system offers a test and a foundation for working toward the first earth-like planet detected.

[43] see http://www.oklo.org for details on the Laughlin team's RV fitting engine.

Section 2.G: The Purpose of this Thesis

Scientific objectives for this thesis are:

(1) Develop means to detect exoplanet transits at low cost and useful fidelity. The initial goal was ground-based sub-meter testing for effectiveness, to be fulfilled thereafter by collecting useful photometric data on targeted RV candidates with TOPhAT and TIP-TOPhAT. Devise and test alternative photometric means to atone for shortfalls in proposed detection schemes.
(2) Report reliable transit observations of primary candidate Gl 876 as a result of TOPhAT and TIP-TOPhAT and conduct follow-up efforts via campaign efforts locally and globally to 3σ. From this, develop and orchestrate said campaign, a distributed transit network as collaborated upon with college observatories, Transitsearch[44], AAVSO. Assess results.
(3) Show the reduce and fitting of RV data in order to observe any indication of transits given by the Rossiter-McLaughlin effect; combine these with constraints posed by the light curve null detections and known orbital dynamics, and optically constrain the dynamics of Gl 876.
(4) Continue expanded modest-aperture programs for a red dwarf census and targeted characterizations, using USNO 0.61 meter instrument, Develop a distributed investigation, GEMSS. Conduct and complete Phase One, a three M dwarf test-drive, preparing for an 180-star GEMSS effort in 2008.
(5) Round out the understanding of the Gl 876 system with a dust disk evaluation. Propose and conduct collaborative millimeter dust observations at the NRAO VLA telescope in Socorro, New Mexico, and the Australia Telescope National Facility (ATNF) ATCA telescope, in Narrabri, Australia. Synthesize observations and evaluate results, further constraining the characteristics and dynamics of Gl 876.
(6) Synergize all results and deduce implications for Gl 876 and M dwarfs. Show the improved constraints developed from the observations and analysis. Discuss and plan for future exoplanet research.

The foregoing six guides were the signposts for this research throughout the process, to include the report and evaluation of results. All objectives of these guides were successfully achieved, and to that end will be the basis for the remainder of the discussion.

[44] See http://www.transitsearch.org for background.

Chapter 3: Transit Photometry

Transit photometry (see figure 22) has been touched upon briefly in Chapters 1 and 2; this chapter elaborates upon those fundamentals and describes some practical considerations for the chosen targets in this research.

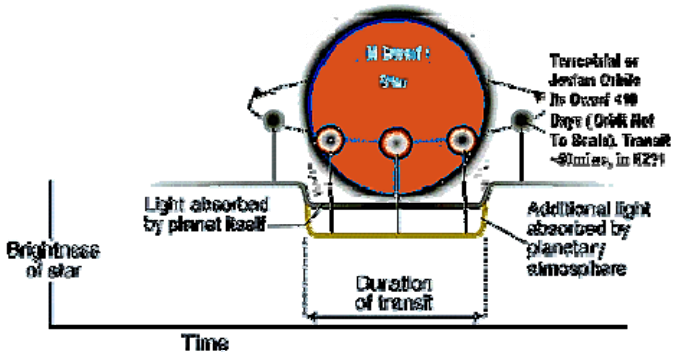

Fig. 22. Simple illustration of what occurs during transit of an exoplanet about a red dwarf. Note the flux dip caused by the occultation. Image modified by the author from Castellano et al., (2004)

Section 3.A: Photometry Applied to Observation

The practical detection of transiting planets hinges on being able to take advantage of infrequent conjunctions of (1) a well-predicted transit epoch, (2) dark, low-noise sites for observations, (3) lowered air mass which can be evaluated as found in Henden and Kaitchuck, (1990), improved seeing as described by Dainty (2003), and (5) low humidity to which both the focal plane arrays (FPAs) are sensitive, particularly in the red and IR, see Sony, 2003). Many other practical considerations; are mentioned in Appendix I. Weather plays a role in each of these and can be a lynchpin for critical observing programs. Although critical to transit photometry, useful well depth can only be identified if the exoplanet's orbit plane nearly crosses the line of sight (LOS), as discussed in Chapter 2. Here the discussion will begin with a non-traditional means to capture that photometric signal, and then progress toward the methods used to produce transit photometry in a more conventional way. Both of these approaches rely on an understanding of the orbital dynamics of the classical exoplanet transit that was described in the previous chapter.

The opportunity to observe an optical transit is most commonly available to observers whose feet are on the ground, be they at sea level or on mountains below ~8500 meters. The author had the fortune to look for photometric transits both on *terra firma*, and while airborne. Altitude offers a number of solutions to some of the pitfalls of precise photometry, and adds its own challenges. For the observations conducted in this

research, prior studies were conducted to determine operational and observational limitations to conducting precision photometry at stratospheric altitudes in aircraft. The initial investigation took place first during graduate studies at University of Western Sydney and then was continued at James Cook University. Working above the extinction and air mass problems especially problematic at the red end of the optical spectrum proved intriguing, and a tactical jet was available that could loiter in the stratosphere above 11,000 meters for periods that would cover a red dwarf exoplanet transit window. While airborne photometric methods revealed their own problems, this concept provided some interesting results. These results were particularly of an instrumental nature, and as such are discussed in Chapter 4.

As noted, ability to observe airborne at 11,000 meters helped solve some big issues for the exoplanet observer. In addition to the scientific ones noted, airborne platforms can geographically reposition themselves to optimize sky position and avoid weather. Fiscally viable applications of such a technique were explored and found achievable, so the *Tactical Observatory for the PHotometry of Astronomical Targets* (TOPhAT) was built, tested, and flown. TOPhAT produced photometric results and can be considered a success. Its limitations were primarily logistical and had to do with training limitations the U.S. Navy imposed upon aircraft operations (meteorological rules, paying for divert locations, etc.). Nonetheless, TOPhAT's unique contribution to astronomy caught the eye of the Smithsonian Institution's senior astronomer curator of the National Air and Space Museum, who has asked for its eventual inclusion into the Smithsonian collection (DeVorkin, pers. comm., 2006).

In contrast, "traditional" differential photometry is a straightforward process at least in theory; to produce imaging of adequate fidelity is more challenging. Photometry in general requires a rigor from modest instruments that is not typical but is certainly possible. Is per Chapter 2, differential photometry requires the transited, or variable star (**V**) be in the same Field of View (FOV) as the check, or comparison star (**C**), in order to determine the difference in magnitude between the (C) star and the (V), or target star. A tertiary check star (K), whose magnitude is also understood, is compared with the (C) star to ensure no variability is detected here too. To get an accurate comparison, apertures, or annuli are selected around the V, C, and K stars with each aperture containing 2 - 3 circles. The inner circle's size is adjusted to fit around the star to be

measured, while the outer circles are adjusted to include background light but not light from any neighboring stars. The radii of the annuli remain constant so as to provide a rigorous comparison between the fluxes captured within each ring. Additional factors that add to noise in the observations need to be addressed as discussed in Chapter 2.

Limb darkening, while not noise[45], *does* obfuscate the exoplanet observer's ability to detect an otherwise 'flat' occultation of a star by a planet. In order to tease out milli-magnitude flux drops caused by such a transit across the stellar disk, the effect of stellar limb darkening on the signal must be understood.

Section 3.B: Limb Darkening Parameters

Stellar disks across which exoplanets might transit are not "flat". The dimming of a star from its center to its edge, or limb, is a more complete description of what the photometrist encounters, which is termed 'limb darkening'.

Two effects cause limb darkening. First, a star's density lessens outward from the center of the star. Also, the star's temperature lessens outward from the center. The stellar density can be described as *optical depth,* a fraction from zero to unity (at the edge of the star), which increases based on the thickness of absorbing gas from which a fraction of 1/e photons can escape the star and be seen by an observer. An optical depth of unity defines the edge (or limb) of a star, where it becomes opaque. It is defined as:

$$I/I_0 = e^{-\tau}.$$

where I is observed intensity on some path, I_0 is the intensity of the radiation at the source, and τ is optical depth. In fact, summing all photons an observer sees from an optical depth of zero through one gives the the approximate radiation

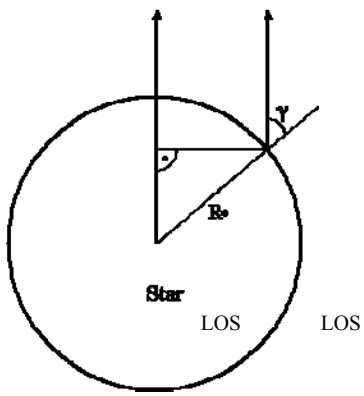

Fig. 23. Simple overhead view of the geometry of an observer per Limb Darkening -top perspective (the LOS), looking both at the center of a star, and closer to its edge. The angle gamma (γ) affects the intensity (I) gradient seen by the observer, as described in the text (see Mandel & Agol (2002).

[45] Limb darkening is an intrinsic property of a star which reveals its opacity and optical depth.

of a star. Because the angle of observation is more oblique for the photons coming from the limb (closer to an optical depth of unity), the observer sees 'into' the star at a lesser depth near the edge.

As well, the temperature of the stellar atmosphere decreases outward from the star's center (as a product of Boyle's Gas Law). Considering a star to be a black body, the Stefan-Boltzmann law (see Appendix D) then causes the regions with greater pressure (and thus greater temperature) to burn more brightly. Since the observer sees deeper into the star at the center of the disk, the denser, hotter, thus brighter region is seen at the center, than at the limb. The two synergistic effects describe what is known as *limb darkening*.

Thus, the gradient in a star's density and temperature from its core to the surface of its photosphere produce limb darkening. Specifically, variations in 'optical depth' are measured using the term τ. Here, τ is an opacity that denies or allows photons to escape the stellar interior at the threshold of $\tau = 1$. When the $\tau = 1$, enough opacity exists to cause the edge, or limb, and near this edge, the emitted photons must travel through more gas at a steeper angle from a perspective where one observes the limb. As described earlier, the radius for $\tau = 1$ increases as the LOS nears the limb. Because at $\tau = 1$ for the center of the disk the LOS penetrates deeper into the star, the observed black-body temperature will be higher and the light flux will be of greater intensity than as the LOS moves toward the edge of the disk. This approximation is complicated by the spectral emissions in stars, which disallows a perfect blackbody response, but creates non-smooth 'regions' and sometimes even brightening toward their limbs. In any event, the effect of limb darkening is best modeled based on empirical observation. Depending on the required fidelity in the detection of exoplanets, limb darkening may need to be applied in order to cull a useable signal from the available observations. Large flux variations (~5% or more) may not require considering it. Figure 23 provides a geometric depiction.

In Chapter 2 and above, limb darkening was not taken into account when performing differential transit photometry. Qualitatively, any transit curve would be expected to deepen clearly toward the center, have a somewhat flat 'bottom' as the occulting planet traverses the stellar disk, and show a gradient slope at the times of ingress and egress.

For basic detections, one might simplify reductions by not accounting for limb darkening if its effect does not degrade the light curve beyond use. However, for cases where S/N is close to the noise floor, ignoring limb darkening might cause the signal to be lost. It also skews the information gleaned in the limb passage of any exoplanet. In general, limb darkening should be considered when each photometric candidate is selected. In the case of M stars, the observationally derived quadratic limb darkening law approximates limb darkening well. See Chapter 6 for specific application in this thesis.

The Limb darkening law used in this research is the approximation

$$I(r) = 1 - c\left(1 - \mu\right) - d\left(1 - \mu\right)^2 ,$$

where r is the stellar radius, I(r) is the specific intensity as a function of r (with I(o) = 1 and μ = cos γ), and γ is the angle subtended by the LOS and a line orthogonal to a tangent to the limb. Terms c and d are the limb-darkening coefficients, which depend on the effective temperature, the stellar local surface gravity, atmospheric transmission for the observer, and the transmission of the instrument, including CCD sensitivity, filter, and primary transmission. Further discussion of their values is in Chapter 6, which follows Claret (2000).

To incorporate limb darkening into the transit flux dip of an occulting exoplanet, the above approximation is applied in a more complete fashion next, such that the flux is

$$F\left(R,\kappa\right) = \frac{\int_0^1 drI(r)\,\frac{d\left[S\left(R,\kappa\right)r^2\right]}{dr}}{\int_0^1 dr2rI(r)}$$

where the terms are described both above and follow from Chapter 2, where k is the impact parameter, S is the flux, r is the stellar radius, and I is the intensity from above. The calculation of the limb-darkening effect of the typical red dwarf revealed that for the Δ in flux depth, which is typically 5-11%, an overall limb darkening impact is 0.5 to 1%. Depending on the study effort, limb-darkening reduction may not be necessary although non-central transits may cross limb-darkened regions, and could be lost in the noise floor.

Section 3.C. General Issues of Technique

Many practical requirements must be applied to achieve quality differential photometry of exoplanet transits. While Appendix I elaborates on many of these essentials, there are a few considerations to emphasize here. Foremost and most simply, select the focal plane array (FPA) so that the pixels are matched to the foreoptic and the impinging light is close to being critically sampled (or worst case, slightly oversampled). Next, one must make and use good calibration frames, including flat frames and dark frames (the latter when not using cryogenically cooled FPAs). In addition, one must keep the target star and its check stars in the same relative positions on the series of photometric slides taken. This requires careful guiding, especially as the exposure length increases. Both of these techniques atone for imperfections in the focal plane array (FPA), dust, vignetting, and other optical path imperfections. They are requirements for detecting changes of brightness to $\Delta m \approx 0.001$.

Calibration frames must be done nightly. For this research, the routine for red dwarfs used was to expose ~20 dark frames and average them into a median master dark frame. Doing so lowers the noise floor often by 1-2 magnitudes.[46] The remainder of the FPAs used in this research were cooled by thermo-electric Peltier units and ethylene glycol circulants to 0 to – 20 C, and thus needed dark frames.

Since aperture selection (which varied) depends on scintillation and FPA critical sampling, a planatic patch of 9-15 arcsec across was used during the photometry herein, if anything to solve calculations quickly, rather than use point-spread-function fitting. Standard deviations in AIP4WIN revealed the potential for adequate fidelity on a given collection run. Statistically "averaging" results over several runs tends to reduce systematic error and potentially, accidental inclusion of variables as check stars. More than 3 nights is ideal, but practically speaking was not achievable in the time allotted, primarily due to logistical and weather constraints. Once processed, mean magnitude and standard deviation of magnitude were noted in AIP4WIN and IRAF, a quick scatter diagram validated data quality. From above, nearby check stars with suitable brightness and separation from close-by stars that might fall within the aperture annuli were used. The check stars were generally fainter than the targets, which could not be avoided for these FOVs, making their use a real test of signal to noise and image stability. Annuli

[46] As noted above, cooling the camera cryogenically reduced the dark current enough in the later-used Versarray FPA to eliminate the need to take dark frame exposures.

were selected in the 700 – 950 pixel range in the software in order to obtain the best scatter, and from there the results were recorded.

Flats can be taken using a “flat screen” at the telescope, imaging a flat FOV on an inner dome surface, or imaging the sky at twilight without tracking the stars. All three were used in various iterations for the Gl 876 and GEMSS photometry. When using TIP-TOPhAT, CCD imaging commenced at least one hour prior to the predicted ingress and extended to one hour after egress to provide a good baseline. This extension beyond the transit was rarely possible when airborne with TOPhAT in a tactical jet. For GEMSS, the process varied, but good pre- and post- transit coverage was maintained. Typically 200 to 350 images were taken of the transit event. A range of procedures were executed prior to a collection session in order to reduce errors and imprecision. For conventional photometry using normal exposures, the KAF-1602E-based CCD camera used a self-designed Glycerin/thermoelectric/refrigerated Peltier cooling apparatus to achieve a stable 0° C for improved S/N and thereby reduce dark noise, assisting the dark frames. The liquid portion of the cooling apparatus was very efficient, yet bulky, so its benefits could not be transferred to the airborne system. The exposure time for each image, typically 8 seconds was recorded from GPS/1PPS and standard cesium clock WWV signals, allowing up to millisecond precision. For TOPhAT and TIP-TOPhAT, the video signal was overlaid with the 1-PPS GPS signal so that each frame was time-stamped to an accuracy of 1 millisecond. Each of the FPAs was energized early in their photometry session so that it could reach temperature equilibrium when ready to begin dark calibration darks ~20-30 minutes. Air temperature and humidity can affect this portion of the collection noticeably and new darks must be imaged when sufficient changes to meteorological parameters have occurred.

One of the significant challenges was to find and keep the target and check stars within the proper FOV. For TOPhAT this was done by pointing an offset 532 NM laser at a pre-planned guidestar which would then put the FOV in front of the foreoptic. Further tracking was done by keeping the objects fixed on a small digital flat-screen monitor. To achieve repeatable acquisition and guiding, the system alignment must itself be built to close tolerances, so that the instrument can eliminate systematics. Some of these include periodic tracking error (P.E.), axial decoupling between right ascension and declination (or altitude and azimuth), any non-orthogonality between the two drive axes,

drive drift and slippage, and other mechanical and optical imperfections. The use of masked and cropped FOV charts became invaluable in a cockpit with TOPhAT and on the ground, and made locating dim red dwarfs and their check stars much easier no matter the observing site. More than the paper charts, real-time planetarium software views also enhanced FOV acquisition terrestrial operations; these will be discussed further.

Section 3.D. Applied Observing – Gl 876 and Onward

In order to develop adequate fidelity and signal-to-noise, to detect a well depth flux at the milli-magnitude level, calibration methods must be applied vigorously to the series of collected images. Because the goal is to maintain adequate precision and S/N to detect a transit depth with less than 0.02 V drop, an observable detection would require a resolution of a third of the transit depth for most cases. While attainable with small instruments, rigorous calibration is unilaterally mandated for transit photometry. No matter the instrument and foreoptic, one must make dark frames[47], bias and flat-field frames and average or median-combine them to produce appropriate master frames for data reduction.

To test TOPhAT, both air-borne and ground-borne, the celebrated transiting exoplanet system HD 209458, was used as a well-studied but demanding target. Novel video-rate (interline) procedures were employed in the TOPhAT instrument, which is discussed in Chapter 6. Video rate photometry has shown promise in a number of arenas and so was made part of the TOPhAT project (Barrington-Leigh, Inan, & Stanley, 2001; Durda et al., 2000; Slater et al., 1999; Christian, et al., 1985). Upscale projects may wish to take advantage of the great strides Orthogonal-Transfer CCD array technologies have made, and implement these FPAs in more elaborate photometric studies (Onaka et al., 2004; Tonri et al., 2005).

Using HD 209458 for a first test did make the procedure slightly different because it was a brighter primary for easier acquisition, but a smaller flux dip requiring very careful tracking, calibration and analysis. The images were obtained while manual and

[47] Or more precisely, reduce the dark current, which could instead be done with cryogenic cooling. However, cryogenic cooling is often unavailable to distributed teams using modest apertures, which thus means dark frames are necessary.

or auto-guiding the exposures done in all cases. When HD 209458 *was* observed, saturation became a concern due to the parent's brightness at a magnitude of V ~ 7.7. Also, the resultant short exposure times made a concern for on-axis or off-axis guiding, requiring manual intervention. These issues were actually less troublesome for Gl 876 itself since it was dimmer. In later photometry, such as with GEMSS, a separate guide scope was used which eliminated light path interference issues for the guiding-during-exposure process.

Image finder charts and check star selection charts used as guide are shown in Appendix F. These assist with the locating process, which was a non-trivial exercise for modest telescopes. The charts were used initially for orientation and verification, and later for post-production comparison. The FOVs of course required satisfactory check stars in the focal field, each of which should ideally be of very similar brightness and color to the target. Outliers had to be monitored, to reduce pixel saturation transformation errors. A major source of error to consider was Poisson noise in the object itself, which is discussed in depth later.

Multiple reference stars combined as a "mean" comparison star, which also compensates for the use of fainter check stars in fields, such as ours, often without good bright comparison candidates. Keeping the magnitude range of check stars within a $\Delta V \sim 4$ minimizes S/N degradations (Henden, 1999). When possible, averaging every star in the FOV above an S/N of 30 serves to improve the precision of the mean and reduce spatial errors, like flat-field gradients. For both HD 209458 and Gl 876, a ~25' x 25' FOV was determined to be an effective practical choice using various FOV and planetarium software schemes[48]. The success with this procedure led to its incorporation in GEMSS operations. For the larger campaigns, the FOV selection effort was done in collaboration with AAVSO[49], which produced attractive, distributed-user-friendly charts as depicted in the Appendix F.

---

[48] Which included USNO Integrated Image and Catalogue Engine (http://www.nofs.navy.mil/data/FchPix/); TheSky6 Professional (http://www.bisque.com/); Guide 8 (http://www.projectpluto.com/); Stellarium (http://www.stellarium.org/); Cartes du Ciel (http://www.ap-i.net/skychart/index.php); XEphem (http://www.clearskyinstitute.com/xephem/xephem.html); and XPlans (http://www.astroarts.com/products/xplns/index.html)

[49] Whose chart engine is found at http://www.aavso.org/observing/charts/vsp/index.html

Selection of reference stars is critical to maintain adequate precision. For the test phase using HD 209458, these check stars were desired for the inter-comparison:

HD 209458 Check Candidates	Magnitude (V)	Notes
C = HIP 108793	8.32	Wider FOV tests
C2 = TYC 1688:01903-1	11.31	In close FOV
K = TYC 1688:01716-1	10.88	All FOVs
K2 = BD+18 4914	10.63	Medium FOV
GSC 1688:1766	10.63	Tertiary
TYC 1688-1766-1	10.13	Tertiary
GSC 1688-1716	11.62	Tertiary
GSC 1688:1864	11.32	Tertiary

Easily used comparison stars were initially much tougher to find for Gl 876; the choices for the intitial TOPhAT tests were these:

Gl 876 Initial Check Candidates	Magnitude (V)	Notes
TYC5819-00963-1	10.32	Wider FOV tests
C2 = TYC5819-00963-1	10.25	In close FOV
K = TYC5819-01046-1	11.04	All FOVs
K2 = TYC5819-00419-1	12.45	Medium FOV

Subsequent Check stars for the distributed follow-ups required broader variation and so were revised to a dynamic and relative selection process[3]. These subsequent selections are shown in Appendix F. Note that easily-confused “BY” variable star 40229 IL Aqr has a ΔV which varies from 10.15 to 10.19 and is located a scant 10 arcsec northeast, while comparison star C2 is a scant 10 arcsec southwest in the FOV. This FOV challenged the smaller apertures in the network, but was more easily achieved in the 0.41 meter with the KAF-1602E and subsequent FPAs.

Traditional CCD photometry dictates long enough exposures so that flux variations due to the atmospherics and scintillation are not the prevailing source of error. Scintillation

modulates the image as an additive noise source, as with white Poisson noise[50]. Accordingly, the noise floor is "averaged downward" by using longer exposure times.

Conversely, for the test target HD 209458, while operating with either the 13-cm TOPhAT foreoptic, or the 0.41 m aperture TIP-TOPhAT foreoptic[51], the CCD would saturate in a time of just 2 to 4 s, while with the TOPhAT 8-cm Maksutov foreoptic, saturation occurred after a time of ~8-10 s [52]. During conventional photometry, adding the required V or R filter typically improved saturation times by a factor of ~6. The safe approach was to half the exposure times to achieve ~50% saturation levels and keep exposures well within the linear response region of the FPA. Henden (1998) recommends a nominal 10 seconds for most small aperture collections.

Air mass extinction becomes an issue at elevations where sec(z) = 2.0, as discussed further in Section 3.F. This is ameliorated if the collector is elevated sufficiently[53], the aperture is larger, or the optical train includes zeroeth and first Zernike-mode passive adaptive optics[54] (AO). AO zeroeth and first order (tip-tilt) optics have become accessible to modestly operating observers, but the research here relied on elevation and aperture in most cases. During initial dry runs a focusing 'curve' was discerned, which became pivotal to achieving proper focus for both airborne and terrestrial work. As a result of all testing, a mean 8-minute sequence of ten light and two dark exposures was automated into the exposure software. For interline video transfer modes the equivalent intervals were simply stacked to the same intervals and then handled the same. Interline video transfer modes were not used during the follow-up observations described in Chapter 6.

---

[50] See Section 3F for elaboration on noise issues.
[51] Called ORCA. See Chapter 4 for details about the instrumentation, such as TOPhAT, TIP-TOPhAT, ORCA, and others.
[52] It is important to note that these are saturation limits when using extended exposure times. When TOPhAT was run in an interline-transfer, video mode, the longest exposure times were 0.25 sec. Images were then registered and stacked to achieve the same signal and reduction of noise, with no saturation or smear. Interline operations also reduced transient effects (e.g.,cosmic rays hits on the FPA and moving objects in the FOV).
[53] Note that instrumentation does not affect extinction, only the thickness of the Earth's atmosphere does. Extinction is not seeing.
[54] If higher, wavefront-deforming Zernike modes are used one must model any photometric distortion effect to understand any error the higher-order AO might introduce into the observations.

Once each image was downloaded, while the next image was being exposed, dark frame and flat field calibration of the downloaded image was performed. This measured the full width at half-maximum (FWHM) flux amplitude deviations of the target star and was measured in pixel spred from the star's point spread function (PSF). FWHM in particular was useful for noting deviations in seeing and weather, and which was optimally kept at ~2.5 - 3.0 pixels[55]. Prior to each 8-min observing sequence, the telescope was pointed close to a predetermined location on the pixels, centered at (128, 128) in the focal plane. Most sequences of remained within 8-15 pixels of (128, 128), which helped to minimize errors. 40-49 sequences were completed in each transit window when using ORCA (and later in GEMSS, NOTI)[5], for example.

After collection, data reduction of all images was done using Astronomical Image Processing for Windows (AIP4WIN), and in Image Reduction and Analysis Facility (IRAF) as a cross check, in multiple differential photometry modes. Straightforward calibration and photometric reduction was then conducted by combining, or summing average darks then flats. However using 'median combine' when applying calibration frames specifically removes cosmic ray hits. It does not produce the best S/N improvement, so cosmic ray hits were sought and removed manually and median combining was usually not used. Upon collection and reduction, the data were analyzed in spreadsheets in Excel, to include graphing and basic statistical analysis.

In many cases even differential photometry with non-interline, time exposures requires shortening, and then combining, the images by stacking them. Although traditional thinking resists this alternative, the noise is after all, reduced by $\sqrt{N}$. However, the potential for misalignment (poor registration) could result in unknown contributions and an elevated noise floor. As a result this research avoided stacking when possible, and in fact registered stacking was not performed except for interline (TOPhAT) operations[56]. In real-time or video photometry performed with TOPhAT, myriad short exposures were satisfactorily averaged. The non-interline exposures were always made to be longer than a time of 2 s, in order to avoid shutter-wipe gradations on the photometric data. A further, practical limitation to stacking conventional CCD imagery is owed to

[55] Steeping the slope of the PSF curve, thus narrowing the FWHM values, will also improve focus.
[56] Still, with careful co-registration, stacking images to improve S/N ratios would give two-fold improvements in S/N, if nonlinear manipulations of data are avoided

the delay caused by the transfer of the photo-electron stream from the focal plane to the CPU. During this time the shutter is closed and neither collection nor tracking occurs. The large number of images interline-style stacking required makes the process miss frames or even fully stall, for less-than-interline rates. Because stacking offers all its advantages, this novel approach was tested once anyway, and as expected, failed. As the 16-bit images had their own advantages (and stacking so many of them would have made media storage prohibitive in size, portability, bandwidth, and cost), the chosen procedure remained the more traditional method. Registration and combining was done only with respect to calibration, and in the actual photometric reduction.

Bias frames[57] were incorporated as zero-second exposures, to assess purely read-out noise and noise caused by computer interference. More than anything, bias frames account for thermal electric currents that accumulate during image download. They established each focal plane array's zero point output and associate pixel scales to a common value so the zero points are equal and nonlinear pixel values removed. Noise in the local instruments' bias frames was small, indicating a relatively 'clean' electronic environment, and bias framing was often not separately used, allowing the dark frames to incorporate this signal. Instead values for all the pixels in a frame were averaged and applied consecutively to all frame pixels.

While flat-framing is a generally high-profile requirement[58], application of dark frames is really the most important part of calibration when seeking to achieve milli-magnitude photometry. Collected dark frames measured the thermal readout of the CCD and isolated hot pixels. To produce them, the shutter was opened but no light was allowed to impinge the focal plane. Dark frames discern the dark current emanating from the CCD alone. The research here follows (Berry & Burnell, 2000), who recommend collecting five times the dark exposure flux of the primary image. The method used with TIP-TOPhAT also involved subtracting the master bias frame from individual dark frames. The science frames were interspersed ~ hourly with integrations of dark frames. At the completion of dark collection, median-combining was performed for more than three

[57] These are exposures intended to correct for the small positive voltage added to the true signal from the CCD. It sets photometric zero point for the electronics. Dark frames, intended to capture thermal noise, also capture bias information. So as long as exposures remain the same, dark frames can be substituted in simpler reductions, and observers can zero out any bias via software.
[58] An intersesting alternative software-based method is revealed in Andruk,Vid'Machenko, & Ivashchenko (2005), using the MIDAS/ROMAFOT program shell.

frames to remove cosmic rays, in order to produce a master dark. In this way the S/N was kept to a precision below $\Delta V = 0.03$ with bias and dark framing (Henden & Kaitchuck, 1982). Generally, dark and bias frames are performed in order to correct for unwanted noise from the FPA.

By contrast, flat field integrations used to correct aberrations in the optics such as internal reflections, dust, vignetting and slight misalignments. For this reason a flat is taken each time the optical system is modified, such as for simply re-focusing. This made it the most time-consuming and rigor-challenging calibration routine. The process began with flat darks. First the dark frames, discussed above, were taken. These were then applied to the flats, ensuring that integration times matched between them. The goal for flat-field frames was to fill the electron capacity of the FPA to ~75% to reduce significant error, but keeping integration times to 10 to 20 second in order to prevent image saturation. The flat exposure intervals depended heavily on whether a V or R filter was in use for that run. With a general goal of half of the pixel full well depth for the science frames, more than sixteen flat field images were integrated per "unchanged optical train" period, in order to maximize its own signal and prevent adding noise to the final calibrated image. Once collected, all flat frames were averaged. Next the dark frames were combined by median averaging for use with the flat frames. The resultant averaged dark frame was next subtracted from the averaged flat frame, which produced the master flat. This master flat remained good for the entire observation run if the optical train was not disturbed.

Normalizing was performed if required, again removing cosmic rays and stray light as required, which are additive components. Science integration would then begin. The process would divide the master flat into each image once the dark frame subtracted it. While IRAF imaging software is versatile in certain areas such as stitching together multiple FOVs, its ability to automate calibration and photometric reduction was very limited at that time, and so was not as frequently used. AIP4WIN software was more user-friendly and allowed automation of check-star selection, registration, stacking, and reduction, which reduced processing time.

Typical frame cadence included two dark frames taken after nine science integrations, which proved to be an effective methodology in the M dwarf integrations performed

here. These nine science images were also 'boxed in' with four dark frames, which were best used by median combining them to the data frames. The result was selected in AIP4WIN to use as the final dark frame, and applied to the data.

Periodically noting the FWHM for focus, subsequent collections of three partially calibrated images were median-combined. Next, the three median-combined images were averaged. Guidance was found in a number of references, among them Henden & Kaitchuk (1990), Ghedhini (1982), Mighell (1999), Howells (2002), Henden (2001), and Gary (2002).

Detector linearity was assessed for each CCD before each instrument was used to perform exoplanet transit photometry. The procedure chosen follows Krajci (2002), Bryan (2002), and Hall & Genet, (1988). The linear range for each instrument was found to be satisfactory to 50% well depth in each case. Observations were simply kept in the linear region by remaining below 50% saturation. In rare cases limiting magnitude forced fuller use of the chip's capacity, the linear response was monitored via FWHM changes, and that data was carefully scrutinized during reduction.

Section 3.E. Other Considerations with Transit Photometry

A host of miscellaneous issues conspire against the photometrist. Although stellar variability in targets such as M dwarfs[59] would seem to be the foremost concern, the flux variability in flares and starspots is sharply peaked and easily discounted. This effect is shown in the simplified illustration, figure 24. Conversely, other variability usually has a period which is much longer that the transit, so this, too, falls outside the change in flux Δf that would serve to confuse a transit occultation.

Weather is an obvious impediment to collecting photometry, and is especially problematic in that transit predictions are for generally narrow windows owing to the dynamics of the orbital geometry discussed in Chapter 2. Seasonal weather patterns can make good results hard to obtain for long stretches of time. Meteorology is further compelling reason to distribute the observations, or take them in the stratosphere.

[59] These are especially notable for convectively-based variability and flares or starspots.

Both the global Gl 876 campaign and the GEMSS Phase I study encountered several overcast observing nights that thwarted observations during a 3σ prediction window. Many nights were affected by other atmospheric difficulties. Even during periods of clear weather, transparency or scintillation may degrade photometry to the point that the expected transit would be buried in the elevated noise. In the case of the Eastern U.S. observations at USNO, light pollution became a major problem. While differential photometry can atone for a less-than-perfect background, it cannot improve limiting magnitude, an issue with the dimmer M stars. Fortunately, the USNO 24" (0.61-m, called NOTI, see Chapter 4) had adequate aperture to extract the signal, in most cases down to V = 12.5 and sometimes V = 13.5.

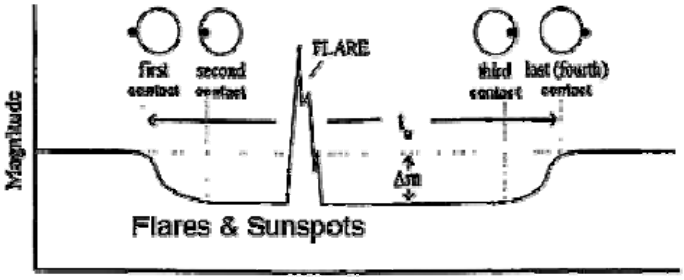

Fig. 24. Astronomical impediments to a clean detection of a classic transit curve included flares and sunspots as shown above, along with other sources of variability.

Early in the GEMSS project, the Naval District Washington Public Works department elected to build stadium lights at the South Gate, located 300 meters south of the 0.61-meter telescope. This was done without forewarning. These Klieg-style lights were intended to provide security for the base, which is coincidentally the residence for U.S.Vice President.[60] The lights made southerly observations extremely problematic until arrangements were made to turn them off when requested by astronomers. To make a compelling case, the author conducted three nights of sky darkness tests which followed Berry (1976). The data collections were performed with a standardized stellar light meter which used a TAOS TSL237S sensor[61] and M-500 filter with a 340 – 660 nm band pass, which together had an effective solid angle FOV of a wide 1.532 steradians (or 80° diameter cone on the sky). For a standardized comparison,

[60] This point of trivia ended up impacting GEMSS until remedied. The Vice President's residence is located aboard the USNO grounds, and many practical limitations to astronomy are imposed by the attendant security. See Dick (2003).

[61] See sensor specifications http://www.taosinc.com/product_detail.asp?cateid=2&proid=52 and http://www.globalspec.com/FeaturedProducts/Detail/TexasAdvancedOptoelectronic/TSL237_High_Sensitivity_Light_Sensors/13885/1

measurements were taken in units[62] of magnitudes arcsec^{-2}. With lights on, twelve equidistant measurements were made about the 3 domes at USNO and 6 inside, and these were all averaged. The lights were extinguished by prior coordination with the U.S. Secret Service each hour on the hour for 10 minutes' duration, during which time the author took the same series of measurements, and averaged these. This was done for three hours and further averaged. For the dome which houses the 0.62-m Cassegrain featured in much of the later optical research, sky darkness was reduced from 19.6 magnitudes arcsec^{-2} down to 16.4 magnitudes arcsec^{-2} with the lights on. Fortunately the tests convinced authorities to allow astronomer requests to extinguish these lights to conduct observations.

In contrast, the site used for the 2003 – 2004 observations at 15 km north of Meridian, Mississippi, provided dark skies to 20.8 magnitudes arcsec^{-2} and minimal scintillation, but sometimes offered saturated air and was fraught with summer storms and clouds. These hampered TOPhAT and TIP-TOPhAT observations. Again, differential photometry accommodates deteriorated seeing, but only inasmuch as the signal punches through the noise floor. Several nights just did not yield sufficient reducible data.

A significant difficulty in transit photometry is the lack of comparably bright comparison stars in the FOV. Currently, high precision RV surveys for extrasolar planets, which provide the high-interest stars that GEMSS seeks, require target stars with V less than 11 to obtain both maximum efficiency and 2 to 6 m s^{-1} precision. By comparison the Henry Draper (HD) catalog contains 225,300 stars, and this catalog is nearly complete to V = 9.5, giving ~5 stars brighter than 10th magnitude degree^{-2}. At even a magnitude fainter, only a few stars are still available per degree, as a mean. Some areas will be far less dense. The sufficiently bright check stars required for differential photometry are, therefore, often lacking within the FOV of even medium-aperture telescopes with typical focal planes.

Spot filter photometry is one way to overcome this limitation (Castellano, 2000) by reducing the flux from the target star to be within a magnitude of the dimmer collection of the background stars about it. Future GEMSS operations are likely to include a spot

[62] This is the brightness in magnitudes spread out over one arcsecond^2 on the plane of the sky.

filter during Phase II, which is placed close to the focal plane to reduce the target star's flux to more closely match the magnitudes of the check stars. An added benefit of any filtering is the correspondingly longer integration times help to beat down scintillation noise. Small apertures are also an advantage in heavy scintillation, as their wave front jitters entirely within the isoplanatic patch, or turbulence cell, of the FOV. Furthermore, the more complex optics required for faster focal ratios will at small aperture provide both relatively large FOVs and remain affordable to modest programs. The expected FOV for the modest GEMSS telescopes runs ~0.25 deg^2.

Section 3.F. Detection Systematics, Illusions, Precision and Errors

Noise can be considered the most significant detriment to precision photometry. Noise sources generally include aperture pixel noise, scintillation noise, seeing noise, and Poisson noise, all of which are components of stochastic noise. The types that affect terrestrial photometry foremost are Poisson and scintillation noise. Further, one must account for readout noise, sky (scintillation[63]) noise, dark noise, seeing (referenced to n_{pix}), and more. General equations are treated below, and in Section 3.F.1 as an introduction, with discussion in following sections. A comprehensive application of noise is shown in the "CCD Equation", discussed in 3.F.6. Sections following that describe other factors which degrade the photometric signal.

For the purposes of transit photometry, stochastic error is produced by a category of non-transit-related outlying random events. Scintillation is tropospheric and creates cell-like columns of wavefront interference upon the inbound celestial light. In the case of focal plane arrays (FPAs), the photoelectrons[64] that are distorted from the scintillation, are treated as random events when they reach the CCD. This effect adds to the noise of 'distracting' electrons (electrons that compete for signal status) due to thermal effects in the electronics and FPA. The result is called stochastic noise, which is treated statistically with Poisson methods. The effects are treated as collections of discrete, random events.

In the detection of exoplanets using photometry, a well-used axiom tends to be quite applicable: *precision will take priority over accuracy in order to minimize systematic*

[63] One of the drivers to fly TOPhAT was to reduce scintillation noise.
[64] Photo-electrons are the electrons released from the silicon when the photo-sites are struck by celestial photons.

errors. Notably, Jovians, M stars, white dwarf companions, and brown dwarfs all have similar radii and/or similar flux curves. In addition, partial, or grazing transits of such objects can mimic the actual planetary ones sought. Therefore, understanding the systematics confirming the errors become important to every detection. Furthermore, M stars are hallmarked as generally variable, which *sometimes* can make them imposters. Often precision photometry will reveal this type of variability to have sharp "v"-shaped floors in the flux curves. Binaries have lesser relative flux amplitudes, which are often seen more clearly in and then eliminated by RV follow-up observations. Interference from a third star in FOV can be removed by performing multiple-band photometry to follow-up any supposed detections. Multiple band photometry was performed in the follow-up observations of Gl 876. Star spots and associated quakes might also contribute to aliasing. All these hindrances must be monitored in order to achieve 1% photometry for G stars and still must be done for the 10% photometry required to detect giant planets orbiting dim red dwarfs.

In addition to understanding such physical imposters, one must understand signal imposters, which are the noise that detracts from "information". All collectors face random noise and CCD noise sources such as dark current, read noise[65], various instrumental and observational biases, and non-linearity. Interestingly, scintillation rather than shot noise marks the precision limit for bright star surveys. GEMSS would fall into that category.

Precise milli-magnitude photometry is most constrained by atmospheric scintillation, random noise, and especially, internal CCD noise (e.g., dark current and read noise). Indeed, scintillation rather than shot noise limits precision for most exoplanet transit detections. But shot and other noise effects contribute to the floor, so will be discussed in turn. Instrumental (CCD) noise sources such as read noise and dark current (unless less than ~1 electron s^{-1}), cannot be ignored.

In general, the CCD's limitations must be well understood, and aperture effects must be known. Noise may also crop up from LOS motion if one's collector moves, such as for TOPhAT airborne, for space-borne collectors, and from variations in how each star's

[65] Read noise is minimized by longer exposures over exposure stacking, and is improved by the calibration procedure described earlier

point spread function (PSF) sits atop the pixel grid comprising the CCD chip. Since a CCD is imperfect, PSFs will vary on how they impinge on the chip's pixel grid. If the position and PSF variations are relatively small, this type of noise can be all but eliminated by separating the relative brightnesses against measured star positions, and the PSFs.

Throughout this thesis, the mean or average of the noise can be described as

$$\bar{x} = \frac{1}{N}\sum_{i=1}^{N} x_i \quad ,$$

where $\mathbf{x}_i$ represents individual measurement values, and N represents a count of all measurements. Standard deviation is used to ascertain how broad a scatter is possible from any given data point compared to the average, such that the standard deviation is

$$\sigma_x = \sqrt{\frac{1}{N-1}\sum_{i=1}^{N}(x_i - \bar{x})^2} \quad .$$

The SNR (sometimes called S/N), which simply quantifies useful information in the signal above the noise, can then be related to this expected standard deviation. The SNR is understood to be

$$\mathrm{SNR} = \sqrt{C_{net}} \quad ,$$

where C_{net} is defined as the net photon count-per-target, once the image background has been subtracted, which follows Henden & Kaitchuck (1982).

3.F.1. General Error Considerations

Understanding error is a key component to assessing the accuracy of any data, especially for transit photometry which hovers just above the noise floor. The amount of signal exceeding this floor can be described in terms of system's parameters, as:

$$\frac{S}{N} = N_t^{1/2}\frac{\delta}{\sigma} \propto P^{-1/3}R_p^2 d^{-1} \qquad \begin{cases} \sigma \propto F^{-1/2} \propto L^{-1/2} d \\ \delta = \left(\frac{R_p}{R_*}\right)^2 \\ N_t = \frac{R_*}{\pi a} N_{tot} \end{cases}$$

where P is the period, R_P is the radius of the planet, and d is the distance to the system; and N_t is a value comprised of total noise (N_{tot}), the radius of the star (R_*) and the semimajor axis (a). δ is a value containing the radii of the star (R_*) and planet (R_p). Note that, the error probability σ is inversely proportional to the root of stellar flux F, or the product of luminosity (L) and distance (d). These relationships form the basis for a statistical error analysis that was performed on each set of transit data, and which produced instrument error bars. For this analysis it is necessary to determine the number of electrons above the sky count for an aperture reading. This is done by multiplying the number of counts by the specific internal gain of the CCD camera. The number of electrons above sky count is calculated as noise, where:

$$N = (counts) * (Gain) = (counts) * 2.82(e^- / count)$$

The Poisson error at 1 σ can then be determined, which is the square root of the number of electrons above sky count,

$$1\sigma = \sqrt{N} \ .$$

The Poisson error is broadly described in terms of percent error,

$$\%Error = \frac{\sqrt{N}}{N} \ .$$

The Poisson error is then used to determine the error term for the raw magnitude,

$$m \pm \Delta m = 2.5 * \log\left[1 \pm \frac{\sqrt{N}}{N} * count\#\right],$$

reduced in terms of the change in magnitude, such that

$$\begin{aligned} m \pm \Delta m &= 2.5 * \log(count\#) + 2.5 * \log\left(1 \pm \tfrac{\sqrt{N}}{N}\right) \\ \Delta m &= +2.5 * \log\left(1 \pm \tfrac{\sqrt{N}}{N}\right) \end{aligned} \ .$$

For most of the photometry described here, the statistical error bars for the magnitudes are “small”, that is, much less than 10% of the flux value. Of all the instrumentation one FPA particularly stands out for its very low noise. The Versarray 1300B CCD digital camera used for GEMSS Phase I (which is described in Chapter 4) has an extremely small random counting error, expected as it is a high performance research grade cryogenic camera.

How noise and other uncertainties are related to the data is important to the photometrist. Furthermore, the uncertainties in the photometric data are heavily dominated by biases, systematic effects and errors in the optical path(s). A treatment of such error issues will relate their effect to the quality of the data.

3.F.2. Selection Effect and Biases

The limits imposed by Dawe's Limit[66], the Rayleigh criterion[67], atmospherics, probability, ephemerides, dynamical geometries, and composition, make certain genres of exoplanets more readily detectible than others. Most of such bias is due to mass and radius selection effects. All but six of exoplanets detected as of 2007 were greater than 10 M_{Earth}, and many are much more massive than 1 M_{Jup}. Detections of such massive planets clearly does not portray a statistically significant census, but rather reveals an observational selection effect of working at the edge of 'observability', where the detection methods discussed in Chapter 2 are much more likely to discover massive planets. While such a bias makes statistical analysis uneven at best, if effort is made to account for the frequency of different classes of planets, one can see where bias is coming from. This is what GEMSS counts on, to use the biases to actually gain detections, then to note them to apply more accurate constraints on the red dwarf planetary makeup. The literature tends toward the notion that that lower-mass planets are actually more common than higher-mass ones, in accord with planet formation theories and the current detections of low-mass planets, in spite of the extreme difficulties detecting them. For example, detections are biased toward close-in orbits owing to their periodicity and greater gravitational effect, plus the ability to repeat initial detections much more frequently. For transit photometry, the geometric relationships for transit passage are especially improved. Consequently many of the detections thus far are of the short-period, high mass variety. Both transit photometry and radial-velocity methods are most sensitive to planets with small orbits. These are observational selection effects, which will be ameliorated with a greater empirical database.

---

[66] the maximum resolution, such that $R = 11.6/D$, where D is aperture in cm and R is resolving power in arcsec.

67 The empirical circular diffraction limit from the Airy disk, given by $\sin \theta = 1.22 \lambda / D$, where θ is the angular resolution, λ is the wavelength of light, and D is aperture.

Since to date, most initial detections have been by RV (six RV detections per transit detection), it remains important to understand how their biases affect transit detections. As with mass and period in transits, RVs are similarly affected. As discussed earlier, expected transit depth for G stars is ~1% and up to 10% for red dwarfs. For transits, though, the predicted transit depth, d, depends on both the planetary and the stellar radii, and since these values are detection limited, this also creates bias in the depths. Generally, a 1 to 3 milli-magnitude range optimizes any transit search based on current capabilities and understanding, while avoiding aggravation of any biases.

Uncertainties in photometry also can have a correlated component in red noise, which is considered to be a noise addition with more power in the lower frequencies, (seen in the power spectrum) than classic white noise. Red noise is usually a product of Brownian motion, and is thus sometimes called Brown noise. In the case of exoplanet detection, the Brownian motion may have produced correlated effects due to systematics in the detection scheme. This red noise was discovered as research groups strove to understand why the early predictions that many hot Jupiters (HJs) would be discovered fell short of predictions. Pont et al. (2007, 2006), found that the OGLE transit discoveries all had S/N > 40 when it was thought half or a third of that S/N would be adequate in order to detect HJs. It is suspected that the red correlation comes from weather gradients across the FOV which are correlated as are optical aberrations (Aigrain & Pont, 2007). Such an impediment were first thought to limit M dwarf detections to warm neptune-sized planets and below. However, it is the contention here that this is a concern only for surveys conducted over larger FOVs, where the gradient could influence the larger field. This bears out in the sub-Neptunian M dwarf detections in the past year. Bright targets in a narrow FOV enjoy a patch of atmosphere which does not change much over the FOV, not to mention that any optical imperfections would also matter less. Kane (2007) concurs that red noise is less of an issue when targeting single stars in a FOV, and so relegates red noise to a less urgent status: that it must be understood, but it can be overcome.

3.F.3. General Systematic Errors

In addition to random noise sources, a variety of potential sources of systematic error must be minimized. While backside-illuminated and thinned CCDs are usually best for

stellar photometry because they are less affected by intra-pixel sensitivity variations than front-illuminated CCDs, front-side arrays are the most typical CCD found in modest instrumentation. Front-illuminated CCDs have achieved precision approaching
0.01 milli-magnitudes by a broad spectrum of users as well. For front-side devices, the light transits the CCD poly-silicon parallel transfer electrodes, which are in the 'row' orientation.[68] The opacity of the electrodes leads to spatial QE[69] variations at the pixel level, which results in degradations to photometric precision.

The required maximum photometric sampling interval is determined by transit durations that generally last several hours. For a circular orbit about a 1 M~ primary, p the transit duration, td, of a planet with semi-major axis, a, is

$$t_d = 13\left(\sqrt{a/1AU}\right)\text{hr}$$

which indicates that there is a weak $t_d \propto \sqrt[3]{P}$ dependence of transit duration on orbital period. In order to be convincing, the photometric cadence must be high enough for either the planetary ingress or egress, which each extend for approximately 1/6 of the transit duration, to be well sampled. Systematic errors can easily produce trends in photometric data due to image motion or changes in air mass over a night's observing, as discussed in the following sections, but the relatively rapid changes in brightness that occurs as the planet crosses the stellar limb should dominate on shorter timescales. Furthermore, Poisson statistics indicate that the significance of a transit detection Increases in proportion to $\sqrt{N}$, where N is the number of independent photometric samples within the transit interval. Poisson errors will be discussed again below.

3.F.4. Instrument Error

Instrument error can complicate and degrade collection of useful data from a broad number of sources. Instrument errors include failing to implement color correction, not selecting comparably colored stars as differential check stars, not using a narrow-band filter, or observing using noisy equipment or equipment with inadequate mechanical, optical or electronic stability. Beyond operational challenges, practical and logistical difficulties conspire vigorously to impede a successful detection study. This potpourri

[68] The electrodes are used to clock charges to the output.
[69] QE is quantum efficiency, the percentage of photons hitting the pixels that will produce an electron–hole pair.

includes including funding, site-instrument-platform access, time allocation, transit window availability, weather obscuration, seeing and air mass, extinction, software limitations, and higher Poisson noise issues[70].

Instrumentation error includes a different set of challenges if the photometry is performed via video-rate data collection and from a cockpit, as discussed in earlier and in Chapter 4. For the airborne research, instrument error was by many means noted thus far, and was further reduced by cooling the FPA, using laser guide star stability, using de-jitter techniques, using autopilot, performing careful on-screen LCD centering; by having a FOV with check stars which are qualitatively even better (closer in color in magnitude) than for ground-based operations. Instrument error is assisted to a lesser extent by the accuracy of the GPS overlay position and time, which is digitally stamped upon the individual frames.[71] Also attention had to be given to the pointing position of TOPhAT with respect to the pilot's glass canopy. Certain portions were composed of steeply curved glass would locally distort the FOV to make the image useless. Once these systematic effects are controlled, both airborne and ground photometry can be achieved to the precision required for exoplanet detection. Also, hole accumulation diode (HAD) technology was key to TOPhAT sensitivity. Overall, S/N was improved by cooling in each of the cameras used for photometry.

In order not to introduce random noise above the 0.001 magnitude threshold during image calibration, each calibration image must also satisfy the requirement of 10^6 photoelectrons per pixel. Combined bias, dark, and flat field frames are therefore required since 10^6 photoelectrons far exceed the usable well capacity of the CCD.

In general, flux variations arising from atmospheric scintillation at low frequency can be described by Ryan & Sandler's (1998) relationship:

$$\frac{\sigma}{S} = 0.09 \frac{X^{1.5}}{D^{2/3}\sqrt{2T}} \exp(-\frac{h}{h_0}) \, ,$$

where X (often identified as sec (z) per the extinction discussion above) is the air mass, D is the aperture diameter (cm), h is the telescope altitude (km) compared to the

[70] For a good treatise, see Janes & Heasley, 1996.
[71] Everett et al. (2002) can also be reviewed for their similar address of instrumentation errors.

atmospheric scale height (h_0), and t is the integration time (s). The same $1/\sqrt{t}$ dependence is present here as is accumulated with Poisson noise. If milli-magnitude photometric precision is to be obtained, then for stars brighter than V = 8 magnitude observations from sea level, scintillation sets the lower exposure time limit. To reduce air mass effects, the non-video observations were set to never integrate above 2 min for stars at the zenith (X = 1.0), and 6 min for observations at an elevation of 48° above the horizon (X = 1.5). Exposure times of 40 s actually produced scintillation values of order 0.003 mag^2. In practice, other reasons such as saturation, linearity capped integration times well below those exposure settings.

Now ignoring dark current, read noise approaches 1 milli-magnitude for the image scale used, and this gave a notionally-optimized 8-pixel radius for apertures about stars. With a greater amount of read noise[72], apertures larger than 1-meter can actually create poor conditions for photometry, making the instruments used here 'feel appreciated'. Distributed numbers of modest telescopes would actually produce better results with regard to read noise.

Interestingly, scintillation rather than shot noise marks the precision limit for brighter transit systems. Noise may also crop up from LOS motion if the collector also moves, and from the PSF [73]. If the position and PSF variations are small, such noise goes beneath the noise floor, and can be ignored for the purposes here.

3.F.5. Poisson Noise

For transit photometry, a Poisson distribution describes the expectations for a signal, and how the finite number of "random" signals produce a measureable integer count, termed an 'analog data unit' (ADU), during the integration of the data. When an electron is dislodged by the inbound photon to be read, the FPA circuitry will read this one electron, which in turn will contribute to a specific pixel's ADU count, relative to the CCD gain.

---

[72] The author saw a range of 15 e^- in off-the shelf FPAs, versus 2 e^- in scientific-grade focal plane arrays.

[73] This is because adjoining stars fall at varied fractional-pixel displacements relative to the CCD pixel grid, and different stars sit atop different distributions of stray light from adjacent/background stars

To reach milli-magnitude precision, the measured stellar variability arising from Poisson noise, σ must be somewhere less than 0.001, as noise amplitude must of course be below the signal threshold, at 0.001 (milli-magnitude level). Poisson statistics *p* dictate that

$$\sigma = 1 \big/ \sqrt{N} \ ,$$

where *N* is the number of photo-electrons collected in the allotted stellar aperture. More than 10^6 photo-electrons are thus required for both the object star and at least one comparison star. Note that when measuring *N* stochastic photoelectrons for some image integration, the value of value *N* is really $N +/- \sqrt{N}$ events. If the gain is then applied relative to the ADU count, the fundamental uncertainty (which is the Poisson noise) is understood. As *N* increases, the effect of these various uncertainties due to Poisson noise becomes more and more moderate. This effect actually approaches a zero as the number of check stars approaches infinity. Also Poisson noise uncertainty must be orthogonally added to the Poisson uncertainty that is produced by any check stars, giving the Poisson component of RMS scatter for each image that can be expected in a final flux curve.

Shot noise is essentially Poisson noise. Shot noise can be specifically defined as the actual intensity-dependent electronic noise which occurs when the finite distribution of either (1) photons in an optical instrument, or (2) electrons in a circuit, is sufficiently small to be able to detect statistical variations in a measurement. The greater the number of electrons or photons, or signal, the smaller the relative deviations from the distribution curve, where the noise N is the actual number of photons collected. Increase in photon count (or electron count) will increase more rapidly than shot noise, which will slip below the noise floor as the signal gets “large”, so the effect is only seen at small counts of particles (i.e., faint detections like M dwarf flux variations).

3.F.6. Read + Dark Noise in Pixels

Each pixel also has its own types of noise specific to that individual pixel, and these noise sources can be combined into a single contribution *N*. The first comes from read noise from the FPA. The second source is the dark current noise. The third type of noise is produced by an elevated noise floor caused by background noise.

As additional noise contributors to the integrations, this per-pixel noise is often ‘small’ in its

contribution to the overall noise in a signal when the target is bright, the background is reasonable, and the FPA is well-cooled. For that situation, the star's flux will be uncertain. If, however, the CCD is not cryogenically cooled and when the sky is light-polluted (both of these conditions were expected when overseeing a distribution of observing sites), the effects of per-pixel noise must be considered. An average flux gives a finite noise level, which is the "read-dark noise per-pixel", or the sum of these three sources of noise, (dark current noise, sky background darkness, and readout noise).

When considering all contributions to noise, to the photometric signal, a simplistic description of signal-to-noise can be shown to be:

$$S/N = \frac{N_\times}{\sqrt{N_\times}}$$

Because the major component of the noise if from the source itself. In the real-world, however, noise has a number of additional contributors, such as:

- readout noise
- photon statistics in the signal background
- noise in the dark level
- noise resulting from digitization of the data
- photon statistics in the signal from the source

So more realistically, signal-to-noise behaves more specifically like what has been coined "the CCD Equation":

$$S/N = \frac{N_\times}{\sqrt{N_\times + n_{pix}\left(1 + \frac{n_{pix}}{n_B}\right)\left(N_S + N_D + N_R^2 + G^2\sigma^2 f\right)}}$$

where N* = number of of total e^- from the star, n_{pix} is the number of pixels being used in the sample in question, n_B is number of background pixels, N_S is the background e^- counts per pixel in total, N_D is the count of dark current e^- per pixel, N_R is the e^- readout noise per pixel, G is the CCD gain (in e^-/ADU), and σ_f is the count of the fraction lost to digitization per pixel, in ADU (Howell, 1989; Howell et al., 1996). This may be described instead in terms of standard error (in magnitudes), such that:

$$\sigma_{mag} = C\frac{\sqrt{N_\times + n_{pix}\left(1 + \frac{n_{pix}}{N_B}\right)\left(N_S + N_D + N_R^2 + G^2\sigma_f^2\right)}}{N_\times}$$

where the terms remain the same, and C is a correction term between e^- and magnitudes, such that C = 1.0857.

3.F.7. Scintillation Noise & Atmospheric Extinction

Atmospheric extinction is another consideration, which changes with location and elevation of the observations. There are three main components that cause extinction: Rayleigh scattering by air molecules, scattering by aerosols, and molecular absorption. An object's altitude is a main cause of the gradient of the extinction, and the air mass itself affects photometry most. Air mass is expressed as the product of a given standard atmospheric extinction curve by the mean air mass calculated over the duration of the observation. For exoplanet differential photometry, precision as low as 0.0008 mag has been achieved for a 9-hr series with 2-min cadence on a 1-meter class telescope (Gilliland et al. 1991). This left plenty of lattitude for the research conducted herein.

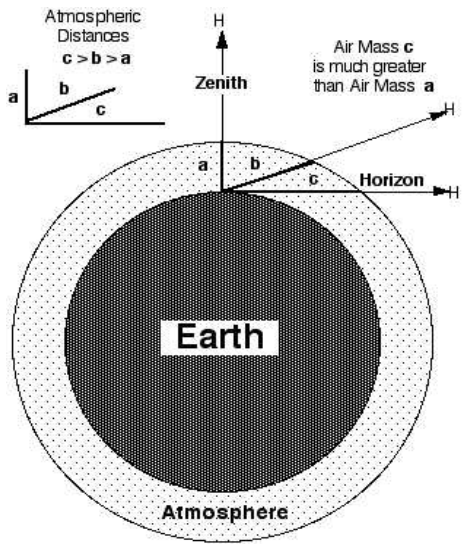

Fig. 25. A simple graphic of the effect of observing through air mass vertically, at elevation c, and vertically (though the least air mass and therefore having the least extinction)

In the global efforts, an on-line calculator was found to be useful to assist global observers making rapid, simple air mass calculations for their local photometry observations[74] (Casey, 2007). Small differences in air mass for typical FOV are understood by applying corrections for first-order and second-order extinction. See figure 25.

The first-order extinction is given by

$$v_o = v - a_v X,$$

where v_o is the target stellar magnitude as though the observer were above Earth's atmosphere, X is the air mass (sec [z]) for the observer, a_v is the V band, first-order extinction coefficient (in mag sec[z]$^{-1}$), and v is magnitude which is actually measured

[74]This can be found at http://www.briancasey.org/artifacts/astro/air mass.cgi.

for the V (or other) filter. The first-order extinction coefficient a_v is assessed by observing a star through the range of air mass altitudes. The second-order extinction depends on the color difference between the object star and a comparison star and is defined by the equation

$$v_o = v - a_v X - b_v(B - V)X.$$

In this equation, b_v is the second-order extinction coefficient in units of magnitudes per air mass per unit difference in *B-V* color. Differential photometry is largely unaffected by extinction-like effects such as small changes in atmospheric transparency due to light clouds. For observations of Gl 876 the air mass observed through was sec (z) < 2.0, and observations were based on first order approximations. Absorption as a function of wavelength is described in the idealized plot shown in figure 26; the addition of the various aspects of extinction to produce a real-time curve is represented to the right as well.

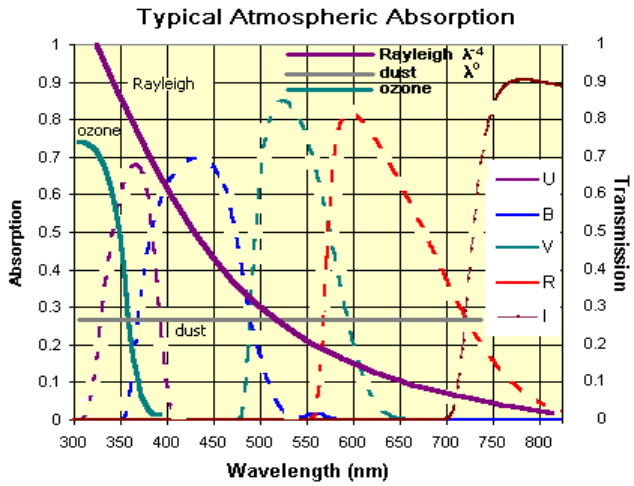

Fig. 26. Typical extinction / absorption characteristics, as compared to a UBVRI filter set, dust, etc.

Meteorological phenomena primarily occur in the troposphere, and the movement of air between high and low pressures and temperatures creates winds, as described by Boyle's Law[75]. Wind across frontal boundaries and steep gradients may not be laminar, particularly at the tropopause just beneath the stratosphere. Here, clear air turbulence is common, and these cellular density and temperature inhomogeneities cause wave front distortions to any PSF. At the base of the troposphere, the result of this scintillation is constructive and destructive interference, so that a star's Airy disk becomes distorted as lenslet-like atmospheric cells cross the LOS.

[75] From the ideal gas law, this law inversely relates volume and pressure to each other with a constant temperature.

All transit-seeking exposures were less than 20 sec exposures, making the spatial seeing differences dominated by atmospherics. Longer exposures can be more strongly influenced by imperfect tracking. In fact, one of the drivers to use video exposure rates from airborne TOPhAT was overcoming tracking challenges for an economically-derived system. Of course, longer exposures, even *with* flawed tracking, tend to beat down noise by $\sqrt{N}$. Generally speaking, systematic effects do not contribute to distortions to the flux curve, so scintillation and air mass effects are considered as noise factors here.

3.F.8. Non-Linearity and Saturation

Linearity and saturation for a given FPA must be known and avoided to produce accurate photometry. Note that, while the dynamic magnitude range is narrower for CCDs than for the celluloid film of yesteryear, CCD's offer a greater linearity (and agility) than film (see figure 27). Most imagers will identify an ADU-count of photoelectrons that converges upon saturation, usually termed "A/D converter saturation." [76] In the case of the various instruments used and discussed in Chapter 4,

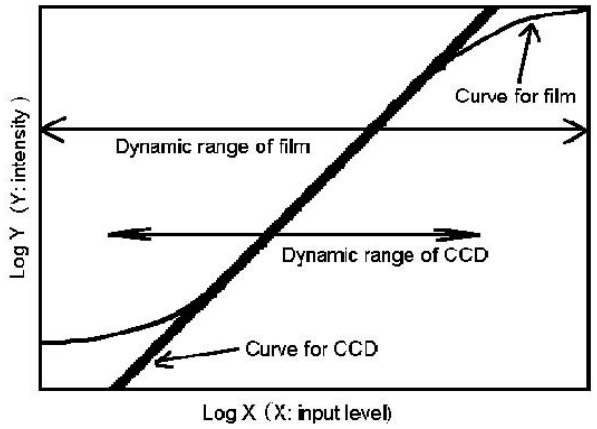

Fig. 27. Example range of current CCD technology FPAs, as compared to celluloid film. Note that, while the linearity of the CCD is greater and flatter, the input level range is less broad. Credit: St Johns College Observatory (2007).

saturation occurred between 45,000 – 100,000 ADU. Anti-blooming (AB) FPAs, which do not avoid saturation by siphoning off 'excess' photoelectrons, should usually be avoided in transit photometry, particularly in wide dynamic-range FOVs and with dim targets because the AB effect lessens the sensitivity and might distort the expected linearity of the CCD, causing noise-like effects. The transit photometrist must understand the linear region and sheer saturation occurs, in order to stay "on the line" and away from saturation. Linear response becomes questionable in many CCDs above a place on the curve approximately halfway to saturation, which makes non-anti-

[76] A/D means 'analog to digital'.

blooming (NAB) CCDs even more difficult to use on dim stars, owing to the narrower linear portion of their curve.

Again, linearity and performance tests are important. After assessing the acceptable flatness of the bias frame and to the extent to which it can be compensated for with calibration frames, a full series of calibration frames should be taken to assess linearity. In fact, full camera performance can be assessed this way including, read noise in e^-, the gain, or conversion factor, in e^-/ADU, and linearity. Taken at the cool and stable operating temperature, a bias frame is taken. Next a flat calibration image of a simple, regulated LED light source is made for the same interval and a short exposure made. Following that, a flat-dark integration is performed for same interval, but without the LED. The standard deviation (σ) results, and is measured in the bias frame, or at least the good center region. Next, the flat-dark is subtracted from one flat, and from that, the average pixel ADU in a subregion is determined. Then one flat is subtracted from another, and if necessary, a constant is added to keep values non-negative. The variance is calculated then averaged for the two frames. Then the CCD's simple gain is derived, then noise. Greater read noise accuracy requires exposing multiple test images for various times. Note that very short images may also exhibit non-linearity if the shutter is not capable of uniform exposures at fast rates).

Clearly, the issue of noise is ‘not so clear’. There are many factors to keep track of in dealing with noise, biases and error, and assuredly so for exoplanet transit photometry. The instrumentation that performs the photometry, and is used to avoid as many of the pitfalls just covered, is discussed next.

Chapter 4: The Instrumentation

Instrumentation for this thesis ranged across a broad technical spectrum, from an author built, budget-conscious optical photometer operating in the stratosphere at video rates, to radiotelescope antennas operating at millimeter wavelengths. All optical instruments were cooled from -10 to –190° C , using several methods: refrigeration, thermo-electrics, and cryogenics. The optics employed also represent a wide range of available configurations from compound and refractive telephoto lenses to sub-meter reflectors; sometimes many of these instruments were deployed as part of a larger collecting network. The following sections review the important attributes of this instrumentation starting with the *Tactical Observatory for the PHotometry of Astronomical Targets* (TOPhAT). Next, the terrestrial successor to TOPhAT will be discussed along with conventional photometric operations using the 0.41-m instrument. The USNO 0.62-m was next operated with a KAF-1602E focal plane array (FPA) first used on the 0.41-m; then other FPA's were used when the KAF-1602E-based FPA failed in 2005. These included A large-format MV interline FPA, a Photometrics VersArray cryogenic FPA, and an SBIG ST-10 FPA.

Concurrently, a millimeter study of Gl 876 constrained that system using the mass and orientation of its dust; two interferometric radio telescopes, the Very Large Array (VLA), and the Australia Telescope Compact Array (ATCA), contributed the necessary observations.

These instruments were the tools upon which the observations were made. A review of the characteristics of each instrument and the role each played, follows.

Fig 28. The TOPhAT interline video photometer. Shown with zoom telephoto, also accepted a range of airborne foreoptics from 7- to 13- cm. Foreground shows the 532-nm 30 mW guide laser, the digital inclinometer, to the right is the Sony ExView HAD FPA, ITT 3rd Gen MX-10160 Electro-optics, Peltier cooler, manual gain adapter; mounted on a digital altaz servomoter arm with dash clamps; below it, the interface box, GPS and video overlay units, batteries, and antennas; not shown; MiniDV recorder and LCD monitor

Section 4.A: TOPhAT

The author conceived, designed and hand-built TOPhAT from numerous COTS[77] components, and in some cases fabricated circuit boards (overlay, GPS, interface, gain control) and couplings. These are shown in figure 28. In addition to affordability and portability goals, it was initially designed for use in a cockpit above 10,000 meters. High altitude operations, like adaptive optics, reduce the effects of scintillation, air mass, and weather. Such locations provide access to the infrared (IR) portion radiation usually absorbed by water in the troposphere.

Compared to expensive, large-infrastructure systems such as TAC [78]-restrictive space-borne satellites or SOFIA [79] aboard a highly modified 747, this simpler project provided flexible applications, very low operating cost, and could be rapidly and easily repositioned in order to observe "targets of opportunity". TOPhAT's optical capability extends to the near-infrared (NIR) as well. TOPhAT does not use gyro-stabilized tracking or attitude maintenance, because GPS-directed-laser gyros would have increased the complexity and budget beyond practical limits. Therefore, stacked real-time images captured via video CCD were made rather than the traditional, extended CCD exposures. Specific procedures and hardware were devised to acquire and retain a given field-of-view (FOV; see sketch, figure 29), in combination with registered stacking, compensated for the lack of a traditional mount with auto-guiding. Image-stabilization, or de-jitter, software improved the video data, but it elevated the noise floor by 3% on average. This made the 1% photometry necessary to record a transit of test-target HD 209458 very difficult, but for a possible 5

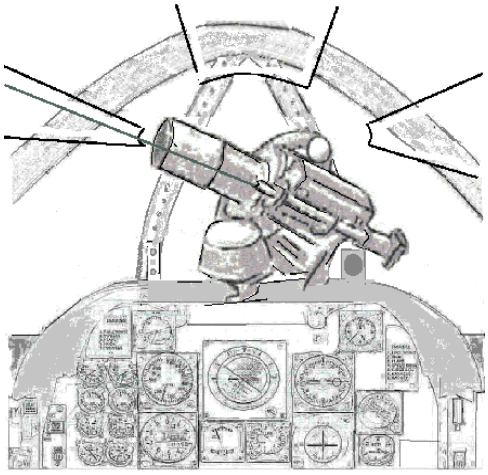

Fig. 29. Interior cockpit geometry for TOPhAT. Target star envelopes for Fields of View shown by wedges. Note TOPhAT could be clamped to either forward or aft dash for transit observations at approximately right angles (± 20 degrees) to the flight path. Elevation to the target inside the FOV envelopes would allow sighting and tracking the target, along with the offset laser. Sketch

[77] COTS is 'Commercial, Off-The Shelf'.
[78] TAC is 'time allocation committee'; refers to referee committees which adjudicate use of over-subscribed instrumentation.
[79] see http://www.sofia.usra.edu/.

to11% flux dip in Gl 876, the software was useful and did assist in image-stacking co-registration. Despite the tougher photometric thresholds posed when observing HD 209458, observations of the known transits about the sun-like star were a helpful test case because the well-established transits have a short period, which allows for methodical testing of equipment. Since being flown, TOPhAT caught the eye of the Smithsonian National Air and Space Museum's senior astronomer curator, who noted its unique contributions to practical, jet-borne astronomy. TOPhAT has been requested as a contribution to the Smithsonian archives (DeVorkin, pers. comm., 2005).

TOPhAT uses a 4 – 4000 Hz, *ExView* Hole Accumulation Diode (HAD)[80] CCD FPA, that digitally records images for later evaluation in mini-DV format, instead of using the traditional astronomical FITS [81] format. HAD CCDs reduce electronic noise due to dark current in the focal plane by accumulating holes in a separate semiconductor layer. The holes, which carry unwanted positive charge, are locations of dislodged electrons created by heat or imperfections. Trapping the holes in the separate layer that acts as a diode prevents them from returning to create noise. The specific CCD used in TOPhAT is an ICX285AL, an interline, hybrid, NIR-sensitive sensor, with small lenses annealed to the CCD that bring the light from a larger area down to the photodiode for greater quantum efficiency (QE). "Super HAD" CCDs have especially close microlenses, to increase the light collection efficiency[82] .

The ICX285AL HAD CCD chip is a high sensitivity, low smear, interlaced, progressive scan device that allows all the signal of each pixel to be output independently at a rapid ~0.067 s, while the integration frequency is 60 frames s^{-1}. This FPA has an electronic shutter with variable charge-storage time so that it can capture full-frame, still images without a mechanical shutter. It has 1.45 million, 6.45-µm square pixels, arranged in a 1392 (H) × 1040 (V) matrix. The image is overlaid with a position and 1-PPS time-stamp at an accuracy to within 1-millisec of UTC (USNO), from a GPS circuit and video interface. TOPhAT can fly with, or without, its third-generation, 18-mm MX-10160 (ITT F9800

[80] 'EXview' is a Sony trademark for a version of its HAD CCD. These devices have proprietary focal plane structure which is said to have 2X optical and 4x infrared (800-900 nm) sensitivity improvement during simple sky tests (Ferreira, 2007). In the CCD the P-N junction of each photodiode is redesigned to improve photon-electron efficiency, and each is microlensed. Visible sensitivity is increased 6dB, smear is reduced 20dB and dynamic range improves by 2dB from non ExView (Sony, 2004, 2005).
[81] FITS is 'Flexible Image Transport System'. It is a digital file format used to handle, store, and transmit science integrations.
[82] See http://products.sel.sony.com/semi/PDF/ICX285AL.pdf.

series) Gallium Arsenide (GaAs), electro-optical (EO) image-intensifier. This unit can be placed at the foreoptic's projected focus or with just the camera, at the primary focus. The image-intensifier has 64 line pairs mm^{-1} resolution, a S/N ratio of 28 to 30, spectral response between 380 and 900 nm, and a gain of 50 K; Jaenisch et. al. (2002) describe a similar instrument. Because the intensifier peaked at 775-nm at better than 25 db, it performed well in the NIR and red portions of the spectrum that are M-star-friendly. Three foreoptics, shown in the image on the previous page, were used airborne. Because the 300-mm telephoto was easy to use and had a good FOV, it was preferred whenever the targets and associated check stars were bright enough. The following guide outlines the use of the two compact apertures with the HAD CCD in intensified and non-intensified EO configurations.

Guide for TOPhAT Configurations	**300mm FL Telephoto**	**130mm Aperture Optics**	**300mm FL Tele + EO***	**130mm Aperture + EO**
Useful True FOV (degrees)	1.74	0.76	3.34 (optical) 1.39 (projected)	1.54 (optical) 0.79 (projected)
Useful lim magnitude ($m_{Lim}(v)$)	11 - 12.6	13.1 - 14.5	12.75	14.67
Useful max Resolving (arcsec) (at altitude)	2.58	1.06	4.31 (ideal) 5.16 (EO ltd)	1.96 (ideal) 2.47 (EO ltd)
Optical Aperture (m; in)	0.0536 ; 2.11	0.130 ; 5.12	Same	same
Optical eff. FL (F) (in; mm)	11.82 ; 300	25.6 ; 650.2	12.1 ; 308.0	26.6 ; 676.0
Optical eff. F.R. (f) (f/#)	5.6	5.0	5.82	5.19

* *EO transfer 5.1 cm*

TOPhAT is clamp-mounted to the aircraft dash (again refer to figure 29). It rides a computer-paddle-controlled, servomotor alt-azimuth arm. It is pointed visually with a 30mW 532-nm pointing laser collimated to the path of the science light. The laser was also used for rough tracking during turns and between integration runs. General heading was provided by GPS, and elevation was derived from an attached digital inclinometer. Once the desired FOV is recognized on the 13-cm LCD screen in the cockpit, the laser is turned off and tracking is done manually. This cadence is sufficient when very short, video-interline exposures are stacked and de-jittered. Although the green laser proved invaluable for FOV maintenance, it can only be employed with the cockpit with great care.

There were practical, temporal challenges to getting a Navy jet in the right place on time for predicted transits. If an exoplanet candidate's orbit predictions were not yet entirely clear, or it

was adjusted at the last minute, the “Capture window” (up to 1.7 hours maximum loiter time) risked not overlapping the prediction window. Fortunately any slides would still fall inside a 3 σ prediction window, and make collections important.

Fig. 30. The author, then a 20+ year aircraft carrier pilot in command of that squadron, had these T-45C Super Goshawk (foreground) and T-2C Buckeye jets available; author is in the foreground jet, leading formation on an equipment test.

Loitering above 12,000-m at maximum endurance settings pushed TOPhAT operations to their limits at times. Oxygen hoses, the HUD [83] and ejection seat equipment in the more crowded *Goshawk* sometimes conspired interfere with pointing (see figure 30, which shows the two types of jet used in this work; the *Goshawk* is in the foreground). The laser had to be used with care to avoid internal reflections. As well, at those service-ceiling altitudes, fuel-efficient loitering meant the jet was configured to fly in its most efficient configuration in very thin atmosphere, not its most stable (>20 knots faster); this made tracking more ‘intensive’., and the pilot flying had to work hard to maintain a stable platform during a 1.5+ hour window. However, as American naval captain John Paul Jones once proclaimed and is apt here, “He who will not risk cannot win” (Bartlett, 1919); or as JCU’s namesake James Cook would have it, “Do just once what others say you can't do, and you will never pay attention to their limitations again”. [84] Indeed, this video system certainly shows that subtle photometric transit detections can be successfully performed despite the requirement to overcome a number of practical hurdles.

Reduction of the photometry from a tactical jet had its own challenges, which were revealed during TOPhAT test observations of HD 209458b. Successful analysis required scrutinizing the issues of recording and data reduction, photon shot noise, detector read noise, and scintillation-limitations. Both unfiltered photometry and wide bandpass (Johnson V, further described in Persha, 1999) were compared. The dim Gl 876 pushed the magnitude limits of both conventional equipment and the TOPhAT system, but offered the possibility of a distinct 5-11% well depth for the second planet, "c". HD 209458b conversely had difficulty distinguishing a 1% well depth, but it is a system with known transits of short-period companions and is bright

[83] Heads-Up Display. Further reading on HUDs is at Pope (2006); aircraft descriptions are at http://www.naval-technology.com/projects/t45/ and http://www.navy.mil/navydata/fact_display.asp?cid=1100&tid=1600&ct=1.
[84] See http://www.brainyquote.com/quotes/quotes/j/jamescook388737.html.

enough (V=7.66 magnitude; see Chapter 3 for details) for easy tracking. It has a rapid orbital period, and the magnitude makes it easier to track.

4.A.1. Video photometry

Video photometry[85] is an extension of occultation and timing work, but requires a new level of rigor and fidelity. Although a video approach appears very different from conventional photometry, once the images are registered and stacked, their treatment is the same as the traditional transit reduction described in Chapter 3 and Appendix I. High altitude affords the researcher the ability to remove IR-absorbing water vapor, air mass, light pollution, weather and other obscuration effects that impede detections of planets orbiting red dwarfs. But unlike the large and expensive systems noted earlier, a smaller 'tactical' airborne project must compensate for its lack of long-term, stabilized tracking, which was the imperative to use real-time video CCD collection rather than traditional CCD exposures and stack of frames for adequate fidelity. Innovative data reduction procedures including jitter-removal and frame stacked flat fielding were developed to meet the demanding S/N requirement.

When airborne, the author could maintain the FOV manually by observing it on the LCD screen of the camcorder used as a data storage device. The individual interline video frames of course lacked fidelity but the stacking of these registered, short exposures not only side-stepped smear problems that would take place airborne, the procedure of stacking improved S/N greatly. This type of photometry was a viable alternative to traditional, longer exposures. Avoiding smear in the longer exposures that could be caused by traditional CCD photometry was just not possible in a tactical jet at altitude.

Oversampling challenges seemed to pose little problem for the intensifier. TOPhAT was essentially critically sampled, but with some slight leaning toward undersampling. Video rates and manual tracking reduced any effects of such undersampling. Slight defocusing also improved the S/N as related to the sampling. Also removing the intensifier was preferred if the stars of interests were sufficiently bright and the un-intensified FOV captured every check star.

The HAD[86] FPA's voltage was stepped down from 12 VDC to 9 VDC in order to control heat, dark current, and related noise further. Once a very cleanly-regulated 9-VDC power supply was

[85] In the future, a 12- to 16-bit monochrome video camera could replace TOPhAT's current FPA for excellent transit detection work; such cameras with organic image intensifiers are now available as COTS equipment.
[86] See http://www.sony.co.jp/~semicon/english/img/sony01/a6805274.pdf.

manufactured, the focal plane continued to run satisfactorily, at lower noise. A modified Sony TRV-25 MiniDV[87] camcorder was used to record data digitally. This camcorder allowed full analog-to-digital (A/D) conversion from the HAD CCD to the miniDV recorder in the camcorder itself. It also fit in the map pouch of the jet. The digital display overlay unit was attached near the camcorder in order to place time and position information in each frame. The author manufactured the display to extract 1-PPS[88] timestamps and geographic position from a GPS circuit also wired into the same box. During stacking, this time-stamp would often be blurred; but, for transiting planets, a millisecond temporal resolution was not required. The basic (and more legible) GPS time-stamp was more than sufficient for exoplanet transit purposes; such time stamps were extracted from overlays at the edges of the original frames as necessary.

During post-flight analysis and prior to calibration, Dynapel[89] *Steadyhand* software removed airborne jitter and did facilitate reduction in early test runs, in some cases. However, de-jittering was not deemed essential for tracking, and it had unknown effects on the linearity of the CCD and optics response. This was a concern for the precision of the photometry, so its use was minimized. Although the National Aeronautics and Space Administration (NASA) also designed and offered similar de-jittering software called *VISAR* [90], during TOPhAT testing the version provided was found to be rather undeveloped, and too labor-intensive to use on the amount of data TOPhAT produced.

Pixela, video digital capture software, was used to capture and manipulate the streamed MiniDV formatted science frames into single frames for any de-jitter, FITS file conversion, and stacking and post processing. *Registax*, *K3CCD*, *Astrostack,* and *AstroVideo* [91] individually provided image registration and stacking; of these, *Registax* worked best, while *Astrostack* was easiest to use. The general goals of image stacking procedures were to overcome scintillation, tracking, and jitter timescales in the short video frame exposures, achieving a signal-to-noise (S/N) that would surpass traditional imagery, and compensate for the motion of the aircraft. Once stacked, science images were handled and processed as done in traditional photometry. As expected, *AIP4WIN* and

---

[87] See http://download.css.ap.sony.com/consumer/IM/3075067621.pdf.
[88] A precision, secondary GPS signal which sends 'one pulse per second', see Caporaloni & Ambrosini (1999). Accuracy is millisecond level. 1-PPS is not to be confused with PPS, which is 'Precise Positioning Service', see http://tycho.usno.navy.mil/gpsinfo.html.
[89] See http://www.dynapel.com/.
[90] VISAR was designed to de-jitter range camera to observe spacecraft launch imagery. See http://nasa.rti.org/msfc/visar/home/index.cfm.
[91] See, respectively, http://www.pixela.co.jp/en/products/authoring/imagemixer3_mac_retail/index.html, http://www.astronomie.be/registax/, http://www.pk3.org/Astro/, http://www.astrostack.com/, and http://www.coaa.co.uk/astrovideo.htm.

IRAF provided extensive reduction and analysis tools for the stacked images. *Excel* accomplished the remaining analysis.[92]

When processing the video imagery, each individual video frame was flat-fielded as a separate, still CCD frame before co-adding them together for the final product. Recursive frame-averaging techniques were not used because doing so would threaten the known linearity of the camera. As new 'arts' in video photometry, dark and bias calibration required initial, 'creative' experimentation. The optimal method converted video into regular imagery by stacking first. Darks consisted of 10 seconds of video stream with the lens-capped camera in a dark area using the same power supply that was used during science operations.

Due to the extremely short exposure time of each video frame, bias video frames were unnecessary as long as the image size remained constant. Dark frames also include bias information. Therefore, a separate, explicit bias calibration step was not included.

For the flat fields, defocusing the lens as much as possible and scanning around the sky near the FOV for a period equal to the length of time of the planned stacked images produced adequate 'sky flats'. The pixel values at every pixel location in each of the 700 to 2000 flat frames taken, were sorted in order to discard the 20 highest and 20 lowest values. Any future variants of TOPhAT or its video-rate succesors will have automated software routines to do this labor-intensive step.

Sky flats of stacked video frames worked very well and produced very clean images Making a flat from hundreds to thousands of images rather then the dozens of conventional astronomical imaging produces excellent "flats" because noise (N) is being "beaten down" by

$$1 / \sqrt{N} \quad .$$

Media storage is a real factor in video collection because several gigabytes of streamed frames per session must be downloaded. This "fat pipe" dictates that the computing power available for proccessing be supported by generous amounts of dynamic memory, to avoid slow processing or even data loss. During this thesis, media storage has increased in accordance with Moore's law[93]; today, storage, although voluminous, is not an ordeal.

---

[92] See respectively, http://www.willbell.com/aip/index.htm, http://iraf.noao.edu/, and http://office.microsoft.com/en-us/excel/default.aspx.

[93] See http://www.intel.com/technology/mooreslaw/index.htm.

4.A.2. Airborne Operations, Techniques and Use

Because the older *Buckeye* jets had larger, flatter canopies and generously sized cockpits, these were the aircraft of choice for doing airborne photometry (figure 31). No matter the aircraft, maintaining the FOV was the most challenging and restrictive parameter, and so required quite meticulous pre-flight planning and briefing. Figure 32 reveals the limited fields available to the *Buckeye* astronomer during flight; the *Goshawk* astronomers had approximately half this amount.

Fig. 31. The author, this time in lead T-2C Buckeye aircraft during TOPhAT daytime equipment tests. Buckeyes were older but were more reliable, were more stable, had more cockpit room, flew for longer loiter times, and possessed better "look-through quality", as regards the glass canopy.

Preflight preparations included ground coordinates for track or event location, FOV optimization, dynamic altitude and azimuth calculations, holding patterns, finder charts, weather forecasts, headings and station times, and of course fuel, or time-on-station, limits. Small FOVs could create significant pointing problems. Assessing center of passage and well depth from a tactical, airborne platform was shown to be achievable. A 1.5-hour window would be adequate for capturing a predicted ingress or egress and might be sufficient for an entire Red Dwarf transit, if the geometry is favorable and a high-quality prediction available.

Image jitter is an issue to be considered with video collection from a dynamic telescope mount, such as aboard a tactical aircraft, even if the jet is on a straight-and-level, loiter profile. Extremely expensive gyro-stabilized tracking systems would have defeated TOPhAT's low-cost design goal, so software was used to remove tracking errors rather than prevent them by "stilling the platform". The *Steadyhand* software noted above performed early de-jitter operations, however in the long run was only occasionally used for this purpose, as registered stacking had the same effect and in stacking, the noise effects are known.

As discussed, concerns about increased noise as the image was "smoothed" led to skipping the image de-jitter step with *Steadyhand*, when the anticipated transit dip was to be less than 8%.

For those occasions when de-jitter was used, *Steadyhand* automatically processed the imagery on digital tracks downloaded from the MiniDV tape, to produce a cleaned digital output file. The 'non-de-jitter' option was first tested in a short terrestrial run by using the standard tracking arm, but without implementing *Steadyhand*. This run was made from a slow-moving SUV vehicle, because a truck trundling at 15 mi hr^{-1} replicated platform jitter motions similar to those found in a jet on station. TOPhAT collected red laser-glint from a ball bearing source placed atop a hangar >2 km-distant, while the instrument was operated from the rear passenger seat. Tests were performed driving along a closed, 3000-m runway. The final, qualitative comparison showed that vehicle-induced jitter did not smear pixels enough to degrade photometry more than 1-3%. Such a minor degradation while not using *Steadyhand* was overcome by more significant concerns when using it. *Steadyhand* effectively removed smearing and auto-stacked frames, but how the removed smear was accounted for was not clear, so had to be counted as additional instrument noise, also at 1-3%. So to minimize its contribution to the noise, this software was not used unless post-production required it to stabilize particular observations wrought with jitter from of a 'turbulent flight'.

Although some logistical and meteorological challenges to getting TOPHAT airborne were expected, the first-run attempt made clear that all logistical matters would require extraordinary scrutiny and preparation plus luck with the weather. In addition, TOPHAT required voluminous data reduction after each run. The system collected 10 to 20 times more frames than conventional collection, all of which had to be de-jittered, registered and stacked, and stack-calibrated before proceeding in the traditional manner. Missions were planned for 2003 August 28 and for 2003 September 2, 5, 6, and 14. All of these except for the first were flown. To work out night operations, mechanical tests of the flying procedures were done on two short late-day flights from Mississippi to Jacksonville Florida and back, on 4 August. Simple test targets included the 45% Moon (azimuth 123°, 150°; elevation 24°, 42°,

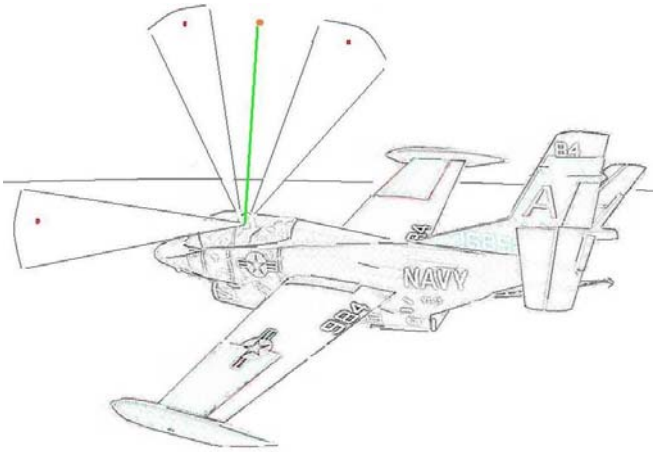

Fig. 32. External geometry of the observations using TOPhAT airborne at > 12 km in altitude. Available target star envelopes for Fields of View (in this case for the T-2C airframe) are depicted by wedges. Example acquisition and rough tracking by off-axis laser positioning shown by 532-nm, 30-mW beam. Sketch by

respectively), and the Sun (azimuth 250°, 270°; elevation 61°, 35°, respectively)[94]. Venus was attempted but was too close to the Sun, located less than 4° away.

The goals of the 28 August mission were to attempt general night variable observations and making test observations of HD 209458. Careful air planning was required because the duration of the scheduled flight would require use of all available fuel with little margin for unknowns such as surprise weather, air traffic congestion, and emergencies. The first planned flight time was to be in one of two windows: at either 04:45 to 06:20 local (~11 UTC), or 21:00 to 22:35 (~03 UTC), depending on aircraft assignment/availability. The flight would continue until one of these end times, or until conditions degraded the observations, or an exhausted fuel reserve forced a minimum-fuel landing. This first run (like successive runs) was scheduled to meet operational restrictions posed by training and safety requirements. Later flights either flew in just the evenings, or as mandated by specific transit predictions.

Obtaining military approval, including approval to use laser guiding systems, required oral and written applications that explained this unique project. These applications were followed by a subsequent oral defense of mission deconfliction, safety risk management, and the ability to simultaneously achieve other required Navy flight training objectives..

For TOPhAT, the air wing commodore approved after hours launching from Meridian Key Field, Meridian, Mississippi, U.S., which is normally open for the requisite night launches and recoveries. Briefing occurred 2.5 hrs prior to flight, and the aircrew, who consisted of the author plus another pilot [95], then would drive to the launch sight. Preflight preparations began 1 hour prior to launch, with no external ground / launch crew. Preflight checks of TOPhAT would then take place on the taxiway (as the auther performed in figure 33). In either type jet, climb to operational altitude took 20 minutes. The goal was to arrive on station (the loiter track) > 5 minutes prior to the planned-for transit prediction window. The non-standard hours dictated an uncontrolled launch and recovery. Because the tower was be

Fig. 33. Author launching prior to sunset for TOPhAT testing in a T-2C, 2003; photo by CDR M. Horsefield

[94] A solar filter was fabricated for these runs using filter material found here: http://www.baader-planetarium.com/pdf/astro_solar_information-e.pdf, which proved diffraction-limited as an optical window for these tests. The Strehl ratio (observed peak intensity of a point source to the theoretical peak at the diffraction limit) was 96.8%, as Zygo-interferometer-tested in http://www.baader-planetarium.com/pdf/astro_solar_test_e.pdf.

[95] Another veteran pilot who would tend to the flight controls during the author's tending to TOPhAT operations at altitude.

unmanned at the times using it, strictly visual weather minimums were required for legal launch until the aircrew activated an airborne clearance request. The actual tower launch would generally be radio-silent because the tactical aircraft used had radios whose band coverage did not include this tower's frequencies.

Although these conditions tested some of the mandated safety constraints (mostly fuel planning), the planned flights were each acceptable, unless and until any deplorable weather intervened. For example, on the first flight, a warning of SIGnificant METeorological (SIGMET) conditions was issued about imbedded severe thunderstorms topping 15-km, with no time to relocate the launch, so that one was aborted. Future missions with similar planning issues and requirements were, however, successful.

Pre-flight preparations included special checklists, because the flight plan included a unique profile, and the TOPhAT instrumentation required numerous pre-launch safety and operational checks. On launch, the jets were climbed at maximum performance (what is called a "Bingo climb") at an aerodynamically optimized Lift-to-Drag (L/D_{Max}) climb attitude in order to intercept a pressure-altitude (PA), slow-endurance speed of 120 knots (indicated), above 7000-m. This speed was maintained through the remainder of the climb, level-off, and fuel-conserving loiter, at 12 km altitude. This altitude was reached at 105 nautical miles downrange. Next, the pilots set the fuel burn to maximum endurance, and set to half flaps as the jets slowly accelerated to 142 KIAS as the fuel load was consumed over the next ~1.2 hr. The jet's track had to be positioned so that TOPhAT would point generally perpendicular to the flight path (over the wing), to avoid obscuration by the jet, and provide an undistorted section of the canopy (again refer to figure 32) to see through for the collection. For these flights this meant northerly 'jet route' (JR) track perpendicular to the target's calculated, dynamic azimuth. Prior to launch, trigonometric and geometric conversions of TOPhAT's expected pointing elevation and azimuth had to be calculated based on the transit predictions, as well as the location of the transit target on the plane of the sky. This was done for expected jet locations at 5 minute intervals for the duration of the loiter profile. The frequent interval proved to be "good insurance" in case of loss of target in the FOV, or during turns or other unexpected maneuvers. The mission courses themselves were calculated based on TOPhAT pointing between 20.5^{o} to 70° up from the horizon. Getting to the target was a matter of slewing the mount from the jet's indicated true north via its navigation systems, and slewing in elevation by digital inclinometer on TOPhAT.

Maintaining the Target was to be generally done by star-field recognition within a given constellation and relative to major bright planets and stars through memorized FOV charts. See the sketch on the previous page. Thereafter tracking was maintained by "laser offset", where the

laser would be directed at a preselected bright nearby object and kept there. Before flight the optical axes of the laser and the FOV were diverged from parallel collimation by a predetermined angle between the planned tracking object ("anchor") to be impinged by the laser, and the primary target. Mars proved most convenient as the anchor during most of the flights. Once tracking, the FOV was displayed on the high-resolution LCD monitor of the DV-TRV25, so that it could be recognized and kept in place to minimize jitter. The laser was then extinguished unless needed later for re-acquisition. Most routes carried TOPhAT over military operations areas which helped to avoid disruptive airliner traffic, however few of these flew nearby during TOPhAT operations.

To minimize loss of data in turns, a single, long leg would be flown northwest, followed by the reciprocal course mid-mission. This maneuver would put the jet back over the initial launch field when minimum fuel criteria were reached. Always the primary planning concern with tactical jets, fuel[96] was always closely evaluated to the nearest 10 sec. The recovery to the airfield was a 20° down-pitch, idle-throttle descent, initiated at the last possible moment at 83-km (45-nm) with 200 knots set. This steep, drop-in profile conserved the maximum amount of fuel to enable longer observations.

4.A.3. TOPhAT Upshot

Generally, TOPhAT data reduced from video images formed a statistical sample that compensated for its instrumental limitations. As a comparison, traditional photometry was attempted airborne during one mission using the KAF-1602E FPA described later.

The dynamic, and often imperfect, tracking critically hurt performance of the KAF-1602E-based camera. The slow movement of star images across traditional CCD during longer exposures increased errors due to flat field anomalies while the reverse was true in the video system with its short sequential exposures. The comparison made the viability of video stacking clear.

TOPhAT demonstrated that systems of this kind are a cost-effective means to counter air mass issues and at the same time do substantive science. Initial tests showed that TOPhAT could collect satisfactory exoplanet transit detections were the flux dip at least 5%, but preferably greater, and that both the target and check stars are brighter than 12th magnitude in either the V or R bands. On the other hand, any future incarnation of TOPhAT should include a more automated data reduction pipeline, including routines for the stacked calibrations and improved

[96] Fuel is measured in flight time remaining, as Hours + minutes + seconds.

routines for stacking the large datasets. Foremost, hardware operations would be greatly simplified through the COTS purchase of 16-bit intensified (even un-intensified) FPAs. Fundamentally, a jet airborne platform with longer endurance above 10-km altitude, e.g., a business jet, would be an important improvement to such a program. Even with these costlier additions, the program costs would not at all approach those levied by programs like SOFIA, and would operations remain more efficient and highly versatile.

Section 4.B. Terrestrially Improved Pointing – TIP-TOPhAT

Observing a transit of the fainter Gl 876 system proved quite challenging, mostly due to fewer opportunities to attempt the observation, which were frustrated by weather. The mission opportunities to fly TOPhAT were limited as well. Therefore, using TOPhAT on a terrestrial telescope offered a number of testing advantages including flexibility, expense, access, safety, and aperture, in order to understand the true viability. If anything TOPhAT proved to be easier point and track from the ground, so the terrestrial variant acquired the name 'Terrestrially Improved Pointing' TOPhAT, or TIP-TOPhAT. The 0.41-m Optical-Robotic Collecting Aperture, ORCA was the foreoptic used for TIP-TOPhAT testing both before and after the airborne program. The ORCA telescope on which TIP-TOPhAT rode was designed, fabricated, and operated by the author. It observed the un-corroborated 27 October 2003 photometric flux dip from V = 0.1187 by 0.2 as discussed in Chapters 5 and 6, which were collected using more traditional photometric means, with the KAF-1602E-based CCD camera described later and were part of the Gl 876 campaigns described in Chapter 6. Later, the KAF-1602E-based CCD camera was moved again to the more-capable Naval Observatory 0.62-m Cassegrain telescope for more transit work and eventually, for GEMSS. While the two focal plane arrays TOPhAT and the KAF-1602E are discussed in Sections 4.A and 4.C, the fore-optic for first terrestrial use of TIP-TOPhAT will be discussed here.

Fig. 34. 0.41-m f/5 Automated ORCA Telescope. Photo and instrument by the author.

4.B.1. Terrestrial Telescope – 0.41-m Optical-Robotic Collecting Aperture (ORCA)

ORCA (shown in figures 34 through 38) was designed and built to be transportable, deployable (it is rapidly moved via closed utility trailer with a telescope-specific ramp, loading winch, cot, reference

materials, spare parts, dehumidifier, camera refrigeration, and a pre-cooling unit), and it is robotic in operation.

ORCA is an f/5, 16.1-inch (0.41-m) telescope with a diffraction-limited 0.111 wavefront-error. It has a Pyrex primary, which the author ground and polished. It was then dielectric-coated to 96% reflectivity. The mechanical assembly was engineered to be stiff and lightweight in design and material composition, using composites and monocoque-style engineering where possible. The upper cage uses a novel quick-release system but is very light weight in part due to the use of heat-shrunk aircraft Monokote plastic. The light path is baffled for contrast.

The altitude-azimuth drive is controlled by machine-code level algorithms via the onboard laptop computer, which interfaces to the drives via A/D electronic interfacing and by a 17-function, lit hand paddle that can also carry a PDA[97] with additional driving software. The author-built electronics (figure 35) have a 12-VDC converter, cooling, readouts, and over-drive cutout interfacing (the interface is shown, below, right). The drives are stepper-controlled to 400 steps each, and use servo-like loops back to the software using 8000-count optical shaft encoders on each axis. The steppers are mechanically isolated and are acoustically and vibrationally insulated with laser-measuring mirrors on the axes to align their microsteps. The axes have inertial fluid-damping flywheels to improve slew and track by 70%. The motors drive 1-arcsec-precision, 300:1 worm gear rings housed in Lucite dust housings. These gears are affixed to frictionless bearing rollers. The azimuth gear is tapered to match the run-out on the azimuth plate, which uses a precise clutching assembly. The reduction gears provide additional 12:1 and 30:1 drive reduction, respectively. The optical tube assembly is built to rotate along its length to accommodate the non-equatorial characteristics of an altitude - azimuth mount.

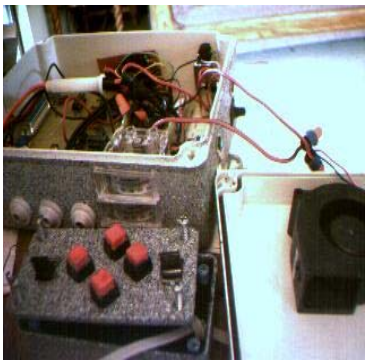

Fig. 35. Drive encoder electronics (opened), and drive padde (in foreground)

The thermal tube currents are reduced and made laminar by using six isolated high-volume fans. Four are placed behind the primary mirror and two are placed across from it. The primary cell is made to be an active-optics collimating device. This tip-tilt of the primary mirror made possible by two geared servomotors, which drive the primary for constant electro-mechanical collimation. Originally, an author-built HeNe Laser and power supply constantly checked the collimation. However, the power drain was too great, so a COTS (commercial, off-the-shelf) diode laser is now used. The cell, primary, and active drives are made to be collimation-holding, quick-release assemblies for rapid repair access. An anti-dew

[97] Personal Digital Assistant. ORCA uses this model: http://www.palm.com/us/support/tungstent/, with http://www.aho.ch/pilotplanets/

system thermostatically controls and warms all optics with thermistor control and heating cords. The mount has removable wheels for mobile positioning, electromechanical alignment and overdrive stops, and special drive-locking fixtures for transport. A Lithium-polymer battery powers the drives and laptop, and a shock-absorbing inflatable base cushion helps to smooth the trailer ride.

Auto-guiding is done with either a Meade DSI-Pro or SBIG ST-4 CCD affixed to an off-axis guider. While using TIP-TOPhAT, a separate guide scope (one is seen in figures 36 and 37) provided better results. The foreoptic for this guiding is any one of a 0.15-m f/9 reflector, a 0.11-m f/10 refractor, a 0.13-m f/12 Maksutov, a 0.21-m f/8 reflector, or a 0.20-m f /5.6 refractor. Initially the targets are found by using both these guiders and a more rudimentary unity reflex finder, a smaller 85-cm F/5 refractor and TOPhAT's 532-nm pointing laser. The laptop-run automation of the drives allows a "go-to" capability, and it permits automation of target finding and tracking sequences. Remote use is also possible via Bluetooth PDA, laptop, or computer on-line. A tube-mounted 90° wide-FOV video camera can allow the remote user a practical view of the overall sky quality during remote use. For GEMSS Phase II, some of these features will be transferred to an updated, smaller system called ULTRA (see section 4.E).

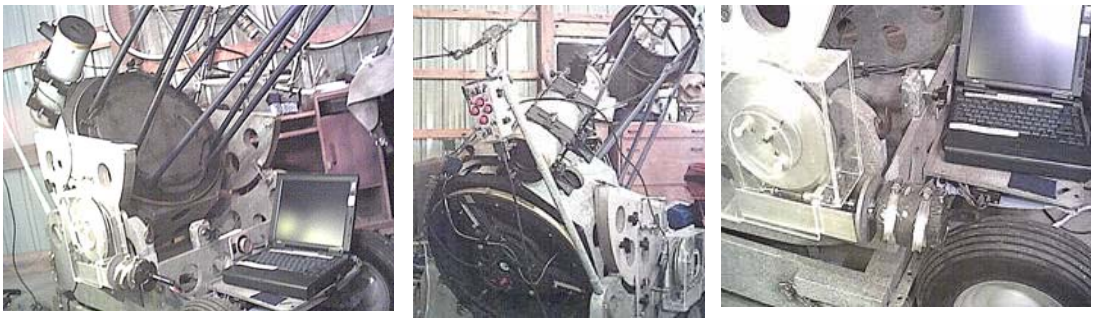

Other views of ORCA. Left(*Fig. 36*), laptop computer drives A/D interface, motors, and reduction gears. Close-up of these is seen at right (*Fig. 38*). At center (*fig. 37*), primary, active-optics, quick-release cell is seen. A 114-cm guide scope sits atop the main tube, and the paddle is slung temporarily from an access extension. All gear trains are decoupled and isolated to reduce vibration to the FPA.

For the photometric work, ORCA was primarily used with the KAF-1602E focal plane array, where this telescope played a central role in the distributed campaign to observe the possible Gl 876 transits from 2003 through 2005. KAF-1602E details are discussed in section 4C, but the initial study of transits was with TOPhAT. Its 'migration' to the ground as now, 'TIP-TOPhAT', merits additional discussion.

4.B.2. Mobile Terrestrial Operations, Techniques - TIP-TOPhAT

TIP-TOPhAT transit collections were attempted for Gl 876c on several occasions matching the system's predicted monthly cadence. However, many of the efforts were thwarted by cloud

cover while using TIP-TOPhAT[98]. Conversely, successful observations of this primary target were made using the more traditional KAF-1602E FPA by October 2003, so by then, TIP-TOPhAT testing was put on hold.

For ORCA's role as the foreoptic for both the traditional FPA and this one, observational calculations were made as the tabulations are shown in Appendix F. The FPA, TIP-TOPhAT was primarily placed on ORCA to devise the methodologies, which are discussed earlier in Section 4.A. These procedures will not be re-evaluated here, except to mention that the pointing calculations were slightly modified for TIP-TOPhAT. These calculations verified pointing algorithms, and were done to mirror airborne operations of TOPhAT as a ground testing measure, except that they were relatively stationary and not above 12 km in height. Several considerations were implemented in these calculations. Each played a bigger role on the ground in terms of observing. Foremost among these were: the primarily weather, and the scintillation/seeing conditions that a stratospheric camera was designed to fly above. Other factors were rise and set times, air mass altitude of the target, rise and set of the sun and rise, set, and phase of the moon, all based on the expected relative position of the mobile observatory. Finally, local time was converted from JD transit prediction calculations, and incorporated. Standard procedures were evolved from this initial routine to become the TOPhAT checklist.

As shown in the tables in Appendix F, a number of factors determined the quality of a predicted transit. Each chart is formulated a bit differently due to the nature of the Doppler data and transit predictions. Gl 876c showed just one ideal transit date during the available 2003 window based on instrument readiness, and unfortunately this date was meteorologically obscured by a severe cold front passage. Five attempts in 2003 were made to observe the transit of HD 209458b. These attempts were on 03 September, then 09, 16, 23, and 30 November. Incidentally the Gl 876c runs using the KAF-1602E FPA (focal plane array) also ran into weather obscuration on all but 16 and 30 November 2003. To observe a transit from a fainter red dwarf proved quite challenging for TOPhAT on the ground, even with the larger aperture. On the ground, TIP-TOPhAT lost its advantages while keeping the inconvenience of large amounts of image stacking and registration. Though the ground work demonstrated real viability for airborne work, further terrestrial use of TIP-TOPhAT was suspended in favor of traditional photometry for further Gl 876c efforts.

[98] See Chapters 5 and 6 for further discussion of observational cadence for Gl 876.

Section 4.C: NOTI -- The Naval Observatory 0.62-meter Cassegrain

Fig. 39. USNO grounds, taken by the author during trek to 0.62-m dome, 2004.

In 2004, the author had the fortune to be assigned to the U.S. Naval Observatory (winter grounds, shown in figure 39). This opportunity afforded access to observatory instruments, one of which available for extended uses was a Boller and Chivens 0.62-m Cassegrain. This telescope, which shown below, is housed in a large dome for its aperture. This dome originally housed the USNO historic 1.0-m Ritchey-Cretien, which was the last of its kind made by Ritchie. The dome and telescope served admirably as the platform for most of the observational work from 2005 to the present day. It was the test-bed for GEMSS Phase I, which is discussed in Chapter 7 and Appendix G.

The *N*aval *O*bservatory *T*wenty-four *I*nch (or *NOTI*), shown in figure 40, saw first light in December, 1971. A classic Cassegrain, its primary is a diffraction-limited, 0.10 wavefront-error, f/3 prime focus Cer-Vit[99] mirror, with a final effective focal ratio of f/13.5 and 823-cm focal length. after the 18-cm diameter hyperbolic secondary. The unvignetted FOV is 5.8-cm. The mirrors use wide-spectral response coatings to extend the ultraviolet and infrared reflectivity. The optics are housed in a 2.1-m-long baffled aluminum tube. Focusing is done by motorized axial movement of the secondary with a 12-digit counter in the warm room to ensure precise adjustment. The massive single-arm equatorial fork is run with servomotors through worm and ring gear reductions and can be controlled by paddle, console or remote paddle in the warm room. The paddle is a 9-function device. The mount is counterweighted and has overrun stops.

Fig. 40 0.62-m Cassegrain (in Bldg 39 Dome) at the U.S. Naval Observatory. Photo, J. Pepin.

The analog dials which are shown in figure 41 are built-in to the polar base and are used to read right ascension (RA), declination (Dec), and local sidereal time (LST) in hour angles (HA). The Cassegrain focus has 35-cm back room to allow use of a motorized Cousins[100] UBVRI filter wheel. Two 0.15-m f/15 refractors (see below right) are used as guide scopes or finders. One has an illuminated reticule, while for the photometry work. The author installed TOPhAT's

[99] Cer-Vit is a very hard, ultra-low expansion crystallized glass ceramic. Its expansion coefficient is 0.2 x 10^7 C^{-1}, while Pyrex is 33 x 10^7 C^{-1} and Plate Glass is 56 x 10^7 C^{-1}.
[100] Cousins and related photometric optical filter sets are treated in Persha (1999).

ExView HAD FPA for real-time guiding from the warm room. During GEMSS Phase I, an SBIG ST-4 autoguider replaced the ExView HAD, and during temporary SBIG ST-10 operations discussed in Section 4.C.4, the ST-10's onboard autoguider was used.

Fig 41. Old analog readouts (left to right) for RA, Local Sidereal Hr Angle, Dec at base of the NOTI mount. Photo, J. Pepin

NOTI's analog dials provided an additional challenge to the project, particularly to the mentored students who participated in GEMSS, as the gauges are dated and do not facilitate quickly locating celestial objects. This telescope has yet to receive upgrades to its 1970's vintage hardware, but is slated for them sometime 2008.

For NOTI, the sidereal HA dial required both a watchful eye, as it occasionally slipped and required re-setting, and it required manual conversion from hour angle to LST each time it was set, which was at least nightly. The electronics had been upgraded in the 1980's; however most of the switching is still done by slower and imprecise 110-VAC electrical relays. Also, while the optics were exceptional and the mount robust and well collimated, there was no 'GoTo' or computer control capability for NOTI. It currently also has no optical shaft encoders on the equatorial axes, which though part of the planned 2008 upgrade, would have been very useful for this research. As a result, the observational work on NOTI was done manually. Yet while the drive was antiquated the optics (seen in figure 42) were excellent. While using NOTI, the author was responsible for maintenance and repair work on the telescope during any failures, which provided additional practical education in vintage electronics.

Fig. 42. The two guide scopes and secondary with focus motor. Upper Rt guide scope carried the EvView HAD or ST-4 guiders. Photo, J. Pepin.

NOTI enjoyed a versatile back plate upon which many different FPAs could be attached. Given the number of CCD failures, this feature proved fortuitous and quite convenient. These FPAs are discussed in the following sections.

4.C.1. KAF-1602E Focal Plane Array

Fig 43. KAF-1602E-based CCD camer, based on Audine and Genesis camera formats. The CCD side is opened to see the shutter and circuitry. The peltier and liquid cooling assemblies are on reverse side (below the shutter, CCD here). Photo by author.

The first camera attached to NOTI was an author-built peltier-and-ethylene glycol-refrigeration-cooled KAF-1602E camera, shown, opened in figure 43. The camera was designed based on the Audine and Genesis formats. It was built with a mechanical shutter, passive dehumidifiers, and USB[101] and parallel data transfer capability. The CCD chip can operate in half-frame mode and work as if electronically shuttered, almost at video rates. This option would be explored in future low-cost variants of an upgraded TOPhAT. This camera used the 1.6 megapixel KAF-1602E CCD, which contains 1536 (H) x 1024 (V) 9-micron pixels, each with an output sensitivity of 10µV/e-, a dark current of ~ $1e^{-}$ $pixel^{-1}$ s^{-1} when cooled to 0° C, a quantum efficiency (QE) of 35%. The camera load is 80k e^{-}, while its full well is at ~100k e^{-} with an output sensitivity of 10 µV/e-. The read noise is tested to be 13 e^{-} with a dynamic range of 76 dB. Non-linearity is 1%, which is important to transit work. This CCD is non-anti blooming (NAB). As indicated, the camera can be cooled by thermo-electric Peltier alone, or the camera's water block, glycol lines, radiator and refrigerant can be activated as well. This drops the dark noise further, from the Peltier-only temperature which stabilizes at a mean -12° C, to a final, collective -50°C.

Fig. 44. QE curve for KAF-1602E CCD. Credit: Kodak

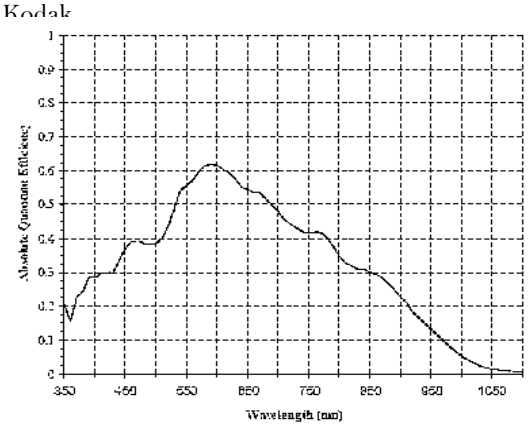

The QE response in this CCD is fairly good for a front-side illuminated FPA. See the QE curve, figure 44, which gives a qualitative understanding of response and an empirical one of efficiency. M dwarf flux dips would not be a problem to detect. The camera was operated using alternatively, *Pisco*, *Iris,* and *Aud'Ace* software [102], and the integrations were collected directly as FITS [4] files.

[101] USB stands for Universal Serial Bus, which is designed to be a legacy-free, plug-and-play computer port.
[102] See respectively, http://www.astrosurf.com/audine/English/pisco/, http://www.astrosurf.com/audine/English/iris/iris.htm, and http://www.astrosurf.com/audine/English/audace/xiw3223b/webpages/audace/audace.htm

This camera worked well through 2005, when electronic synchronizing and amplifier problems required it be shelved until it could be repaired. In order to continue research in 2005, an interim solution was sought, that resulted in the eventual use of three more FPAs over the following months.

4.C.2. Illunis MMV-11000 Large-Format Interline FPA

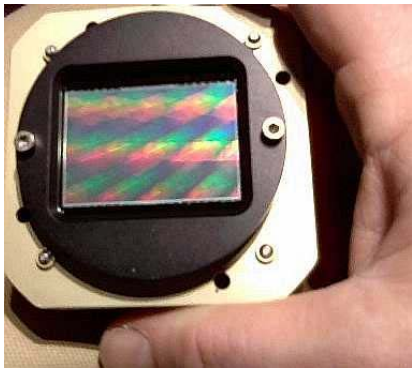

Fig 45. Large-format KAI-11000 FPA, shown while MMV-11000 imager head was opened for potential repairs. Photo by author.

A second camera was borrowed from A. Hajian who was then at the USNO, when the KAF-1602E device was shelved. Shown in figure 45, this camera was an Illunis Argon-coated model MMV-11000 CCD device which had 9.0 µm square pixels, but arrayed as 4072 (H) x 2720 (V) on its large 35-mm-style, 11.1-megapixel interline-progressive scan KAI-11000 chip. The camera's dynamic range was 60 dB and was primarily a high-fidelity scientific video device with a maximum frame rate of 5 frame s^{-1}, with available integration times between 0.001 and 3600 s. It had an adjustable gain range of 2 - 40 dB, an output depth which was 12-bit, and was anti-blooming (AB). The latter was a drawback, but in this arrangement, exposures were expected to be short, keeping collections in the linear response region of the FPA. This camera touted a low dark current of less than 50mV s^{-1} plus a reasonable 30 e^- noise, a 13e^- RMS read noise with *no* active cooling, and low video smear which remained below -80dB. Image saturation occurred at 60k e^-. The FPA's QE was at 50%. Note the QE curve (figure 46), which indicates this CCD has a improved blue response while keeping good red response which is needed for M dwarfs. The FPA was controlled with Illunis' proprietary software, and required conversion to FITS formats.

Fig. 46. QE Curve for KAI-11000 CCD. Credit: Kodak

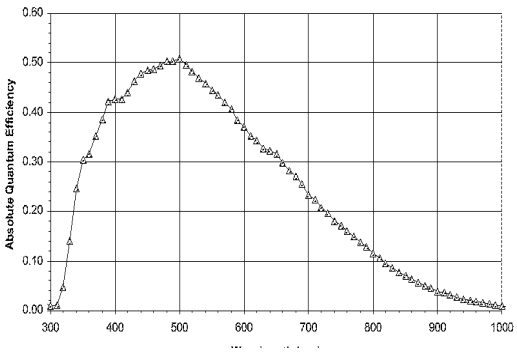

The real advantage to use of this chip was its immense real estate, although full still frames took a very slow 26 s to serially download. Unfortunately this camera had electronic problems, too. In this case the power lines feeding the FPA failed. With little time available to troubleshoot its problems, this FPA was shelved after three weeks, and other interim solutions were sought.

4.C.3. Princeton Instruments VersArray Cryogenic FPA

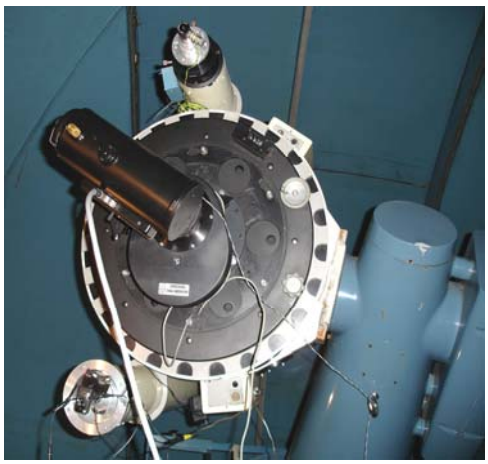

Fig. 47. Cryogenic Princeton Instruments Versarray FPA in use on NOTI. Photo by J. Pepin

A third CCD imager, the VersArray, shown in figure 47, was then found and employed on NOTI, which turned out to be a well-suited, high-quality match for M dwarf exoplanet photometry. This instrument was indefinitely loaned to the USNO by the U.S. Naval Academy's (USNA) Physics Department. It had been purchased 4 years prior for their 0.5-m Cassegrain, but the mating telescope and rooftop dome suffered in a hurricane, so the entire instrument had been crated until reconstruction funds became available. This loan allowed this FPA to return to useful science.

Made by Princeton Instruments, this model is the VersArray 1300B. Its FPA is a zero-column-defect, thinned, back-illuminated CCD with 1340 (H) x 1300 (V) 20-micron^{-2} pixels, and is cooled with liquid nitrogen (LN2) cooling system. The current instrumentation at the main USNO site all use thermo-electric and refrigerant methods, so the USNO had to institute new local handling procedures for cryogenics.

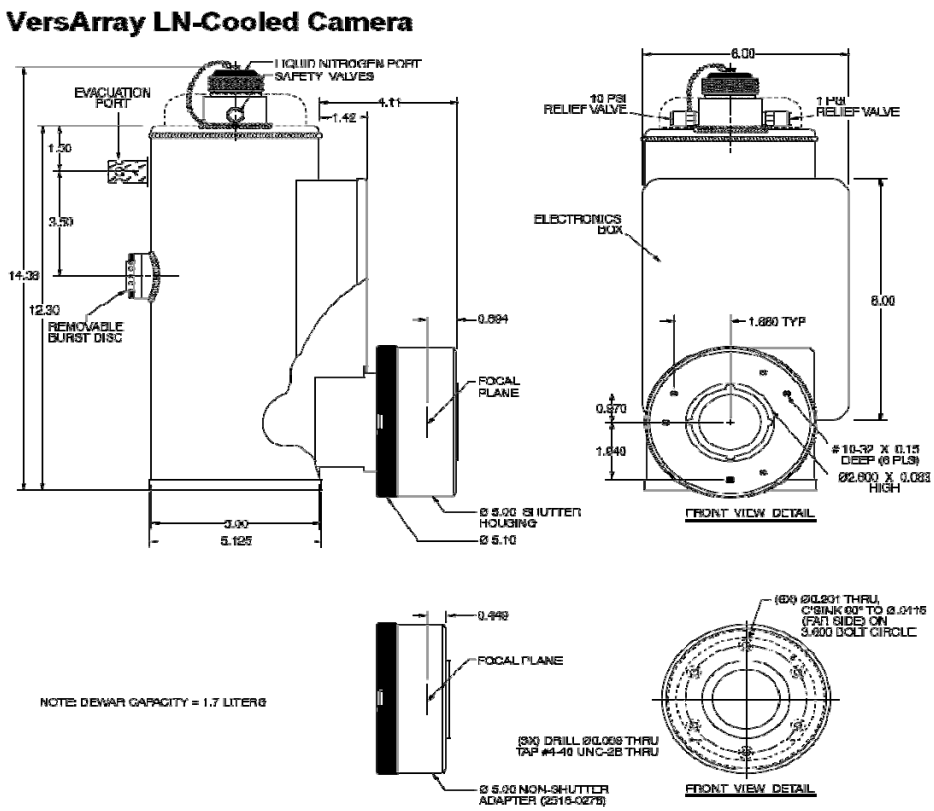

Fig. 48. Drawing of Versarray camera body. Credit: Princeton Instruments

The camera's shutter faceplate, shown in figure 48 above, fortuitously mated directly to the NOTI's 15-mm Cousins *UBVRI* filter wheel with zero modifications. This FPA provided noise typically of 8 e^- RMS at 0° C, negligible dark current using liquid nitrogen (LN2) cooling at a thermostatic -110°C with a ±0.05°C precision. At operating temperatures, the camera produced 1 e^- $pixel^{-1}$ hr^{-1} noise, with a 1-MHz gain of 2.82 e^- per count.

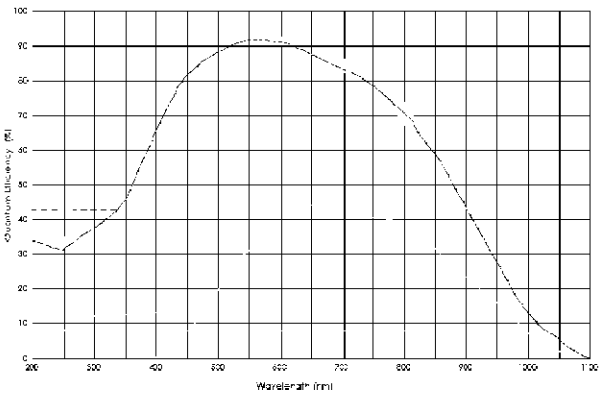

Fig. 49. QE of back-illuminated, thinned CCD36-40 with UV coatings (dashed straight line). Here cooled to -10° C.

The Versarray's EEV CCD36-40, a scientific grade 1, back-illuminated CCD had very low noise, high-capacity preamplifiers and a QE greater than 90% QE, as shown in the curve, figure 49. The Versarray had a 16-bit readout at 1-MHz, and took just 1.8 s to read and display a full frame at 1-MHz, owing to the intermediate ST-133 Controller and parallel A/D PCI interface. The acquisition software was proprietary and unusual, in that it controlled the camera well, but acquired images in TIFF format. This required the observer to convert from TIFF to FITS formats manually in order to perform calibration, processing, and photometry. The 0.75 liter dewar, shown in figure 50, allowed greater than 13 hr operation on one fill. It was a 360°, spill-resistant model that could withstand odd orientations while riding equatorially. The dewar was filled via another small 1-liter portable dewar, which itself was topped using a 10-liter refrigerated stowage dewar that a local chemical company re-filled twice a week during full GEMSS operations.

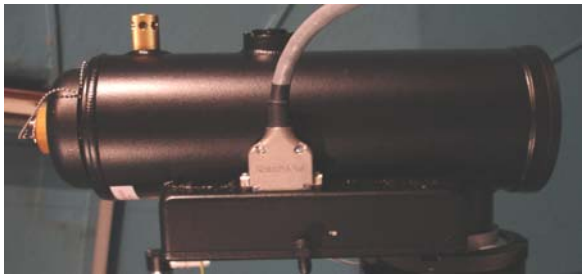

Fig. 50. Close-up of Versarray's 360° LN2 dewar and interface. FPA and shutter are below right. Photo by J. Pepin.

4.C.4. SBIG ST-10 ME FPA

Fig. 51. ST-10 Camera body. Credit: SBIG

For 4 months, the VersArray also failed after nearly a year of reliable operation. Having lost vacuum, it was returned to the manufacturer for service. Unfortunately the failure occurred during a period scheduled for GEMSS Phase I operations. So during that time, the USNA also loaned the USNO a Santa Barbara Instrument Group (SBIG) ST-10 ME camera, shown in figure 51. This camera was perhaps the most automated and easy to use of all the FPAs, but second to the VersArray in terms of the ability to produce the best precision, milli-magnitude photometry. The imager contains an enhanced, zero-column-defect, 3.2-megapixel KAF-3200ME science blue-plus CCD with a mechanical shutter. The chip has 2184 (H) x 1472 (H) 6.8 micron^{-1} pixels. The on-board auto-guiding FPA, a TC-237H, has 657 (V) x 495 (H) pixels. The ST-10 uses a USB interface, a 16-bit A/D converter, and it uses a thermo-electric heat exchanger to a regulated -45° C. The FPA had a dark current less than 1e- pixel^{-1} s^{-1} at 0° C. The QE was greater than 85%, as shown in the graph, figure 52. This is even though the KAF-3200ME is not thinned or back-illuminated. As well, red response is strong, and data transfer is fast, at 425k pixels s^{-1}. The camera was operated using *CCDSoft*,[103] which collected images in FITS format. For these operations, the Cousins filter set already in use was continued in lieu of operating its color filter wheel.

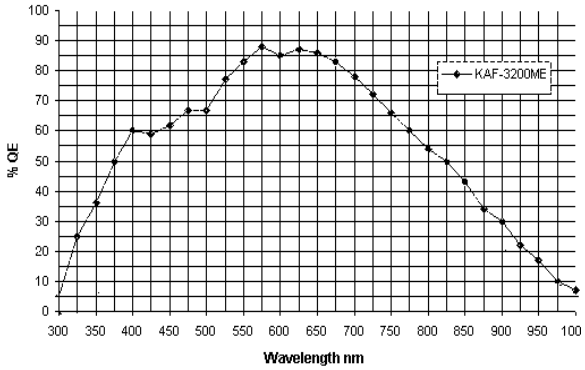

Fig 52. QE Curve for KAF-3200ME CCD. Credit: Kodak

Section 4D: Radio Observations in the Millimeter

Moving between HE, optical, IR, and radio observation is the hallmark of the third-millennium astronomer, whose interests are to optimize his / her pan-spectral understanding of the selected target – irrespective of wavelength. Notwithstanding, practical understanding of observational astronomy is a 'shifting of gears' when it comes to operating to collect optical photometry vs. interferometric synthesis to collect imagery of dust masses. The latter proved essential to further

[103] See http://www.bisque.com/Products/CCDSoft/.

constraining the orbital dynamics of the Gl 876 system -- not to mention it was an excellent opportunity to exercise very long baseline operations in the radio regime. For this research, two radio studies were performed, at the VLA, and at ATCA. The overarching operations involving these telescopes are noted below, while the character of the research, further discussion of the operations and the results are discussed in Chapter 8.

4.D.1. The Very Large Array (VLA)

Situated 80-km west of Socorro, NM, U.S., the VLA is an unfilled interferometric array of 27 radio antennas in a "Y" configuration as seen in the aerial view, figure 53. This instrument was used to observe the millimeter continuum after conducting the photometric work, in order to search for a mature dust disk about Gl 876.

Fig. 53. Aerial view of VLA spread in approximately mid-way (DnC) configuration. Credit: NRAO

The VLA's individual collectors have 25-m filled apertures, whose baselines are synthetically combined to produce the equivalent of up to a 36-km diameter unfilled aperture, with the sensitivity equal to that of a single 130-m filled aperture. The length of the baselines can be adjusted to change the resolution versus sensitivity as the beam width (BW), which is equivalent to an optical FOV, grows and shrinks in inverse proportion to the extent of the arm length. As in an optical zoom, the most-spread configuration, "A", has a 21-km arm radius which gives the highest resolution in a tight BW, which varies as the wavelength. The configurations move inward through "B" and "C", to the smallest radius of 0.6-km arm length, configuration "D". Configuration "D" provides the widest BW and allows the observer to assess large structure. Hybrid configurations are found between the four major ones. In such a case, a 3-letter designation is used, where the old and pending configuration letters sandwich an "n". A full cycle through the configurations usually takes 16 months. Individual observations may typically be as short as one half hour, to as long as several weeks in duration. Most observations take 3 to 24 hr; a snapshot mode allows very short exposures of less than one minute.

The 7-mm continuum images were processed, calibrated, reduced, and synthesized using what is called "classic" Astronomical Image Processing System (AIPS) software[104]. Further discussion of the VLA is found in Chapter 8.

4.D.2. The Australia Telescope Compact Array (ATCA)

The ATCA at the Paul Wild Narrabri Observatory, is an array of six 22-m antennas used for radio aperture synthesis imagery. It is located 25-km west of Narrabri in New South Wales (approximately 500-km northwest of Sydney) and is run by the Australia Telescope National Facility (ATNF). Five of six telescopes are moved along a 3-km railway while the sixth is situated 3-km beyond this track (the five seen in figure 54). The array is frequently operated together with the 64-m telescope at the Parkes Observatory and a single collector at Mopra (near Coonabarabran), to form a VLBI array. ATCA has begun upgrading to operate at frequencies as high as 100 GHz, which allowed for the millimeter dust search to proceed with this array as well. Five antennas have recently been equipped with 3-mm receivers that extend the coverage to 85-105 GHz. It is these receivers, which were used in the millimeter research.

Fig. 54. 5 of 6 antennas of ATCA. Credit ATNF

As with the VLA, the ATCA 3-mm continuum images were processed, calibrated, reduced and synthesized using, this time, the Multichannel Image Reconstruction, Image Analysis and Display (*MIRIAD*) software.[105] Further discussion of the ATCA (along with the VLA) is found in Chapter 8.

Section 4.E. GEMSS-II Telescope - *ULTRA*

Post-doctoral plans include continued development of GEMSS in Phase II, which is discussed in detail in Chapter 7. To this end, a dedicated instrument has been designed and is now under construction, with first

Fig. 55. Primary foreoptic for *ULTRA*, a WW-II apochromatic triplet lens (pen resting on cell as a size indicator). Photo by author.

[104] See http://www.aips.nrao.edu/.
[105] See http://www.atnf.csiro.au/computing/software/miriad http://astron.berkeley.edu/~wright/miriad/miriad_retrospe

light expected in May 2008. Called Ultra-Light Telescope-Robotic-Apochromatic (*ULTRA*), the fore-optic is an 8" (0.2-m) aperture, f/5.6 focal ratio, Cold War-era reconnaissance aircraft apochromatic triplet, as shown in figure 55. The tube is made of carbon graphite, and is baffled and lined. The mount is a lightweight altitude-azimuth servo-motored "GoTo" single-arm fork. The instrument will be remote-controllable and automated in order to perform search-list operations. The auto-guider will be either the ST-4 or a Meade DSI-Pro mated to a 12-cm F/5 achromat. The collector will the large-format MMV-11000 discussed above, after the author repairs the power supply and re-houses the CCD in a vacuum case, installs an external mechanical shutter and triple-stage thermoelectric cooling. A closed-loop, ethylene-glycol, regulated Cryotiger cooler will also be installed. As a backup, the now-stowed VersArray FPA could be used. However using LN2 significantly hampers any automation process. Meteorological and sky transparency monitors are being built to further automate observations. The instrument will be transportable to find the best conditions for GEMSS photometry.

The components have been secured and are in various stages of fabrication. Planned tests will ascertain whether the MMV-11000 will do photometry best by video means like an advanced TOPhAT, or via traditional time-series imaging photometry. As discussed further in Chapter 7, ULTRA will be dedicated to the GEMSS Phase II targeted M dwarf search in collaboration with other telescopes, such as at Perth, AU (Perth Observatory), Flagstaff, AZ, U.S. (Naval Observatory Flagstaff Station), Townsville, AU (James Cook University), University of California Santa Cruz, CA, U.S. (Lick Observatory and *Transitsearch*), and Cambridge, MA, U.S. (AAVSO). Updates will be found at the GEMSS website. [106]

Additional near infrared (NIR) photometric studies using 1.8 m aperture "Keck Outrigger" telescopes will also be considered in future years (operated in a non-interfereometric mode), if these are installed in the Naval Prototype Optical Interferometer (NPOI) array as a result of their disuse at the Keck Observatory. While a potentially exciting option, with options to team with Lick Observatory spectroscopists, further discussion of the outriggers is in the early planning stage, and beyond the scope of this thesis.

[106] The GEMSS Project is found here: http://gemss.wordpress.com/

Chapter 5: The First Optical Observations -- Initial Flux

The primary science target for this research was Gl 876. The initial 2003 observations of its possible transit egress are noted and discussed here, in the context that are the catalyst for further study of the transits discussed in Chapter 6. These initial observations, which led to the larger campaign, are important in that a transit egress from the limb of Gl 876 may have been detected. This potential detection became the impetus for the large follow-on global study demonstrated the potential for GEMSS. It also was the basis for our consideration of a dust study for a clearer picture of this system (Chapter 8). Find here then, a short review of the bases for the chapters that follow.

Section 5.A. A First System Test -- HD 209458

Based on an assessment of possible test systems to demonstrate TOPhAT's technical capabilities discussed in Chapter 4, HD 209458 was selected as a known transiting planet to observe first. This was to prepare to observe Gl 876, for which transits were suspected but not yet detected at that time. As a 'known entity', HD 209458b's period is relatively frequent at 3.5 days, it was positioned high for low air mass targeting at the time (in Aquarius), and it is sufficiently bright for small aperture collectors. However, the shallowness of its well depth, which is only about 1%, was a major drawback, which if anything tested the limits of TOPhAT. It also lacks the red color and variability expected of M dwarfs, making the assessment of TOPhAT's capabilities in these areas difficult. For a test bed, the "cleanest" of the chosen system is of primary importance; therefore, the well-studied HD 209458b was the best choice.

HD 209458b (α = 22 03 10.77, δ = +18 53 03.5 epoch J2000) is an HJ giant about a solar-like G0V main sequence star (It orbits at a distance of 0.047 AU from its primary, as described in Castellano et al., 2000). During transits, this Jovian planet obscures ~1.7% of the stellar disk for ~2.5 hours, as calculated in Appendix F. Observers can conveniently catch the entire transit, including pre-transit and post-transit flux measurements during every other transit; daytime often obscures one of the transits. The predictions for this test run were based on the work of Laughlin, Castellano et al. (2004), in concert with those of UCO/Lick and Transitsearch.org. All of these were based upon Keck-derived spectroscopic analysis and the subsequent estimation of the observed time of center of transit. For this exoplanet, center of transit time (T_c) were predicted to be at Julian Date (JD) 2451659.93675 +/- 0.00010, with transit and egress at 92.125 minutes before or after; the orbital period is 3.52474 +/- 0.00004 days, with transit ingress and egress at 92.125 minutes before (and after) T_c. (Laughlin, pers. comm., 2003, 2004).

TOPhAT and TIP-TOPhAT were able to capture the transits of HD 209458b. Further analysis of the observations compared to the predictions revealed HD 209458b to have a period of 3.525 ± 3.8×10^{-7}days, a periastron of 2452223.0150 ± 0.00009 days, and an eccentricity of (e) of 0.06 ± 0.08. Argument of perihelion was $\omega = 0.000 \pm 0.10^{o}$, a velocity half-amplitude K = 84.26 m s^{-1} ± 2.2, a minimum planet mass of 0.691 M_{jup} ± 0.05, and a parent-star stellar mass of 1.01 ± 0.066 M_{sun}[107]. It was consistent with an inclination (*i*) of 86.7^{o}± 0.06. These parameters are in keeping with the host star properties effective temperature of ~6000K and stellar radius of $1.15R_{sun}$ (Butler et al., 2006). With a successful test (within 10% of Butler et al., 2006), work with the more elusive red dwarf, Gl 876, was shown to be viable.

Section 5.B. Background on Gl 876 – Selecting it as a Target

The desired characteristics of the primary science candidate were to be a main sequence star brighter than 11th magnitude in V belonging to spectral classes G through M within 50 pc of the Earth. Targets were not to be demonstrably metal-poor because 10% of what are likely to harbor at least one planet. The desire was to include stars with metallicities (Fe/H) > +0.3, and in notable cases, permit inclusion of stars down to a zero metallicity, unless the star already contained RV-detected stars. In addition, targets must lie within a star field appropriate for differential photometry and have suitable, known radial velocities to improve probabilities or to use complimentary validation methods later. Target candidates from Hipparcos and similar surveys (van Leeuwen,et al., 1997; Perryman, M.,et al., 1997; Castellano et al., 2000a) were scrutinized. Castellano and Laughlin (2003) conducted a search of almost 12,700 main sequence stars of spectral types F, G, K and M in the Hipparcos photometry catalog.

Also to arrive at a final candidate, the field of view (FOV) in which it would be found would want to be devoid of photometric competition from nearby variables, such as cataclysmic variables, minor planets, asteroids and Kuiper belt objects (KBOs). Additional preference was given to candidates in the galactic plane and open cluster fields. Position in the sky was constrained due to air mass desired > 1 but in all cases constrained by an altitude > 10° and $\delta <$ -20 (south). Doppler spectroscopy further narrowed the photometric candidates. Stars were eliminated because their spectra contained unusually strong calcium (Ca) emission lines

[107] Regrettably, all HD 209458b transits and some (initial) Gl 876c observations were lost owing to a destroyed computer hard drive the following year. Fortunately the test procedures did demonstrate the viability of TOPhAT, and allowed for the subsequent, preserved data for the primary target, Gl 876 on a different hard drive (during the global campaigns).

indicating photospheric turbulence, double lines indicating an unresolved binary system, or variability indicating rapid rotation; such features could unnecessarily complicate the planned observations. If indeed an RV-detected, planet-bearing star, it was preferred to have a transit probability ($P_{Transit}$) greater than 2.5 %

Candidates were also considered that had large proper motions. Initially, special consideration was given to solar-type stars but this criterion was downgraded because habitable zones (HZs) around solar-like stars, while large, are often beyond the range where photometric detection is possible. Conveniently, the HZs around red dwarfs, while small, are co-situated with the distance from the parent star that makes it easiest to detect exoplanets, both by RV and by photometry. Kastinget al. (1993) define habitably zones (HZs) as those areas in space having planets capable of maintaining liquid water on their surfaces. As discussed in Chapter 2, this definition is the one most commonly accepted for use. Stars were considered that were already known to have dust disks such as T Tauri systems, and especially those with mature, gapped disks. Consideration of dust disks led to the dust search described in Chapter 8. Observations of bright stars are generally photon-limited (Charbonneau, 2003a), and were given preference, although most bright stars have dim planets by comparison. This was mitigated by later reversing the strategy and detecting that were dimmer but within instrumental limitations.

Further constraints included an orbital period of P < ~30 days, necessary so that transit well depth could be repeatedly examined within time constraints. Generally, transits of 51 Pegasi-b type HJs occulting solar-sized stars tend to last about 3 hours, and they produce a 1 – 2% flux degradation of the parent star. Smaller stars, such as red dwarfs, improve this well depth, while they have a lower S/N due to their fainter V magnitudes. Gl 876c falls in this enticing category. To detect such transits, the target must be imaged along with a suitable comparison star of similar brightness and color as discussed in Chapter 3. The observer must keep both well situated on the CCD for at least the duration of the transit, and preferably well beyond that event; the limited on-station time is a weakness of airborne tactical collection. Later portions of the campaign did not have this limitation. Location of a suitable comparison star requires a FOV radius of at least 0.5º. For airborne systems like TOPhAT, careful thought must be given to flight date and time versus orbital periodicity and expected transit. Again this was less of an issue in subsequent endeavors.

Consideration of all these factors resulted in an initial candidate list of five stars: HD 195019, HD 130322, HD 74156, HD 80606 and Gl 876. Gl 876 became the final choice, which was incidentally the only M star in this early look. HD 195019 is a G3IV-V with HJ giant at 20 pc and V=6.91; HD 130322 is a K0V with HJ giant at 28 pc and V=8.04; HD 74156 is a G0 with

two eccentric giants at 65 pc and V=7.61; and HD 80606 is a G5 with (a very) eccentric giant at 58 pc and V=9.06. All are well situated for northern hemispheric collection. The HD 80606 system had a rather low transit probability. However, due to its large eccentricity of e = 0.927 ± 0.012 and long-period orbit P = 111.78 ± 0.21 days [108], (Butler et al. 2005), the transit predictions are well constrained, making HD 80606 a useful and interesting quaternary choice. In fact the author has observed HD 80606 at the November 2007 periastron passage (seeking exo-Aurorae) using the Very Large Array, in concert with a Spitzer Space Telescope team observing in the IR. Those results will prove to be an appropriate postlude to the work here.

Conversely, HD 38529b is well-situated, with a high transit probability, but because the host star has a radius of 2.58 $R_\odot$ the transit depth is a mere 0.13%, making it unsavory for collection here. Other possibilities (HD 767000, HD 162020, HD 108147, and HD 13445) were eliminated because of their southerly declinations. Of these candidates, Gl 876 turned out to be the most interesting, needed immediate understanding of its inclination, harbored multiple planets, was nearby, and had the best flux dip, despite its dimness.

Choosing Gl 876 still comes at a certain price. Not only is it dim for modest apertures, most importantly it is considered a variable (Rivera et al., 2005). If the variable signal could compete with the dip that could be attributed to a transit, the star would have to be eliminated. Problematically, very little is known about the photometric variability of Gl 876 on rotational and magnetic cycle timescales. Fortunately, variability on time scales of a few hours, similar to those of a transit, are unlikely to conflict as the long-period signatures have little relative amplitude variation. Weis (1994) suspected a period of 2.9 years in the flux curve based on a 2 – 3% variability detected in 38 measurements at Kitt Peak National Observatory over 11 yr. Based on his findings, Kazarovets & Samus (1997) assigned Gl 876 the variable star name IL Aquarii in the 73rd *Name List of Variable Stars*. Hipparcos did not detect photometric variability made 67 brightness measurements over the course of its 3 year mission. The Hipparcos are consistent with the star's low level of chromospheric and coronal activity (Delfosse et al. 1998). Based on these assessments, Gl 876 remained the most suitable choice.

While a long-coverage observing was planned and executed as discussed in Chapter 6, Laughlin et al. (2005), added 65 additional radial velocities to the prediction fit (Laughlin, Pers. Comm., 2004). This refined the three-body solution to the orbital dynamics. These additional constraints led to more precise prediction models, that when applied in retrospect produced a central transit time for planet "c" for Oct. 2003 of JD 2452940.31 ± 0.22, with a corresponding egress time of

[108] See http://exoplanet.eu/star.php?st=HD+80606 for the current parameters of this system.

JD 2452940.36 ± 0.22. This window is consistent to within 1 σ of the author's 2003 flux-variant observations, discussed next.

Section 5C: Initial Collection Detail – Gl 876

The Gl 876 light curve obtained in 2003 (seen in figure 56 and in Appendix E) -- and the instrumentation -- were scrutinized to ensure the flux variation was not a false positive. The curve is consistent with a transit egress and is the basis for the follow-up observations and reported work in Chapter 6 and Appendix C. Time-series differential photometry of Gl 876 was taken from 2003 Oct. 27.9583 to 2003 Oct. 28.0368, which revealed a monotonic flux increase of 0.16 ± 0.04 mag from 2003 Oct. 27.9583 to 2003 Oct. 27.9972.

Owing to the clean signal (which matched the characteristics of an egress and occurred within 1 σ of RV-based predictions), the time, duration, and depth of this event appeared to be consistent with a transit egress of planet Gl 876c. This possible detection gave impetus to further investigations of this multi-planet system. The co-planar, edge-on, three-body dynamical model for the Gl 876 system predicted a central transit epoch for planet "c" at 2003 Oct. 27.81 ± 0.22 d with a central transit duration (t_d) of 0.10 ± 0.02 d, assuming a stellar radius of $0.3R_{\odot}$. (Laughlin, personal communication).

These compelling observations were collected through a Cousins V filter at the primary focus of ORCA with TIP-TOPhAT, positioned 16 km north of Meridian Mississippi, USA (longitude 05h 54m W, latitude 32° 29' N, GPS position) during clear weather. The air mass for Gl 876 ranged from sec(z) = 2.7 to sec(z) = 1.8. Observations were obtained in clear weather.

This differential photometry time series was based on inter-comparison with these check stars[109]:

Check Star	A	Δ	equinox	Mag (V)	Spectral Type
HD 216387	22h 52m 40s.45	-14° 25' 28".2	2000.0	V= 10.30	F5 IV/V
HD 216442	22h 53m 04s.27	-14° 02' 55".6	2000.0	V= 10.24	G8 V
BD-14 6363	22h 53m 26s.13	-14° 00' 46".3	2000.0	V= 9.8	GV
HD 216310	22h 52m05s.74	-14° 25'55".43	2000.0	V= 9.74	G3 V

[109] As with the HD209458b data, some initial Gl 876 research was since lost during a hard drive failure. Fortunately the data represented herein had been saved separately. See Appendix E for a graphical depiction of the intercomparison stars' effects.

A representation of the transit egress can be seen to the right. Details are found in Appendix E. The signal did not exhibit flare or star spot characteristics, and even at the limit of the error bars, the signal provided a variation consistent with a limb passage. The observation gave strong cause for follow-up observations.

Section 5.D. A Global Transit Follow-up

The flux variation required follow-up and verification. Because transits only last a fraction of a day (~1 hour for an M dwarf), Gl 876 would need to be monitored continuously, at least once every few hours to achieve a notional 3 σ coverage, especially for confirmation detections. Continuous monitoring required a FOV available for 3 σ around prediction windows for over half a year when the constellation Aquarius was up. Achieving an incomplete but long-coverage season would require global observation in the case of Gl 876. As noted elsewhere, the Rossiter-McLaughlin (R-M) effect was used to assess RV observations to flag or constrain possible transits (Marcy & Bundy 2000; Queloz et al. 2000; Rossiter, 1924; Mclaughlin, 1924). Chapter 6 and Appendix C provide details of this R-M RV assessment.

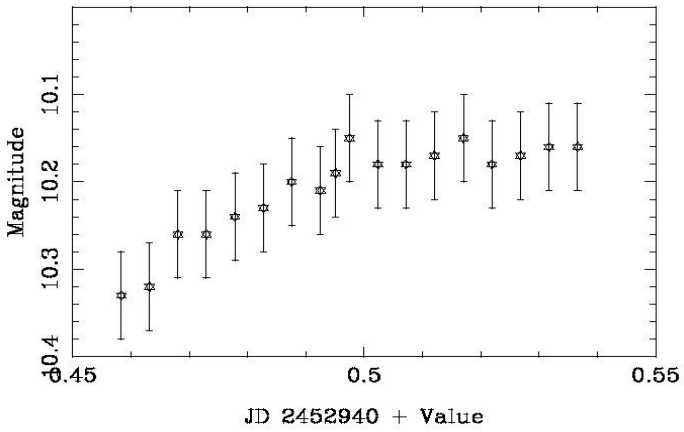

Fig. 56 .Potential 2003 egress flux; see Appendix E for Details. In this graph on the X-axis, the abscissa values 0.45 through 0.55 are combined with a value of 2452940 to give the Julian Date (JD). Variation was a mean V of +/- 0.04 to 1σ (as detailed in a similar graphic in apprendix E). Above, error bars are shown to a broader 2 σ, or V = +/- 0.08. See Appendix E for more detail and a depiction of the check stars.

The global campaign was arranged to begin in 2004 with Australia, which was the first location able to observe Aquarius in parallel with the global observation program. The first window occurred on 2004 June 24, 2004 and several Australian photometrists participated. Unfortunately the prediction window centered on 20 July was obscured by weather. For the next prediction window, the effort was expanded to include Japanese observers. By August, observers from the AAVSO joined the campaign. With the “b” planet in its larger orbit of 60.2 days and resonating with a period of twice its inner sibling “c”, it was added to the searches bimonthly at this point. Concentrated efforts continued monthly around 3 σ prediction windows. Assessment of the photometry obtained during the August 23rd opportunity for planet "c" indicated that no such transit occurred in that window. The September 2004 opportunities were

missed due to bad weather. The worldwide observing run during the Oct. 21, 2004 planet "b" opportunity was the largest effort and afforded a complete 3σ prediction coverage. The results indicated that the outer planet was not then transiting.

Although this stint produced no transits, it demonstrated that large, distributed detection networks were possible using modest apertures could produce valuable science. The results further constrained the system dynamics, and were reported in the *Astrophysical Journal*. That material is presented next in Chapter 6.

Chapter 6: Gl 876 and the Global, Distributed Transit Search (*ApJ, 2006*)

With the knowledge provided by the radial velocity studies, the key to understanding Gl 876 as a complete, multi-planet, dynamical system centered around knowing its inclination. This could be found by observing a transit of one of its planets. If this M dwarf were to be well understood, it would help to understand unusual dynamics found about a red dwarf, and add to the scant knowledge of M stars. Prior to the photometry performed here, studies by Benedict et al. (2002) using the Hubble Space Telescope (HST) Fine Guidance Sensor (FGS) revealed a symmetric astrometric signature that asserted system was inclined to $84^{o} \pm 6$, and ripe for a yet-observed transit. This declaration was the impetus to detect such a transit, and began the study which culminated in what follows. It may at first seem of less importance to have obtained a null result subsequent to Benedict. As will be revealed, that is what was obtained here from the eventual plethora of optical observation.

But nothing could be further from the truth. The study herein provided a surprise result in that an edge-on inclination was shown *not* to occur. While an initial transit egress seems to have been detected for 2003, the non-detections in the follow-ups along with the use of the radial velocity Rossiter-McLaughlin (R-M) effect[110] show that since 2004 this system cannot be inclined edge-on to the Earth (Ohta, Taruya & Suto, 2005). The lack of transit effects on the RV data was further scrutinized, and the variances owed to the R-M effect showed the system to be inclined to an actual $i = 50^{o}$. What this does to constrain the orbital dynamics is profound, in that RV-derived masses (limited to understanding them by sin (i) with RV alone) can now be solved. For the 2005 RV-derived planetary masses in Appendix D, a factor of 0.766 can further constrain the masses to 1.482 M_{jup} and 0.474 M_{jup} for the outer Jovian planets "b" and "c", respectively. For planet "d" (Rivera et al., 2005), the mass is derived to be 0.0142 M_{Jup}, or 4.52 Earth masses, which makes this terrestrial planet the smallest known to date. By way of comparison, GJ 581c has an unknown inclination but an RV-derived mass of 0.158 M_{Jup} (sin i), or 5.6 Earth masses (Udry et al. (2007). Just detected, GJ 581 was

[110] The parent star rotates during a transit, and the planet will occult a small portion of the red and blue shifts of the star's spectral lines while it traverses the face of the star. When crossing the blue shifted quadrant, some blue signal is lost, and vice versa. This shows up in an RV curve as a canting of the classic sinus shape, and can be modeled.

also the system the author recommended in the Shankland et al. (2006) as an ideal target for studies seeking Earth-massed planets.

The efforts to identify the inclination via transit were extensive. Attempts were made to observe transits for both Gl 876's planets "b" and "c" during prediction opportunities throughout 2004 and early 2005. For the Gl 876 campaign, the majority of the earlier sessions were clouded out; however working results were obtained by 2004 October. The 2004 global team found no transits in these efforts, and when combined with RV studies discussed shortly, transits from 2004-2005 can be ruled out. Archival reviews for transits are less clear. The published *Astrophysical Journal* paper reprinted here also indicates the expanse of the team created as a result of this research, which itself advances the understanding of effective observation with large, distributed photometric networks.

Section 6.A. Transit campaigns: TransitSearch and AAVSO

The notion of a large optical search campaign was first thought to be viable in the early nineties (Kjeldsen & Frandsen, 1992; Walker, 1993). In the campaign specifically devised to perform transit photometry for Gl 876, it was certainly proven as a viable concept, with a number of challenges to overcome along the way. Distributed photometry requires protracted oversight of the distribution of operators and reassembly of sometimes-inhomogeneous data. But distributed networks have shown their great merit in the information technology (IT) community, and the paradigm is easily applied to this research. Of course, the effort described in the Transitsearch collaboration as described in Seagroves et al. (2003) and Laughlin & Chambers (2001) was critical to understanding a clear path to achievable results. The published paper here underscores that role. Realizing the power to leverage existing capabilities from a distance becomes a sure means to getting programs accomplished. AAVSO was another lever in the research, whose role in the observations is also underscored. In both cases the observing infrastructure eventually became the equivalent of a remote-access, automated observing instrument, not unlike the way most major interferometric radio telescopes currently operate.

Section 6.B. An Archival Check: The All Sky Automated Survey- ASAS

Princeton University conducts an All Sky Automated Survey, and has archival data for its third iteration, ASAS-3.[111] A review of this archive produced some potentially interesting overlap with predictions, and was investigated while the Transitsearch photometry campaigns continued. ASAS has the goal of providing multi-epoch photometric coverage of the whole sky using a homogeneous network of five small telescopes attached to CCD cameras, as further described in Pojmanski (2002). The third version of this survey covers the southern hemisphere. It is also in the proper dynamic brightness range, and therefore would be suitable to the GEMSS team's use (this portion led by D. Blank of James Cook University). It turns out that Gl 876 was observed 230 times during the ASAS-3 survey between 2000 November 22 and 2004 September 6. In one case a then-predicted transit egress had been modeled to occur 0.09589 days before an ASAS exposure on 2002 October 21.11088. In this data a flux drop of V = 0.1045 ± 0.032 magnitude was detected. Additional ASAS-3 data from 2002 December 21.05827 showed no other notable variation. See Appendix E for relevant ASAS-3 data. Unfortunately the ASAS-3 data was insufficiently dense to eliminate other explanations for the variability or to generate a transit-like curve. An average of the data increases the uncertainty to the point that the uncertainty exceeds the transit depth, or falls beneath the noise floor. While provocative and consistent with the 2004 edge-on dynamical model, the data would have had more fidelity to stand as a transit detection and not a another event.

Section 6.C. Oklo's Systemic - Understanding RVs and R-M Effects

As part of the effort to understand both the Rossiter-Mclaughlin and general RV effects on Gl 876 during notional transits, a collaboration with the *Systemic* team was developed[112]. Systemic represents another large-scale distributed effort to characterize exoplanets, of which modeling Gl 876 was a part. This effort leverages the ability to model exoplanet RV curves across a spectrum of on-line users who take the team's Systemic software and employ it to fit a number of both theoretical and actual RV curves. As an example of distributed computing, this particular effort requires dynamic interaction from the user through variation of any number of the system ephemerides.

---

[111] See http://archive.princeton.edu/~asas/asas.html

[112] see http://oklo.org/?page_id=33. The team members are identified there, and include G. Laughlin (UCSC), S. Meschiari (UCSC), E. Rivera (UCSC), A. Price (Caltech), and the author.

The name *Systemic* was developed for this program because the algorithm is a "system integrator" console. The larger intent of the Oklo team is to seek a better understanding of the statistical distribution of planetary system initial conditions throughout the Galaxy. The collaboration makes potentially enlightened insights when analyses offer surprising results. The ultimate goal is to compare the synthetic planets to the growing collection of real ones, and compare the real dynamics to the manufactured ones to see that they are fully internally consistent. After they have been characterized via synthetic radial velocity observations, the planets orbiting the systemic stars will be the focus of further observational models and, eventually, synthetic, virtual *exploration*. Humanity may not be destined for near-term interstellar travel, but Moore's law should provide sufficient computing power in 4 decades to make synthetic exploration a useful tool for immersive analyses. The Oklo *Systemic* research is elaborated upon in Shankland & Laughlin (2006).

As the basis on which to build *Systemic* (and its precursor, *Systemic, Jr.),* the Oklo team built the reduction scheme upon a catalog of 100,000 stars, with both real and synthetic orbits about 970 of these stars. The planetary systems were designed to be fully internally consistent as noted, and running the software helps to empirically validate this assertion. The author participated at length in the Beta testing of ported JAVA routines, testing of the fit routines against synthetic data for operability, and conducted extensive RV data set entry (the data are divided into 450 real and 520 simulated stellar data sets, with numerous entries per set). These are bootstrapped through a Monte Carlo routine to produce results which can be manipulated for real-time curve fitting. In *Systemic*, the datasets are integrated on each system for 10^6 yr to sort out dynamical instabilities (using inelastic collisions). As with the real datasets, the synthetic datasets use realistic cadences, S/N, Earth location, and air mass to ensure their results are also realistic. During 2005-2006, the author and A. Wolfe tested and ported the *Systemic* Java applet code between PC, Apple OSX, and Linux operating systems, identifying porting and operating bugs in the data fitting and reduction evaluation of a number of simulated and real-system runs, particularly for the Gl 876 RV data[113]. With G. Laughlin, the author participated in start-up site maintenance, web page drafting, and pedagogical dialogue

[113] See http://oklo.org/?page_id=9 for specific Gl 876 tutorials developed.

with public participants as to system operation, data analyses, and progress in various exoplanet programs.

The OKLO team's *Systemic* is a Java tool which provides a 'tactile' means to introduce the user to what reductions do in the fitting of a possible Keplerian (or other) orbital curve to a real (or synthetic) radial velocity dataset, replete with imperfections and outliers. For the Oklo team it gives "goodness of fit" and "long term stability" feedback. The statistical tools, from simple application of Kepler's and Newton's laws, Monte Carlo and bootstrapping, to use of periodograms, Levenberg-Marquardt and classical LSQ fitting, to chi^2 (χ^2) and Runge-Kutta methods) are used in *Systemic*. The concepts are discussed in some detail in Appendix C. There, the analyses are discussed as to the effect of the Rossiter-McLaughlin effect upon the RV curves during transits. The *Systemic* console extends such specific analysis to a more general understanding of how radial velocity curves behave during their fitting to the data. The applet allows graphical and numerical results to be displayed near real-time, as though the user were exercising his / her own Monte Carlo bootstrapped 'Do-loop', assaying the result at each adjustment for fit. The reader is encourage to either download, or access and run the applet on-line to feel the qualitative feedback the console provides.[114]

The fit methods used in *Systemic* are how Gl 876 was assessed as shown later in this chapter and in Appendix C, so that transit potential was understood[115]. The goal of *Systemic* has been to improve statistical understanding of the distribution of current and initial conditions for exoplanets in the Galaxy, and to clarify obtuse or hidden dynamical relationships to the team (Shankland & Laughlin, 2006). The "Console" applet allows the user to select either synthetic or real RV datasets from a dropdown menu. From there, the applet displays RV points and an initial RV curve. The orbital dynamics are then optimized for a best fit of the curve, using the various sliders and/or subroutine buttons.[116] While one may reduce RVs in the approximate order described below, a set procedure is not fully defined, which allows the Systemic user to adjust any multiple of variables or minima to find the best global solution.

---

[114] Download at http://oklo.org/?page_id=86, or try the online console at http://www.oklo.org/SystemicBeta/SystemicBeta.html. Note the online version is sometimes temperamental for some Windows OS-based computers. In this case the download is suggested.
[115] For a treatise on the many numerical methods employed in Systemic, read *Numerical Recipes: The Art of Scientific Computing* (Press et al., 1989, 1992, 2007), which is salient.
[116] These orbital parameters and related fundamentals are defined in Appendix D.

The planetary mass slider would likely be first used when fitting RV data, in order to adjust the amplitude of the radial velocity signal so that it approximates the data point amplitude. The fit can also be adjusted for mean anomaly, which is the position of the planet in its orbit. This laterally shifts the curve to overlay the data points as the user sees best (since most RV data sets would not normally start at 0 m s^{-1}). To be more precise, one can zoom into regions of the curve to determine line overlays visually. A zoom-able window is also offered to provide an overhead depiction of the orbit being "built". Eccentricity of the orbit is also adjusted with an assigned slider, which might help to visually further align the data with the waveform. The closest approach of this orbit, the periastron, may then be chosen as an angle, the longitude of periastron, and is shown as a dotted line in the overhead depiction. As with the mean anomaly, the data must also be zeroized vertically, particularly to match disparate data sets. This is done using the 'stellar velocity' slider.

To assess how well the data is matching the offered curve, the root-mean-square (RMS) of the fit is taken, as well as the reduced Chi-square (χ^2), which weights data with smaller error more strongly, with the ideal in Systemic being $\chi^2 = 1$. The error itself is measured at the telescope and entered with the data. Separately, Systemic can account for stellar jitter (which is owed to non-zero photospheric turbulence). Like RV measurements, jitter is measured in m s^{-1}.

While fits may be done manually, there are multiple levels of automation in Systemic. For most measurements, clicking on the right-hand radio button by each slider in the applet, repeatedly if desired. This causes a local minimization of that parameter. Fits can be refined with "Polish", which smoothes the fit by multi-parameterization. Polish invokes the Levenberg-Marquardt (L-M) minimization, which seeks a global minimum for all clicked parameters. If the fit still falls short, one may look for residual 'spikes', an indication that other planets co-exist in the data. The user may select 'periodogram' from the drop-down menu, which runs a Fourier transform to produce the graphical Lomb-Scargle periodogram. The periodogram's stronger peaks occur at residual periods for likely additional planets. Subsequent planets might then be added along the lower left side, near the suggested periods. The above reduction procedure might then be repeated again to improve the fit. If the system appears to contain multiple planets, the

user might also try a periodogram of the residuals (a transform of the transform) to seek more planets.

If the system exhibits non-Keplerian motions such as some resonance (Gl 876 is a classic example[117]), further progress may be difficult, since *Systemic* will have processed the RV data simply to a local minimal. *Systemic* starts as though these were simple Keplerian-Newtonian orbits. Alternative reduction may be in order by switching the "Integrate" window to Runge-Kutta (where gravitational interactions are taken into account) or Hermite (which interpolates the derivatives of the data points as well as the points themselves[118]). Non-Keplerian integration however is computer-intensive and quite slow.

Other features include the ability to manipulate synthetic data, and 'create' complicated RV curves, which offers a better understanding of possible orbital mechanics. Bootstrapping unknown parameters to tighten error bars is now possible, as is period folding (where multiple planets show up as a smear), and stability testing can be done. Options also provide a transit calculator, which takes known transiting planets and significantly constrains the dynamics offered by the RVs. For the audiophile, the RV curve can be converted to an acoustic waveform and played on the computer to detect harmonics.

Systemic allows to user a true qualitative 'feel' for the effects orbital dynamics have upon their RV curves. This qualitative feel helps not only to educate the public (who may participate in *Systemic* reductions), it allows graphical manipulation of real data for detections.

For the Gl 876, the author employed the dataset to characterize the dynamics of its 3 planets (Marcy et al., 2001) with E. Rivera, and then did so independently as a check. This was the first multi-planet system to be used in *Systemic* to validate internal consistencies in the models with real observations. In *Systemic*, the periodogram of the

---

[117] An example of an RV reduction of Gl 876 using Systemic is found at: http://oklo.org/?p=37#more-37. The tutorial is a result of the team's work along with their participation in the paper in the next section.

[118] The Hermite method is used in numerical analysis to interpolate, and to consider given derivatives at data points to the original data points. Such an interpolation produces a polynomial ≤ the combination of the point(s) and the derivative(s) − 1.

data showed power peaks at periods aligned with the three planets.[6] An online example of the Console being used to reduce Gl 876 data is shown in figure 57.

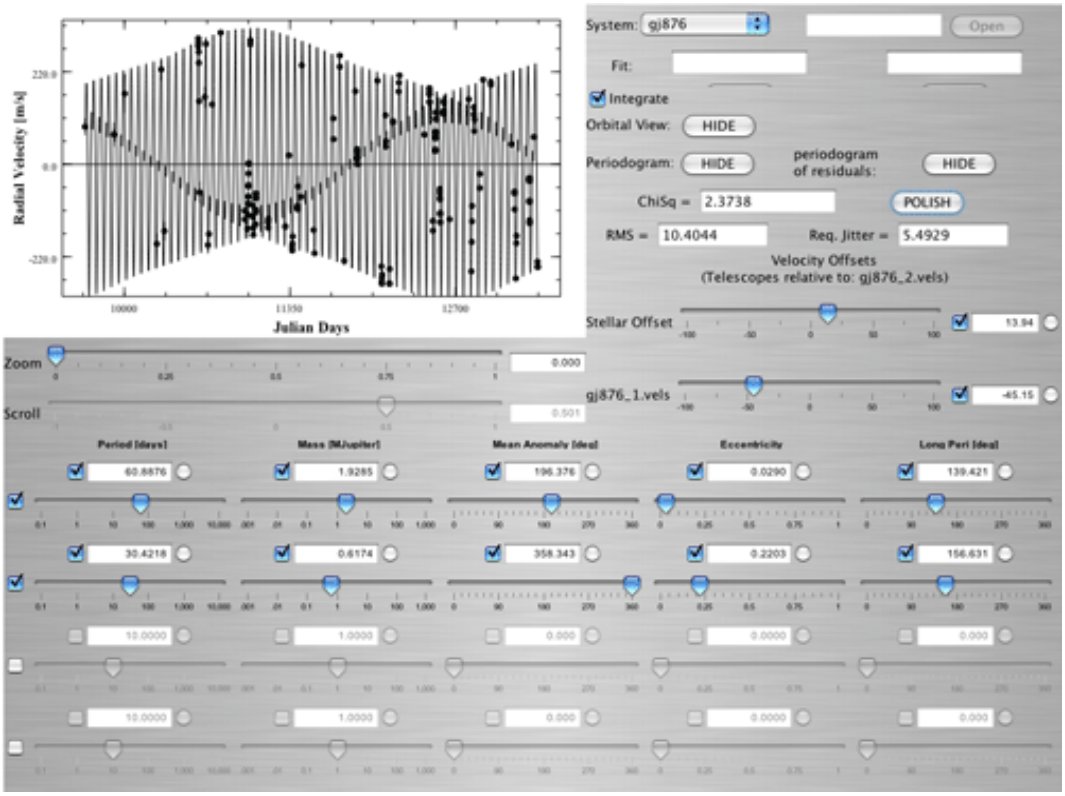

Fig. 57. Systemic Console, 2006, during Gl 876 reductions, image credit: G. Laughlin

As a comparison to 'real' results, note that after reduction without L-M polish, the Gl 876 periodogram first peaks at 60.961 days, and the periodogram of the residuals peaks at 30.247 days. Minimizing for the greater eccentricity of the second planet ("c"), and another similar fit, an integration and a polish, the periodogram of residuals revealed the third planet ("d") at 1.94 days. This occurred with good initial conditions estimated and entered. The results gave a χ^2 of 1.38, with jitter at 1.79 – 2.86 m s^{-1}. Further dynamics are studied next, and in Appendix C.

The Astrophysical Journal, 653:700–707, 2006 December 10
© 2006. The American Astronomical Society. All rights reserved. Printed in U.S.A.

ON THE SEARCH FOR TRANSITS OF THE PLANETS ORBITING GLIESE 876

P. D. Shankland,[1,2] E. J. Rivera,[3] G. Laughlin,[3] D. L. Blank,[1] A. Price,[4] B. Gary,[4] R. Bissinger,[4] F. Ringwald,[5] G. White,[1] G. W. Henry,[6] P. McGee,[7] A. S. Wolf,[3] B. Carter,[8] S. Lee,[9] J. Biggs,[10] B. Monard,[11] and M. C. B. Ashley[12]

Received 2006 May 7; accepted 2006 August 21

ABSTRACT

We report the results of a globally coordinated photometric campaign to search for transits by the $P \sim 30$ day and $P \sim 60$ day outer planets of the three-planet system orbiting the nearby M dwarf Gl 876. These two planets experience strong mutual perturbations, which necessitate the use of a dynamical (four-body) model to compute transit ephemerides for the system. Our photometric data have been collected from published archival sources, as well as from our photometric campaigns that were targeted to specific transit predictions. Our analysis indicates that transits by planet c ($P \sim 30$ days) do not currently occur, in concordance with the best-fit $i = 50^\circ$ coplanar configuration obtained by dynamical fits to the most recent radial velocity data for the system. Transits by planet b ($P \sim 60$ day) are not entirely ruled out by our observations, but our data indicate that it is very unlikely that they occur. Our experience with the Gl 876 system suggests that a distributed ground-based network of small telescopes can be used to search for transits of very low mass M stars by terrestrial-sized planets.

Subject headings: planetary systems — planets and satellites: general — stars: individual (Gliese 876)

1. INTRODUCTION

The Gl 876 planetary system ranks with the most remarkable discoveries that have emerged from the first decade of extrasolar planet detections. As described by Rivera et al. (2005), Laughlin et al. (2005), Butler et al. (2001), Marcy et al. (1998, 2001), and Delfosse et al. (1998), there are a number of reasons why the Gl 876 planets are extraordinary. Planet d with its 1.974 day orbit and $M \sin(i) = 5.9\ M_\oplus$, is the lowest mass exoplanet known to orbit a nearby main-sequence star (Rivera et al. 2005). Planets c and b are the only Jovian-mass companions known to orbit an M dwarf, and their clear participation in 2:1 mean-motion resonance gives important dynamical clues to the formation and evolution of the system (e.g., Lee & Peale 2002). Furthermore, the Gl 876 planets are the closest exoplanets that have been reliably characterized. Their radial velocity amplitudes induce an overall signal-to-noise ratio of nearly 100, and they have been observed for well over a decade.

The detection of Gl 876d by Rivera et al. (2005) underscored the rapid development of the Doppler technique. The detection of planets having only a few Earth masses is the culmination of advances described by Butler et al. (1996), Marcy & Butler (1998), Marcy et al. (2000, 2005), and Lovis et al. (2006). Nevertheless, while radial velocity precision has improved to better than 1 m s^{-1}, Keplerian orbital fits to Doppler velocities give estimates of $M_{\rm pl}\sin(i)$ rather than $M_{\rm pl}$. In order to ascertain the true mass of a planet, one must obtain an independent measure of the orbital inclination i, which is most easily measured when the planet is observed to transit across the face of the parent star.

The now celebrated companion to HD 209458 provided the first example of a transiting extrasolar planet, and this body has generated an incredible variety of observational and theoretical investigations. HD 209458b was initially detected with the radial velocity method, and was then discovered to transit on the basis of follow-up photometric observations at the predicted transit times (Henry et al. 1999, 2000; Charbonneau et al. 2000). HD 209458b's well-sampled light curve, when combined with high-precision radial velocity data, has permitted precise measurements of the planet's basic attributes (e.g., Mazeh et al. 2000; Brown et al. 2001; Laughlin et al. 2005; Winn & Holman 2005).

To date, nine additional planets have been found to transit their parent stars, and the varied uses to which these transits have been put are described in the review article by Charbonneau et al. (2006). Our goal in this paper is to ascertain whether the two outer planets orbiting Gl 876 (IL Aqr, GJ 876, HIP 113020) can similarly be observed in transit. A positive detection would represent a further major improvement in our understanding both of this specific system and of planetary properties in general.

Rivera et al. (2005) carried out a photometric search for transits by planet d ($P \sim 1.974$ day), and showed that such transits do not occur. To date, photometric searches for transits by planet c ($P \sim 30$ day) and b ($P \sim 60$ day) have not been reported. Although the a priori geometric transit probabilities for Gl 876c and b are only $P_{\rm tr} = 1.4\%$ and $P_{\rm tr} = 0.9\%$, respectively, the expected photometric transit depths are greater than 10%. Librational motions arising from the resonance between the two outer planets lead to predicted transit epochs for the outer planets that are not

[1] Centre for Astronomy, School of Mathematical and Physical Sciences, James Cook University, Townsville QLD 4811, Australia.
[2] Current address: US Naval Observatory, 3450 Massachusetts Avenue NW, Washington, DC 20392-5420; paul.shankland@usno.navy.mil.
[3] University of California/Lick Observatory, University of California at Santa Cruz, Santa Cruz, CA 95064.
[4] American Association of Variable Star Observers, Clinton B. Ford Astronomical Data and Research Center, 25 Birch St., Cambridge, MA 02138.
[5] Department of Physics, California State University, Fresno, 2345 East San Ramon Avenue, M/S MH37, Fresno, CA 93740.
[6] Center of Excellence in Information Systems, Tennessee State University, 3500 John A. Merritt Boulevard, Box 9501, Nashville, TN 37209.
[7] School of Chemistry and Physics, University of Adelaide, Adelaide SA 5005, Australia.
[8] Centre for Astronomy, Solar Radiation and Climate Physics, University of Southern Queensland, Towoomba 4350, Australia.
[9] Anglo-Australian Observatory, 167 Vimiera Road, Eastwood NSW 2122, Australia.
[10] Perth Observatory, Walnut Road, Bickley WA 6076, Australia.
[11] Bronberg Observatory, Centurion 0157, Pretoria, South Africa.
[12] School of Physics, University of New South Wales, Sydney, NSW 2052, Australia.

TABLE 1
Coplanar Three-Planet $i = 90^\circ$ Jacobi Parameters of the Gl 876 System

Parameter	Planet d	Planet c	Planet b
m^a	$5.89 \pm 0.54\ M_\oplus$	$0.619 \pm 0.005 M_{\rm Jup}$	$1.935 \pm 0.007 M_{\rm Jup}$
P (days)	1.93776 ± 0.00007	30.340 ± 0.013	60.940 ± 0.013
K (m s^{-1})	6.46 ± 0.59	88.36 ± 0.72	212.60 ± 0.76
a^a (AU)	0.0208067 ± 0.0000005	0.13030 ± 0.00004	0.20783 ± 0.00003
e	0 (fixed)	0.2243 ± 0.0013	0.0249 ± 0.0026
ω (deg)	0 (fixed)	198.3 ± 0.9	175.7 ± 6.0
M (deg)	309.5 ± 5.1	308.5 ± 1.4	175.5 ± 6.0
transit epoch	JD 2,452,490.756 $\pm$ 0.027	JD 2,452,517.633 $\pm$ 0.051	...

[a] Quoted uncertainties in planetary masses and semimajor axes *do not* incorporate the uncertainty in the mass of the star.

spaced evenly in time. (The resonant structure of the system is discussed further in Laughlin & Chambers 2001; Rivera & Lissauer 2001; Kley 2003; and Beaugé et al. 2005).

Benedict et al. (2002) used *Hubble Space Telescope (HST)* astrometry to derive an orbital inclination for Gl 876b of $i = 84^\circ \pm 6^\circ$. Their result thus suggests that planet b has a mass equal or close to the radial velocity (RV)-determined value of $M \sin(i) = 1.89 M_{\rm Jup}$, and that the system is within 1 σ of being viewed edge-on. The implication of the Benedict et al. (2002) measurement is that occurrence of transits is much more likely than the a priori geometric probability would suggest. The Benedict et al. (2002) result is in conflict, however, with the dynamical models of the system presented by Rivera et al. (2005), who find a best fit to the radial velocity data when the system (assumed coplanar) is inclined by $i \sim 50^\circ \pm 3^\circ$ with respect to the plane of the sky. Therefore, if transits are detected, then the Benedict et al. (2002) results will be confirmed at the expense of the conclusions of Rivera et al. (2005).

Gl 876b and Gl 876c are members of an as yet unobserved class of giant planets with intermediate surface temperatures. The expected effective temperatures of $T_{\rm eff,b} = 160$ K and $T_{\rm eff,c} = 200$ K of the planets are much lower than the value $T_{\rm eff} \sim 1350$ K measured with *Spitzer* for HD 209458b (Charbonneau et al. 2005), but still considerably higher than the $T_{\rm eff} \sim 135$ K measured for Jupiter. Determination of their physical properties would thus provide a useful link between Jupiter and Saturn on the one hand, and objects such as HD 209458b on the other. Accurate measurement of their radii would also give clues to their interior structure (see Charbonneau et al. 2006).

Finally, the Gl 876 system with its strongly gravitationally interacting planets and large planet-to-star radius ratios, has the potential to display an extraordinarily informative set of transit light curves. Our model light curves here show what one can expect when interacting transiting systems are discovered, for example, with ongoing radial velocity surveys or with space-based missions such as *Kepler* (Borucki et al. 2003) or *COROT* (Baglin 2003), and allow for a more complete understanding of the multiplanet dynamics.

The plan of this paper is as follows. In § 2 we describe our dynamical model of the system, and illustrate some of the photometric properties that the in-transit light curves would be expected to display. In § 3 we describe an evaluation of the Doppler radial velocity measurements that have been taken during predicted transit intervals. In § 4 we evaluate a range of archival and newly obtained photometric data sets for evidence of transits. In § 5 we discuss our results, as well as the current status and outlook for the ongoing Transitsearch collaboration and conclude in § 6.

2. THE DYNAMICAL MODEL

Gl 876 (M4V) is the 40th nearest star to Earth, with a *Hipparcos*-determined distance of 4.69 pc (Perryman et al. 1997); Tycho-II and UCAC positions validate this determination. As discussed in Laughlin et al. (2005), current estimates of its mass and radius stand at $M_\star = 0.32\ M_\odot$ and $R_\star = 0.3\ R_\odot$. We adopt these values as fixed in this paper. To date, 155 Doppler velocities measured at the Keck telescope and 16 velocities measured at the Lick telescope have been published for the Gl 876 system (Marcy et al. 2001; Rivera et al. 2005). The two planets induce a total velocity half-amplitude of the star of nearly 0.25 km s^{-1}. Furthermore, as discussed in Rivera et al. (2005), the system displays a very low level of stellar radial velocity "jitter," which further aids in obtaining a detailed characterization of the orbits. The system has now been observed for more than 80 orbital periods of the middle planet, c. This extensive time baseline allows for a much more detailed study of planet-planet interactions than can be obtained with the other exoplanetary systems known to be in 2:1 resonance, a list that now includes HD 82943 (Mayor et al. 2004; Lee et al. 2006), HD 128311 (Vogt et al. 2005), and HD 73526 (Tinney et al. 2006). These three systems all have inner planet periods on the order of 10 times longer than Gl 876c. Our baseline coplanar $i = 90^\circ$ orbital model was obtained by Rivera et al. (2005) from a dynamical fit to the Keck radial velocity data. For reference, the parameters of this model are reproduced in Table 1.[13] Additional fits with $i < 90^\circ$ were also obtained to the Keck data using the algorithm described by Rivera et al. (2005). As with the $i = 90^\circ$ baseline model, the system is assumed to contain three planets, all orbiting the star in the same plane. We varied the inclination of the orbital plane to the plane of the sky from $i = 90^\circ$ to $89^\circ.0$ in decrements of $0^\circ.1$, and fitted for each of the 13 + 1 remaining parameters. Then N-body integrations of the fit generate a sequence of transit predictions for the outer two planets. Uncertainties in the predicted transit midpoints were generated with the bootstrap Monte Carlo technique described by Rivera et al. (2005). For both outer planets, the uncertainty in the transit midpoint times was found to vary from $\sim$1 to a few hours. The variation in uncertainty from transit to transit is plotted in Figure 1. The predicted transit midpoints are best constrained during the epoch spanned by the radial velocity observations. Errors increase as the transit predictions are generated for earlier or later times. Light curves were produced with a photometric model of the transit, which assumes that the planets are opaque disks with radii $R = 0.93 R_{\rm Jup}$

[13] Note that the elements reported in Table 1 are osculating orbital elements (see, e.g., Murray & Dermott 1999) referenced to the epoch JD 2,452,490.

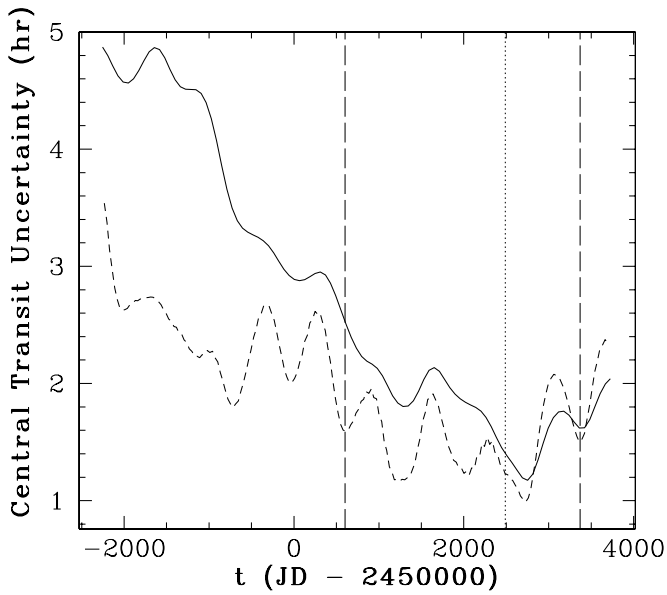

FIG. 1.—Uncertainty in the central transit time for planets Gl 876b (*solid line*) and Gl 876c (*dashed line*). The vertical dashed lines delineate the time span of the Keck RV observations used to generate the coplanar fits that form the basis of our model photometric and RV curves. The vertical dotted line indicates the epoch for the fits (JD 2,452,490.0).

for c and $R = 1.04R_{\rm Jup}$ for b. These equatorial radii are computed using the models of Bodenheimer et al. (2003). The specific intensity of the stellar disk is modeled with a linear limb darkening law, given as

$$I(\mu)/I(1) = 1 - v(1-\mu), \tag{1}$$

where I is the specific intensity of the stellar disk, $v = 0.724$ is the corresponding limb darkening coefficient appropriate to V-band observations of an M4V primary (per Claret 2000), and $\mu = \cos(\theta)$.

Figures 2 and 3 show a selection of model light curves for planets b and c. For planet b, which has an eccentric ($e = 0.22$), rapidly precessing orbit ($d\varpi/dt \sim 44^\circ$ yr^{-1}), the shape of the

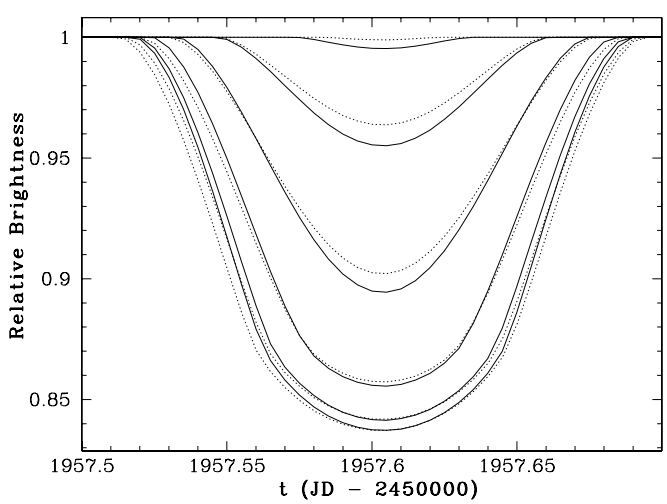

FIG. 2.—Model limb-darkened light curves during a predicted transit by planet Gl 876b when it is near periastron (*solid curves*) and near apastron (*dotted curves*). The curves correspond to different assumed inclinations ($i = 90^\circ$, $89^\circ.9$, $89^\circ.8$,. . ., $89^\circ.5$). The shallowest occur for $i = 89^\circ.5$.

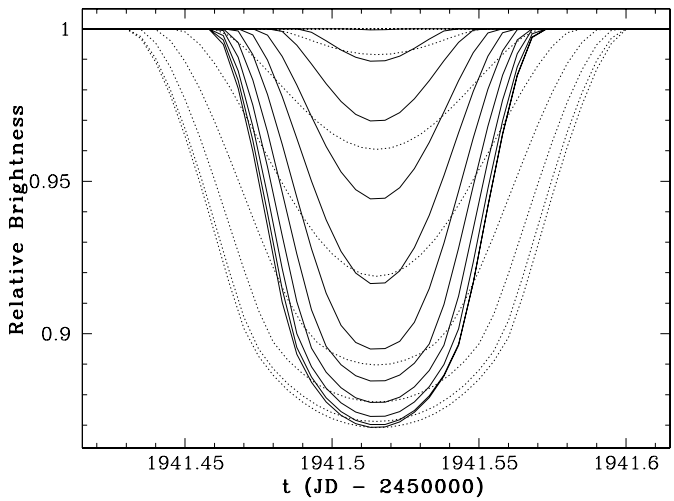

FIG. 3.—Model transit light curves for planet Gl 876c, when it is near periastron (*solid curves*), and near apastron (*dotted curves*). Inclinations, $i = 90^\circ$ through $i = 89^\circ.0$ are shown in decrements of $0^\circ.1$. Planet Gl 876c's eccentricity $e \sim 0.22$ leads to a greater difference in transit depth and duration between periastron and apastron.

predicted curves depends strongly on the osculating periastron angle. For $i < 90^\circ$, the transits are both shorter and deeper when the transits occur near periastron. The orbital eccentricity of planet b is more nearly circular, with $e = 0.025$. In this case, there is little variation in the predicted light curves as the orbits precess. The known transiting planets have transit-to-transit intervals ΔT_i that are evenly spaced to within the current resolution of the observations. HD 209458b, for example, has had individual transit midpoints measured to an accuracy of several seconds (Brown et al. 2001; Wittenmyer et al. 2005), and an average period measured to an accuracy of 83 ms (Wittenmyer et al. 2005; Winn & Holman 2005). If, however, one is able to measure differences in the time intervals between successive transits, one can derive additional dynamical information. As discussed by Miralda-Escudé (2002), Holman & Murray (2005), and Agol et al. (2005), measurements of small variations from exact periodicity can be used to infer the presence of additional bodies in the system, potentially with the masses in the range appropriate to terrestrial planets. In the event that either Gl 876b or Gl 876c were to transit, one would expect the departures from strict periodicity to be large. In fact, successive transits of planet c would occur at intervals differing by as much as 4 hr. By fitting a dynamical model to such transit intervals, one could obtain information regarding all of the orbital elements of the planets (including inclinations and nodes).

3. SEEKING EVIDENCE OF TRANSITS IN THE RADIAL VELOCITY DATA SET

During a planetary transit, the occulting disk of the planet passes over portions of the stellar disk containing a varying component of line-of-sight velocity arising from stellar rotation; this phenomenon produces an asymmetry in the star's spectral lines known as the Rossiter-McLaughlin effect (Rossiter 1924; McLaughlin 1924). The effect has been described in detail in the context of planetary transits by Ohta et al. (2005), and has been analyzed for HD 209458 by Queloz et al. (2000), Bundy & Marcy (2000), and Winn et al. (2005), and for HD 149026 by Wolf et al. (2006). In fact, the transiting planet HD 189733 was initially discovered to transit *not* via photometry, but rather via such in-transit radial velocity variations found by Bouchy et al. (2005). For our study of Gl 876, we compared the observation epochs of all of

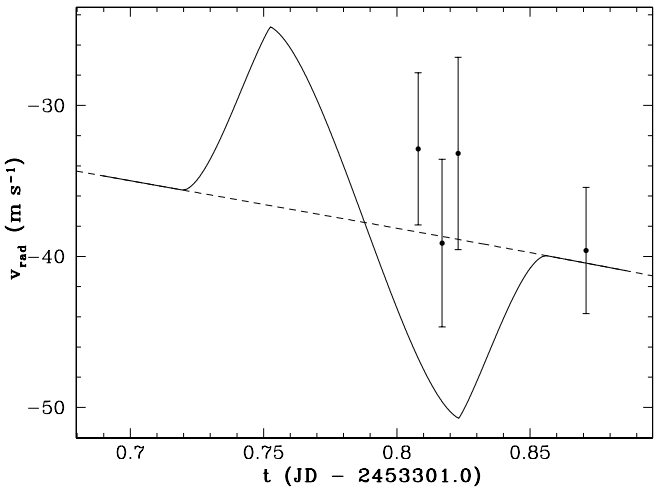

FIG. 4.—Three-planet RV model (*dashed line*) with a superimposed model Rossiter curve (*solid line*) during a predicted transit by planet Gl 876c near epoch JD 2,453,301.79. The observed Keck RV data are shown as the black filled-in circles with error bars.

the Lick (see Marcy et al. 2001) and Keck (see Rivera et al. 2005) radial velocity observations to see if any of these observations occurred during a predicted transit (assuming $i = 90^\circ$). For Gl 876, we used a rotational period that was determined to be 96.7 days using rotational modulation (as reported in Rivera et al. 2005); we used this value to calculate the amplitude of the Rossitter-McLaughlin effect. Four such observations were found, three taken during a predicted transit by planet c, and one taken during a predicted transit by planet b. Figures 4 and 5 display the relevant parts of the radial velocity model (both with and without the Rossiter-McLaughlin effect), with the observations shown. The radial velocity model curves in both figures were generated by adding template curves that use the stellar and planetary radii and limb darkening law given above (and that apply the analytic integrals given in Ohta et al. 2005), to our fiducial $i = 90^\circ$ three-planet radial velocity model. For the transit epoch in the case of planet c (Fig. 4), the data are inconsistent with a transit. In Figure 5, for the outer planet b, the situation is unresolved.

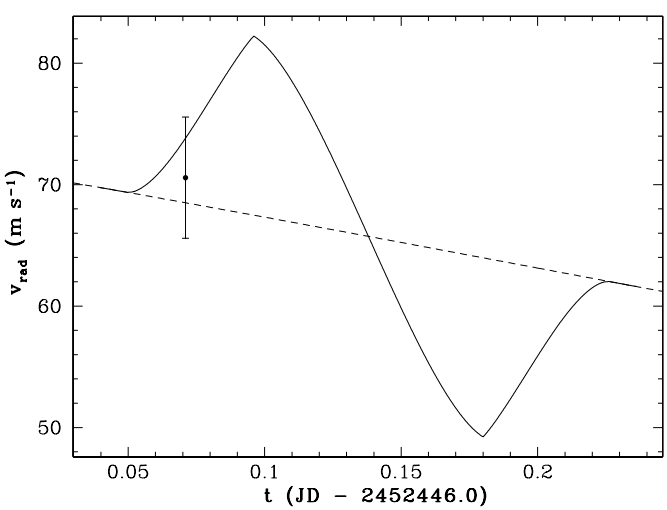

FIG. 5.—Three-planet RV model (*dashed line*) with a superimposed model Rossiter curve (*solid line*) during a predicted transit by planet Gl 876b near epoch JD 2,452,446.14. Again, the observed Keck RV data are shown as the black filled-in circle with error bars.

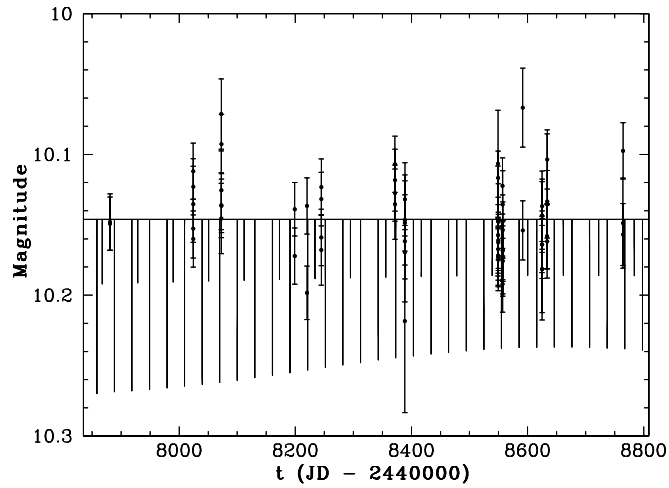

FIG. 6.—Model $i = 89\overset{\circ}{.}6$ light curves for Gl 876b and c superimposed on *Hipparcos* epoch photometry. None of the *Hipparcos* measurements were made near or during a predicted transit window.

4. A SEARCH FOR TRANSITS IN PHOTOMETRIC DATA SETS

We have also compared our model light curves to a variety of photometric data sets for Gl 876 taken since 1989. The results of these comparisons are as follows.

Hipparcos.— The *Hipparcos* mission (see Perryman et al. 1997) produced 67 accepted photometric measurements for Gl 876 (HIP 113020). These measurements have a median magnitude $H_P = 10.148$, with $\sigma = 0.0045$. There is evidence for a weak periodicity when the data is folded at the 96.7 days rotational period of the star (also noted in Rivera et al. 2005). In Figure 6, we plot our model $i = 89\overset{\circ}{.}6$ light curves for Gl 876b and c superimposed on the *Hipparcos* epoch photometry. None of the *Hipparcos* measurements were made near or during a predicted transit window.

Fairborn Observatory.— A number of long-term photometric monitoring programs are being carried out with the automated telescopes at Fairborn Observatory (e.g., Henry 1999; Eaton et al. 2003) and, as described in detail in Rivera et al. (2005), Gl 876 has been on one of the observing programs. Figures 7 and 8 show the Fairborn Observatory data and our corresponding model light

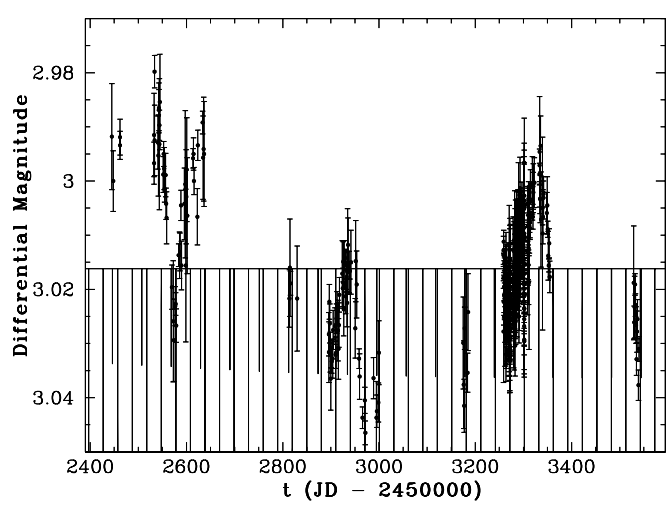

FIG. 7.—Model $i = 89\overset{\circ}{.}3$ light curves for Gl 876b and c superimposed on Fairborn Observatory photometry. Note that the intrinsic long-term variability for Gl 876 over a ~1000 day period is of order 0.05 mag.

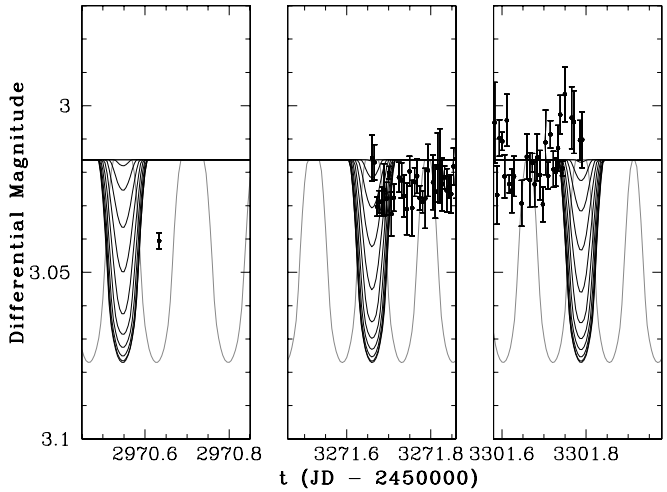

FIG. 8.—Model light curves for Gl 876c superimposed on Fairborn Observatory photometry taken near three individual predicted transit windows. The solid lines correspond to model light curves arising from assumed inclinations running from $i = 90.^\circ0$ to $i = 89.^\circ0$. The light lines correspond to $i = 90^\circ$ model light curves arising from bootstrap fits in which the transit is 3 σ early, 1 σ early, and 1 σ and 3 σ late.

curve for planets b and c. Data taken during predicted transit epochs for planet c show no indication of a transit. The Fairborn Observatory data indicate that long-term stellar variability from Gl 876 is of the order 0.05 mag, which is somewhat smaller than the variation observed with *Hipparcos*.

Transitsearch and AAVSO[14].— Seagroves et al. (2003) describe Transitsearch as a cooperative distributed observing project involving submeter class telescopes worldwide. The Transitsearch strategy is to observe known planet-bearing stars at the dates and times when transits are expected to occur. It is therefore a targeted search, which differentiates it from ongoing wide-field surveys. We identify observing windows for candidate stars through the use of the bootstrap Monte Carlo technique described by Laughlin et al. (2005). The observational campaigns are prioritized by the a priori likelihood that a particular candidate planet will display transits. This likelihood is given by

$$P_{\rm transit} = 0.0045\left(\frac{1\ {\rm AU}}{a}\right)\left(\frac{R_\star + R_{\rm pl}}{R_\odot}\right)\left[\frac{1 + e\cos(\pi/2 - \varpi)}{1 - e^2}\right], \quad (2)$$

where a is the semimajor axis of the orbit, $R_\star$ is the radius of the star, $R_{\rm pl}$ is the radius of the planet, ϖ is the longitude of periastron, and e is the orbital eccentricity.

The first Transitsearch data set for Gl 876 was obtained by one of us (P. D. S. Shankland) from 2003 October 27.9583 to October 28.0368, with a *V*-filtered, 16-bit speckle CCD at the primary focus of a 40.4 cm f/5.1 reflector (at air mass from $\sec z = 2.7$–1.7). The photometric time series shows a monotonic flux increase of 0.16 ± 0.04 mag from 2003 October 27.9583 to October 27.9972. As shown on the left panel of Figure 9, the depth, duration, and timing of this event were consistent with an egress from transit of Gl 876c, in agreement with our predictions. The possibility that a transit had been observed spurred us to orchestrate a distributed observational campaign during the 2004 season.

During the 2004 June 24 opportunity, observations were attempted by 10 observers in Australia. Poor weather thwarted all but one observer, and no transit signal was seen in the data, which covered about half of the 1 σ transit window. Eight Australian and Japanese observers participated in the following 2004 July 24 planet c campaign. They were all clouded out. Weather improved for the 2004 August 23 planet c opportunity, permitting observations by five of the nine Australian, South African, and German observers. No transit signal was seen with photometric depth greater than 1%.

In 2004 October, a number of AAVSO and Transitsearch observers obtained photometry during a closely spaced pair of transit windows for planets b and c. Beginning October 20 11:22 (UT) and ending October 23 15:27 (UT), a total of 2795 CCD observations were obtained. In addition, 2981 photometric observations were obtained in the days immediately before and after the window to set baseline activity and to look for red dwarf flaring. Such a large, distributed network of observers allowed coverage of the window with very few observing gaps over the 3 day period. Gaps in the coverage were smaller than the estimated transit period or forecast window, allowing us to conclude that transits for planets

[14] See http://www.aavso.org.

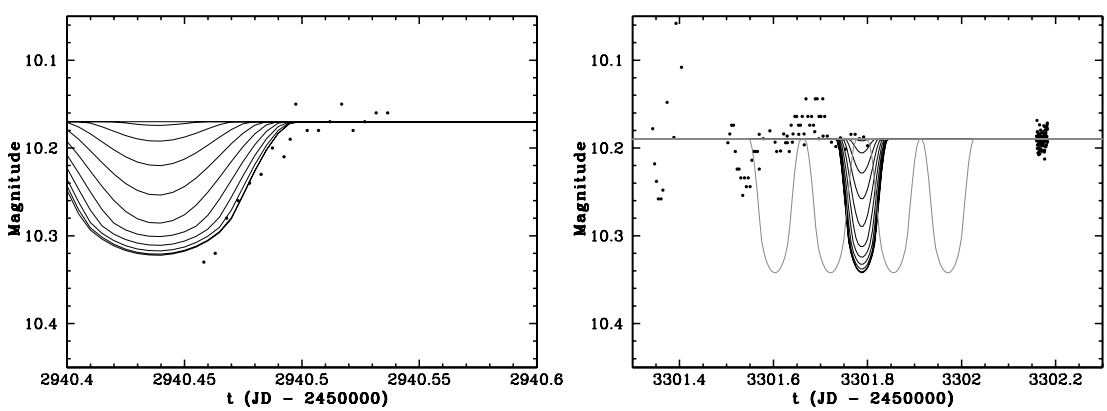

FIG. 9.—*Left*: data for Gl876c, this plate shows dynamical model light curves again for the same decrements of *i*, taken near JD 2,452,940.4381; relative photometry, which began in astronomical twilight (*filled circles*). *Right*: Dynamical model light curves for Gl 876 due to planet c for $i = 90.^\circ0$ through $89.^\circ0$ in $0.^\circ1$ decrements, taken near a predicted transit centered at JD 2,453,301.7879. The data were compiled, baselined, and shifted to employ a mean magnitude of $V = 10.19$, based on relative photometry obtained by AAVSO and Transitsearch (*filled circles*). The light lines correspond to $i = 90^\circ$ model light curves arising from bootstrap fits in which the transit is 3 σ early, 1 σ early, and 1 σ late and 3 σ late.

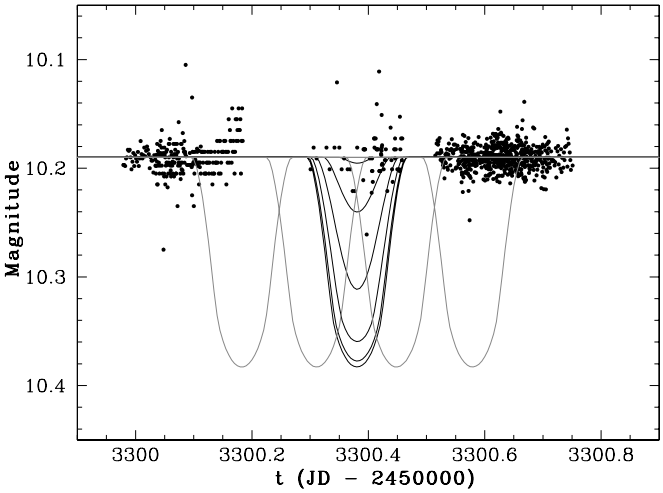

FIG. 10.—Dynamical model light curves for Gl 876 due to planet b for $i = 90\overset{\circ}{.}0$ through $89\overset{\circ}{.}5$ in $0\overset{\circ}{.}1$ decrements, near a predicted transit centered at JD 2,453,300.3806. As with the previous figure, the data were baselined and shifted to employ a mean magnitude of $V = 10.19$, based on relative photometry obtained by AAVSO and Transitsearch (*filled circles*). The light lines correspond to $i = 90^{\circ}$ model light curves arising from bootstrap fits in which the transit is 3 σ early, 1 σ early, and 1 σ late and 3 σ late.

b and c did not occur during the 2004 October campaign. Photometric data from the campaign are plotted in Figures 9 and 10.

Individual observations and uncertainty estimates from the 2004 October campaign are available from the AAVSO Web site, while the other data sets can be found at the Transitsearch website.[15] We are continuing to obtain photometry of Gl 876, with the goal of gaining a better understanding of the photometric variability of mature (age exceeding 1 Gyr) red dwarfs.

5. DISCUSSION

The Transitsearch photometric network has been in operation for 3 yr, and has participating observers capable of providing fully global longitude and latitude coverage. The network maintains a continuously updated catalog[16] of the known census of extrasolar planets. The catalog is currently the only available source for (1) a priori transit probabilities and predicted transit depths for the known extrasolar planets, (2) predicted transit ephemeris and transit window uncertainties based on orbital fits to published radial velocities, and (3) the results of known photometric searches for transits of planet-bearing stars. To date, the majority of negative transit searches have not been reported in the literature. With this paper, we hope to spur a reversal of that trend.

Due to significant uncertainties in the orbital fits, it is generally very difficult to definitively rule out transits by planets with $P >$ 10 day. The Gl 876 planets form a notable exception to this rule because of their high signal-to-noise ratio $\Gamma \sim 50$, and the extensive radial velocity data set allows for a very accurate orbital fit. Campaigns by the Transitsearch collaboration have thus far led to transits of a number of other shorter-period planet-bearing stars being ruled out to a high degree of confidence. The planets for which the possibility of transits have been significantly discounted by our campaigns include HD 217107b ($P = 7.127$ day, $P_{\rm tr} =$ 8.0%; see also Vogt et al. 2005), HD 168746b ($P = 6.403$ day, $P_{\rm tr} = 8.1\%$; see also Pepe et al. 2002), and HD 68988b ($P =$ 6.276 day, $P_{\rm tr} = 9.0\%$; see also Vogt et al. 2002).

Furthermore, planets for which usable photometry of the parent stars has been obtained by our network during the 3 σ transit windows, but for which transits cannot yet be fully ruled out, include HD 188753Ab ($P = 3.348$ day, $P_{\rm tr} = 11.8\%$), HD 76700b ($P =$ 3.971 day, $P_{\rm tr} = 10.0\%$), HD 13445b ($P = 15.76$ day, $P_{\rm tr} =$ 3.4%), HD 74156b ($P = 51.64$ day, $P_{\rm tr} = 3.8\%$), HD 37605b ($P = 54.23$ day, $P_{\rm tr} = 2.2\%$), and HD 80606b ($P = 111.4$ day, $P_{\rm tr} = 1.7\%$). Planets for which campaigns are scheduled to begin soon include GL 581b ($P = 5.366$ day, $P_{\rm tr} = 3.6\%$), and HD 99492b ($P = 17.04$ day, $P_{\rm tr} = 3.4\%$). GL 581 is of particular interest because the primary star is an M dwarf, and the planet (if it transits) will be a Neptune-mass object $M \sin i = 0.052 M_{\rm Jup}$ (Bonfils et al. 2005). The 1.6% transit depth would allow an unprecedented physical characterization of a low-mass extrasolar planet. To date, our Gl 876 campaign has employed the most globally far-reaching distribution, and along with recent leaps in fidelity in similar campaigns, clearly underscores the utility of the network.

What is more, Gl 876b and c constitute a dramatic exception to the emerging aphorism that Jupiter-mass planets are rarely associated with M dwarfs. Indeed, a paucity of giant planets orbiting red dwarfs seems to be a natural consequence of the core accretion theory of planet formation (Laughlin et al. 2004). The core-accretion theory predicts, however, that Neptune-mass and smaller mass planets will be very common around red dwarfs. This stands in contrast to the predictions of Boss (2006), who suggests that the gravitational instability mechanism is the dominant mode of giant planet formation. If this is true, then Jupiter-mass planets should be just as common around red dwarfs as they are around solar-type stars. Efforts to detect transits of small planets orbiting small stars are therefore likely to gain increasing importance and focus over the next several years.

There are, in fact, several observational indications that low-mass planets may be common around red dwarfs. Radial velocity surveys have recently reported the detection of Neptune-mass companions in short-period orbits around the red dwarfs GL 581 and GL 436. The Optical Gravitational Lensing Experiment (OGLE) team of observers using the microlensing method have detected the signature of what appears to be a planet with 5.5 $M_{\oplus}$ orbiting a distant red dwarf (Beaulieu et al. 2006). With these points in mind, we can put the results of our Gl 876 campaign in a broader context. A ground-based (and "fiscally viable") photometric network such as Transitsearch, especially in collaboration with a dedicated bank of telescopes, can capably monitor individual M dwarfs to search for transits of terrestrial-sized planets. Owing to the intrinsic long-term variability of M dwarfs, candidate planets would have to be identified on the basis of a full transit signature in a single time series.

A 0.1 $M_{\odot}$ M dwarf has $R_{\star}/R_{\odot} \sim 0.1$, $T_{\rm eff} \sim 2750$ K, and $L_{\star}/L_{\odot} \sim 5 \times 10^{-5}$; a habitable planet that receives an Earth-equivalent flux from the star thus needs to orbit at a distance of just 0.022 AU, which corresponds to an orbital period of 3.85 days. An Earth-like planet with such a period would be rotationally synchronized to the red dwarf, and in the absence of any significant perturbing bodies, its orbit would be almost perfectly circular. Interestingly, however, simulations show that habitability is unlikely to be adversely affected by a spin-orbit period synchronization. Joshi et al. (1997) used a global climate model to investigate how the Earth's climate would respond if the Earth were tidally locked to the Sun, and found that Earth remains habitable in this configuration, at 1 AU, and perhaps throughout the habitable zone.

[15] Our AAVSO data are available at http://www.aavso.org/data/download/, while other collected data can be found at http://www.ucolick.org/%7elaugh/Gl876/__c.results.html.

[16] Available at http://www.ucolick.org/%7elaugh/.

The $M = 7.5\ M_\oplus, P = 1.9379$ day companion to Gl 876 demonstrates that it is not unreasonable to expect terrestrial-mass bodies on short-period orbits of 0.1 $M_\odot$ stars. R. Montgomery & G. Laughlin (private communication, 2006) have carried out accretion simulations with the Wetherill-Chambers method (Wetherill 1996; Chambers 2001) that model the accretion of terrestrial-mass planets in short-period orbits about M dwarfs. These simulations provide further evidence that terrestrial-mass planets will commonly form in the desired short-period orbits.

If habitable planets do commonly form in orbit around low mass M dwarfs, the chances of detecting and characterizing them are surprisingly good. The transit of an Earth-sized planet will block about 1% of the stellar flux of a 0.1 $M_\oplus$ star. For a planet on a habitable 3.85 day orbit, the transit will be relatively brief, $\sim$40 minutes. The a priori geometric probability of observing such a transit is 2%.

A 1% photometric dip is readily detectable. Amateur astronomers who participate in the Transitsearch collaboration routinely achieve detection thresholds of considerably better than 1%, as evidenced by confirming detections of HD 149026b, which has a transit depth of just 0.3%. Indeed, capable amateur observers have demonstrated the photometric capability to detect the passage of a Mars-sized body in front of an 11th mag 0.1 $M_\odot$ red dwarf.

Inevitably one must ask how many suitable red dwarfs are available on the sky as a whole. Even though the lowest mass M stars are the most common type of star, they are also exceedingly dim. A dedicated 3 m class telescope would be required to properly search the magnitude range $V = 16$–18, where observations of the lowest mass red dwarfs begin to be plentiful (and indeed, many 0.1 $M_\odot$ stars within 10 pc still likely remain to be discovered). In the meantime, however, we recommend that observers obtain high-cadence photometry of nearby single stars listed in the RECONS catalog[17] of the 100 nearest stellar systems; these include Proxima Centauri, Barnard's Star, Wolf 359, Ross 154, Ross 128, DX Cancri, GJ 1061, GJ 54.1, and GJ 83.1. We estimate that each one has a $\sim$1% chance of harboring a detectable transiting, potentially habitable planet, readily detectable by distributed photometric observation.

[17] Maintained by T. Henry and collaborators at Georgia State University.

6. CONCLUSIONS

Our study of Gl 876 has produced several interesting results. We have demonstrated that transits of planets b and c are not currently occurring, and we have thus modestly constrained the parameter space available to observationally allowed orbital configurations of the Gl 876 system. The absence of transits is consistent with the dynamical study of Rivera et al. (2005), who find that a coplanar system inclination $i \sim 50^\circ$ yields the best fit to the radial velocity data. Our dynamical analysis indicates that when planetary transits in a strongly interacting system similar to Gl 876 are eventually observed, then a tremendous amount of information will be obtained. We look forward to the discovery of the first such system.

We have also shown that a globally distributed network of small-telescope observers can effectively provide definitive photometric follow-up of known planet-bearing low-mass stars. Our experience with Gl 876 indicates that intensive photometric monitoring campaigns of individual, nearby M dwarfs constitute a tractable strategy for planet detection. The Sun's nearest low-mass stellar neighbors should therefore be scrutinized very carefully for transits by short-period terrestrial planets. A low-budget survey of this type provides a small, but nevertheless nonnegligible chance to discover a truly habitable world from the ground and within a year or two. Such a detection would be a remarkable and exciting discovery.

We thank K. Johnston, R. Gaume, K. Malatesta, J. Lazio, D. Boboltz, C. Shaw, B. Casey, E. Albert, A. Henden, J. Larsen, D. Katz, C. Phillips, W. Bollwerk, Z. Dugan, J. Jaglowicz, and T. Castellano for useful discussions or other support. We are grateful to the AAVSO and its many members who provided campaign support in addition to those authors listed above. We also gratefully acknowledge the insightful suggestions and constructive feedback offered by our referee. This material is based on work supported by the National Aeronautics and Space Administration under grant NNG04GN30G issued through the Origins of Solar Systems Program to G.L. G. W. H. acknowledges support from NASA grant NCC5-511 and NSF grant HRD-9550561. This research has made use of the Simbad, USNO, and transitsearch databases, operated at CDS, Strasbourg, France, USNO, Washington, DC, and UCSC, Santa Cruz, California, respectively.

REFERENCES

Agol, E., Steffen, J., Sari, R., & Clarkson, W. 2005, MNRAS, 359, 567
Baglin, A. 2003, Adv. Space Res., 31, 345
Beaugé, C., Michtchenko, T., & Ferraz-Mello, S. 2006, MNRAS, 365, 1160
Beaulieu, J.-P., et al. 2006, Nature, 439, 437
Benedict, G. F., et al. 2002, ApJ, 581, L115
Bodenheimer, P., Laughlin, G., & Lin, D. N. C. 2003, ApJ, 592, 555
Bonfils, X., et al. 2005, A&A, 443, L15
Borucki, W. J., et al. 2003, in ASP Conf. Ser. 294, Scientific Frontiers in Research on Extrasolar Planets, ed. D. Deming, & S. Seager (San Francisco: ASP), 427
Boss, A. P. 2006, ApJ, 643, 501
Bouchy, F., et al. 2005, A&A, 444, L15
Brown, T., Charbonneau, D., Gilliland, R., Noyes, R., & Burrows, A. 2001, ApJ, 552, 699
Bundy, K. A., & Marcy, G. W. 2000, PASP, 112, 1421
Butler, R. P., Marcy, G. W., Williams, E., McCarthy, C., & Vogt, S. S. 1996, PASP, 108, 500
Butler, R. P., Tinney, C. G., Marcy, G. W., Jones, H. R. A., Penny, A., & Apps, K. 2001, ApJ, 555, 410
Chambers, J. E. 2001, Icarus, 152, 205
Charbonneau, D., Brown, T., Latham, D., & Mayor, M. 2000, ApJ, 529, L45
Charbonneau, D., Brown, T. M., Burrows, A., & Laughlin, G. 2006, preprint (astro-ph/0603376)
Charbonneau, D., et al. 2005, ApJ, 626, 523
Claret, A. 2000, A&A, 363, 1081
Delfosse, X., Forveille, T., Mayor, M., Perrier, C., Naef, D., & Queloz, D. 1998, A&A, 338, L67
Eaton, J. A., Henry, G. W., & Fekel, F. C. 2003, The Future of Small Telescopes in the New Millennium, ed. T. D. Oswalt (Dordrecht: Kluwer)
Henry, G., Marcy, G., Butler, R., & Vogt, S. 1999, IAU Circ., 7307, 1
———. 2000, ApJ, 529, L41
Henry, G. W. 1999, PASP, 111, 845
Holman, M., & Murray, N. 2005, Science, 307, 1288
Joshi, M. M., Haberle, R. M., & Reynolds, R. T. 1997, Icarus, 129, 450
Kley, W. 2003, Celest. Mech. Dyn. Astron., 87, 85
Laughlin, G., Bodenheimer, P., & Adams, F. C. 2004, ApJ, 612, L73
Laughlin, G., Butler, R. P., Fischer, D. A., Marcy, G. W., Vogt, S. S., & Wolf, A. S. 2005, ApJ, 622, 1182
Laughlin, G., & Chambers, J. E. 2001, ApJ, 551, L109
Lee, M. H., Butler, P., Fischer, D., Marcy, G, & Vogt, S. 2006, ApJ, 641, 1178
Lee, M. H., & Peale, S. J. 2002, ApJ, 567, 596
Lovis, C., et al. 2006, Nature, 441, 305
Marcy, G. W., & Butler, R. P. 1998, ARA&A, 36, 57
Marcy, G. W., Butler, R. P., Fischer, D., Vogt, S. S., Lissauer, J. J., & Rivera, E. J. 2001, ApJ, 556, 296
Marcy, G. W., Butler, R. P., Fischer, D., Vogt, S. S., Wright, J. T., Tinney, C. G., & Jones, H. R. A. 2005, Prog. Theor. Phys. Suppl., 158, 24

Marcy, G. W., Butler, R. P., Vogt, S. S., Fischer, D. A., & Lissauer, J. J. 1998, ApJ, 505, L147
Marcy, G. W., Cochran, W. D., & Mayor, M. 2000, in Protostars and Planets IV, ed. V. Mannings, A. P. Boss, & S. S. Russell (Tucson: Univ. Arizona Press)
Mayor, M., Udry, S., Naef, D., Pepe, F., Queloz, D., Santos, N. C., & Burnet, M. 2004, A&A 415, 391
Mazeh, T., et al. 2000, ApJ, 532, L55
McLaughlin, D. B. 1924, ApJ, 60, 22
Miralda-Escudé, J. 2002, ApJ, 564, 1019
Murray, C. D., & Dermott, S. F. 1999, Solar System Dynamics (Cambridge: Cambridge Univ. Press)
Ohta, Y., Taruya, A., & Suto, Y. 2005, ApJ, 622, 1118
Pepe, F., Mayor, M., Galland, F., Naef, D., Queloz, D., Santos, N. C., Udry, S., & Burnet, M. 2002, A&A, 388, 632
Perryman, M. A. C., et al. 1997, A&A, 323, L49
Queloz, D., Eggenberger, A., Mayor, M., Perrier, C., Beuzit, J. L., Naef, D., Sivan, J. P., & Udry, S. 2000, A&A, 359, L13
Rivera, E. J., & Lissauer, J. J. 2001, ApJ, 558, 392
Rivera, E. J., et al. 2005, ApJ, 634, 625
Rossiter, R. A. 1924, ApJ, 60, 15
Seagroves, S., Harker, J., Laughlin, G., Lacy, J., & Castellano, T. 2003, PASP, 115, 1355
Tinney, C. G., et al. 2006, ApJ, 647, 594
Vogt, S. S., Butler, R. P., Marcy, G. W., Fischer, D. A., Henry, G. W., Laughlin, G., Wright, J. T., & Johnson, J. A. 2005, ApJ, 632, 638
Vogt, S. S., Butler, R. P., Marcy, G. W., Fischer, D. A., Pourbaix, D. Apps, K., & Laughlin, G. 2002, ApJ, 568, 352
Wetherill, G. W. 1996, Icarus, 119, 219
Winn, J. N., & Holman, M. J. 2005, ApJ, 628, L159
Winn, J. N., et al. 2005, ApJ, 631, 1215
Wittenmyer, R. A., et al. 2005, ApJ, 632, 1157
Wolf, A. S., Laughlin, G., Henry, G. W., Fischer, D. A., Marcy, G., Butler, P., & Vogt, S. 2006, ApJ, in press

Chapter 7: GEMSS

The Global Exoplanet M-dwarf Search-Survey (GEMSS) represents an evolution of the research conducted in Chapter 6. As such, it has expanded the search envelope from one star, Gl 876, to what became readily apparent in that study, which is that M dwarfs represent the direction that more of exoplanet research should go. M Dwarfs will very likely be the type of star about which humankind will detect the first Earth-massed terrestrial planets near Earth, and then will characterize them (Tarter et al. 2006). This research has had impact on such a characterization effort already. Because of the published efforts and the initial programs on-line[119], the mantra that 'red dwarfs are the future of exoplanet study', the research has done its part to enthuse the profession with new interest in this spectral type.[120]

During research described, GEMSS developed naturally from the distributed, mobile efforts discussed in Chapters 5 and 6. As a result, Phase I of GEMSS was initiated in 2006 March to capitalize on the Gl 876 experience, and to widen the scope to include a larger sample of red dwarfs. Stars of the M spectral type are favorable sites for exoplanet searches for the reasons discussed when constraining the study to Gl 876 in Chapter 3 and further noted in Chapter 6.

As has been discussed in Chapters 3 and 6, exoplanets are readily detectable in M-dwarf habitable zones (HZs) should they reside there. With the research plan developed, Phase I operations began in 2006 June with the adroit assistance of Z. Dugan (Yale) and some support from J. Jagclowicz (USNA), two undergraduate students mentored by the author. During the initial phase, GEMSS constrained a reasonable target list and, then, designed and performed test operations. Appendix G lists the resulting target list; its development is noted there, online[111], and discussed in what follows. Appendix H lists the results achieved with the completion of Phase I in 2006 November.

Most of the initial GEMSS work demonstrated the validity of the initial concept before proceeding to a large-scale network effort. Phase I was a step up from the Gl 876 distribution, with a larger scientific goal: to detect, observe and constrain characteristics of higher probability, nearby M Dwarf stars. To demonstrate GEMSS optimally during this concept study, balance had to be achieved between large-scale surveys and narrowly targeted searches. Exoplanet hunters enthused about M-dwarfs tend toward survey programs; however; GEMSS

---

[119] see http://gemss.wordpress.com/

[120] As evidence see the list of recent red dwarf detections which are encouraged to be observed published in Chapter 6, and the numbers of red dwarfs studied with detections, in the more recent publication of Chapter 8.

sought to target candidates with higher host probabilities. Although targeting the likeliest candidates might skew an understanding the Galactic M-dwarf planetary system census, it would produce more Earth-like detections in HZs. Appropriate narrowing of the search would lead to a statistical understanding of the planets that *could* be more likely found. Therefore, an understanding of high-probability candidates is desirable. GEMSS had to determine the essential components of a viable plan to observe sufficient M-dwarfs to achieve detection rates greater than 1% while neither constraining the search too narrowly nor broadening it too far.

The impetus for GEMSS stems from the nearness of many M dwarfs, from how common a spectral type they are, and from the greater chance of detecting a terrestrial exoplanet in their HZ's, since HZ radii largely match the semi-major axes of more-detectable exoplanets that orbit M stars.

The M dwarfs are small main sequence stars with masses between 0.08 and 0.50$M_\odot$, and radii of 0.1 to 0.6 $R_\odot$ (Martini & Osmer, 1998). Because the proto-disks for such stars are also small, planets accreted about M stars will lie closer to their parents than in solar-like systems (Laughlin et al 2005). The lower luminosities of M stars also dictate that their HZs will be closer-in than for solar-like systems, and would probably encompass terrestrial orbits.

Therefore, terrestrials could lie within HZs and still transit frequently. As shown in terms of the geometrical relationships in Chapters 2 and 3, transits are easier to observe and appear to more frequently cross the stellar disk for M stars than for solar-like ones. Most of all the small terrestrial-planet-to-red-dwarf radius relationship is greater than for a Jovian-planet-to-G-type star relationship. This means that a greater flux dip is expected for an M star transit by a super-Earth, than for example, the HD 209458 system offers. M-dwarfs maintain a relatively constant luminosity for billions of years, increasing the possibility of life on an orbiting planet. One could speculate that water-bearing worlds could orbit nearby M dwarfs. The detection of such would provide excellent opportunities for astrobiological studies. All these elements, such as the radius relationship, the long, slow burn rate, the convenient HZ, are more conducive to life first here than on other systems.

Conversely, objections to M-star exoplanet searches includes their dimness, the variability of the hosts, the likelihood that such planets might be tidally locked, and that they could suffer from a volatile (organics, water, etc.) deficiency. But these issues are shown to be largely overcome as in the case of the study of Gl 876, and others more recently detected in 2007, such as Gl 581, another red dwarf thought to have a super-Earth-massed planet (Udry et al., 2007). As discussed in Chapters 2 and 3, tidal locking does not negate habitability, this system is sufficiently invariable, and is estimated to have an age of 1 to 8 Gyr (Bonfils et al., 2005; Rivera et al., 2005). M-dwarf exoplanet searches, even with non-detections, contribute to our knowledge of the frequency and distribution of planets at the lower end of the main sequence and help constrain the elusive number of Earth-like planets expected in a system (η_{Earth}), an important part of the Galactic census.

GEMSS has the potential to harvest much fruit and provide opportunities to constrain the understood characteristics for red dwarf systems and their formation. In Phase II, a distributed network will be operated in a manner similar to the 2004 Gl 876 campaign but with numerous continuous-coverage candidates. Although Phase II operations have not begun, Phase I successfully demonstrated the feasibility of the concept with the implementation of a single telescope to dynamically collect continuous data from medium (<200) target lists. The USNO NOTI, which is described in Chapter 4, was the primary telescope used in Phase I. The remotely operated, robotic instrument at Perth Observatory is the next telescope to be incorporated; it will be described in greater detail below. Thus far, JCU colleagues have tested the Perth instrument on Proxima Centauri, and this too was done successfully (Blank et al. 2008, in preparation). The continuing development of GEMSS may be monitored via the program website[1] noted earlier.

Section 7.A. Search – Survey Optimization

A process was developed to select objects for the GEMSS "targeted survey" similar to that which led to Gl 876 becoming the initial target. The Hipparcos Satellite Photometry catalog is of immense value here (Brown, 1997). Evaluation of 12,690 catalogued main sequence stars with spectral types between F and M reveal several dozen whose photometric features are consistent with a planetary transit (Koch,et al., 1998). From such Hipparcos photometry, statistical analyses of known extrasolar planets indicate that ~10% of metal-rich stars have at least one planet, so ~1% of the most metal rich stars will have a detectable planetary

companion. In general, M stars belong to the metal-poor population II stars, which have fewer metals to form terrestrial planets[121]. As GEMSS progresses, this metallicity dependence may prove to reveal few detections – although to date and contrary to this reasoning, seven M-star planetary systems have already been recently discovered (see Chapter 8). Assessing the detection of additional planets orbiting M dwarfs may unravel why lower metallicities seem permitted in the creation of M star exoplanets.

For GEMSS, target choices were restricted to those known to show few signs of activity such as flares or star spots and are within about 50-pc so that they are reasonably bright; have either a V magnitude less than 15, with most brighter than 13, or an R magnitude less than 12. Candidates were further selected for the presence of metals as indicated by a positive metallicity, or iron to hydrogen ratio ([Fe/H] > 0). Additional observational constraints include an air mass of sec(z) below 2.0, a right ascension of between 6^{hr} and 22^{hr}, and a declination between -10 and $+10^{o}$. Equatorial declinations allow for continuous coverage during collaboration with Perth Observatory team members. Stars chosen in the correct region would allow for non-stop coverage while monitoring their flux – and allowing for a rigorously complete, 3 σ coverage scheme. Although this stare mode is a slow cadence for observing larger numbers of stars, the delays are offset by observing the most likely candidates. Studies, such as ASAS (see Chapter 6) and Harvard's MEarth (Nutzmann & Charbonneau, 2007), demonstrate that sufficient flux fidelity, or dwell time on a particular candidate, requires a step-stare approach to ensure a convincing transit is recorded lest the transit be missed or not provable; the resulting timetables which advance much more slowly than the GEMSS pace.

Considering all these constraints, the data on Hipparcos candidates was supplement with information from Simbad[122], Oklo[123], and Vizie-R[124]. The resulting GEMSS Pre Phase-One Planning Baseline (or P^3B) appears in Appendix G. The process to narrow the list further was based on practical constraints, where limiting magnitude, FOV and weather at the site telescopes became a consideration. In particular the practical constraints included air mass, available filtering, camera characteristics, and quadrant and general

[121] Although it proves to be difficult to determine well-constrained metallicities for M dwarfs; see Bonfils (2005).
[122] http://simbad.u-strasbg.fr/simbad/sim-fid
[123] http://www.oklo.org
[124] http://vizier.u-strasbg.fr/viz-bin/VizieR

light-pollution. Such variables were ameliorated by having a dynamic list from, based on available instrumentation and conditions for that run. This dynamic process to narrow the list on a short-term basis was coined GETSUM – the GEMSS Erudition To Synergize Unsimilar Metadata. GETSUM selection was something of an art. The goal was to pick targets useful to all instruments on a "quick-draw" basis from the P^3B list. Many of the targets chosen were also members of the GEMSS High Interest Targets Baseline (or HIT-B) list, a more-constrained list which became the "special reserve" list of targets always considered by the GETSUM process.

Characteristics of HIT-B candidates included, but were not limited to, high proper motion, location within 8 pc of the Sun, recent or notable RV exoplanet detection, 'popular special interest', planetary hosts with suggestive RV-periodogram residuals, hosts of multiple planets not all of which may have been detected, observations in progress by other teams that could benefit from GEMSS photometric synergy and fuller coverage, or otherwise having significant terrestrial-mass detection probability.

The list used for the GEMSS Phase One selection process was itself called the Phase-One Evolved Target List (or PET-L). The PET-L was a natural GETSUM-based evolution of the original P^3B, and was based on any additional practical limitations discovered P^3B candidates. Using PET-L stars as photometric candidates required check stars that could be used across the network of observers to ensure the scientific rigor of any given run. The PET-L Comparison and Check Stars (or P-CACs) list became the list of commonly used check stars, themselves also loosely called P-CACs. Adding a star to PET-L including selecting P-CACs in accordance the check star rules explained in Chapter 3 and Appendix I.
Where possible, the selected P-CACs were useable by collectors with a range of small apertures; however, the FOV limitations did not always allow this. Occasionally, the P-CACs for a specific run would be modified so that all observers during the run could use the same check stars. Lists of P-CACs appear in Appendix G.

Section 7.B. Additional Compelling Matters

GEMSS is coming on-line at a time of increasing interest in M dwarfs due to their potential as examined in Chapter 6. The prospects for stable systems around such hosts appear positive as recently discussed in Udry et al. (2007); Bonfils et al. (2005); Nutzmann and Charbonneau (2007); Rivera et al. (2005); and Laughlin, Bodenheimer & Adams (2005). As discussed in Chapter 6, tidally locked worlds may retain their

atmospheres, and they may also produce protective magnetic fields similar to Earth's field. These effects would improve habitability on such a planet.
There are other oddities to consider with regard to Gl 876. According to the core accretion theory of planetary formation (Laughlin, 2004), gas giants should be rare around red dwarfs. Larger proto-planetary masses acquire gas from the surrounding *in situ* material very quickly producing a gas giant, or Jovian planet. In small red dwarf systems, less *in situ* material (lower metal content) conspire with lower escape velocities to offer less opportunity for planet cores to enshroud themselves in the available gas. Consequently, rocky, terrestrial planets should be the most frequently formed planets about red dwarfs. Curiously, Gl 876 *has two gas Jovians*. With sufficient detections of M-dwarf planets, a statistically meaningful assessment could be made that would put the Gl 876 system in context. In general, why low-metal M stars still produce (apparently) plenty of planets, can be better understood with characterization through detections – which in GEMSS circles is wryly called "putting the PET-L to the metal".

Another matter which may affect what habitability is ascribed to red dwarfs is the long burn rate of the star. The reasons for being among the most long-lived main sequence stars include their low mass hence gravity, conversely higher internal density (internal opacity) and convective nature of their stellar atmospheres. With masses and radii less than a third of our Sun's and surface temperatures below 3,500K, M stars slowly fuse hydrogen into helium via the proton-proton chain, which is the only fusion path available at the minimal core temperatures achieved. This slow burn is likely to last billions to trillions of years (Laughlin & Adams, 1997). Such long-term stability makes terrestrial planets in the corresponding HZs a fertile place astrobiological research, particularly considering that M dwarfs constitute the gamut of the galactic population.

The spectral type distribution must also be considered; the distribution of detectable M dwarfs is inhomogeneous. Because P-CACs should be similar in color and brightness for differential photometry, many FOVs may contain insufficient numbers of P-CACs. GEMSS will eventually employ SIMBAD-compatible, data-mining algorithms to avoid such homogeneities. Currently optimizing FOVs is a manual process. Spot-filter photometry may provide another method of observing targets in FOVs that lack similar-

magnitude (< 1.5 Δ mag) check stars. These would be included with low weights in the current PET-L.

Filter choice is another important consideration for the working PET-L. As with limiting FOV's, the limiting magnitude becomes a factor for intrinsically dim red dwarfs. Filters should accept light from a bandpass matched to the peak of the Wien blackbody spectrum peak; for red dwarfs, the best filter choice in any system is the red one. With such a filter, the fraction of apposite target stars increases usefully. Interestingly, more useable candidates are found above the Galactic plane at galactic latitudes (b) greater than $+10^{o}$ than in the Galactic plane (probably because the candidates are close).

Each of the considerations above played a role in the development and execution of Phase I, which was itself an extension of the Gl 876 efforts, and will be essential for GEMSS Phase II operations.

Section 7.C. First Distributed Site: Perth Observatory

For GEMSS in Australia, D. Blank is slated to operate the Perth Observatory Internet telescope, a relatively new instrument that saw first light in 2005. This telescope was the first distributed collaborator for GEMSS observations and the Australian component has performed its own Phase I tests. Although Blank is closer to Perth than the USNO team is, he is still situated across Australia from the instrument, at JCU in Townsville. The telescope was specifically designed for on-line operations such as Blank and colleagues will need for GEMSS operations.

Fig. 58. Perth Observatory *HOU* Telescope. Credit: Perth Observatory

The RAE (Real Astronomy Experience) 14" (0.36-m) f/11.3 Cassegrain telescope with focal reducer will be the primary GEMSS instrument. It is shown in figure 58. This telescope has a German-equatorial mount and

Bessel *BVRI*-filter set. The associated Apogee CCD FPA is cooled to a nominal temperature of -15º C. The telescope website[125] provides additional technical details; remote control of the telescope is also available on-line[126]. It has been remotely test-run and is capable of the requisite M dwarf photometry.

Section 7.D. Operations

During GEMSS Phase I, the operational cadence was one target per week, as appropriate for a test of program capabilities. With the resolution of most operational quirks, the Phase II cadence is expected to be 3-4 stars every 4-5 days with two stars observed per night; the cadence can be adjustable as necessary for all participants and conditions. The cadence at a particular site may be higher or lower depending on weather and remote-use issues among other potential factors.

USNO will use NOTI if it is available; however, NOTI has been removed from its base in order to test other USNO optics and focal plane arrays, which include the USNO Robotic Astrometric Telescope, (URAT) and the Joint Milli-arcsecond Astrometric Pathfinder Survey (J-MAPS) satellite (see Zacharias, 2004; and Johnston, Shankland & Gaume, 2007). The ULTRA instrument, which is described in Chapter 4, is being fabricated as an alternative. Although its aperture is smaller, the latter's mounting and automation will eventually make it a better fit for GEMSS' requirements than NOTI.

During Constant-Alternating-Distributed Instrument (CADI) operations, cadence must be closely coordinated for hand-offs. At present, Perth automatically takes dark and flat images. With NOTI, USNO participants take flats manually; due to LN2 cooling darks are unnecessary. ULTRA will eventually be automated for auto-calibration. Weather holes will not be considered fatal in CADI operations, but might require dynamic reselection of PET-L stars and PCACs. After one year of Phase II operations, some automated list-selection and field-detection routines will be considered. Photometric folding algorithms in PHP (an HTML-friendly, server-side scripting language similar to Perl and C++) are being developed by the GEMSS team to determine folding-based cadence variations.

---

[125] http://www.perthobservatory.wa.gov.au/education _and_outreach /internet_telescopes.html
[126] http://teleslin.lbl.gov/ index.html

Chapter 8: Characterizing Gl876 Further–a mm Dust Study *(AJ, 2008)*

Section 8.A: Dust and Exoplanets

From the distribution of dust around a star, one can sometimes infer the presence of planets and this dust, is often easier to observe than the planets themselves. Therefore, in order to investigate a number of unresolved aspects of Gl 876 and its multiplanet system, millimeter observations were undertaken to detect a possible dust disk associated with it. These millimeter observations when combined with the earlier optical results further constrained the orbital dynamics and other characteristics of the Gl 876 system. The millimeter observations and analyses described in this chapter have clearly supported the results obtained in the optical. The millimeter observations themselves followed the standard procedures for that subfield.[127] The material presented in this chapter is substantially the same as that which will appear in the *Astronomical Journal* (Shankland et al., 2008).

Section 8.B. Why the Observations

There were several reasons to conduct millimeter research on Gl 876. Most importantly, observing any dust encircling Gl 876 would allow the dust mass and any associated inhomogeneities to be measured and assessed from which estimates of primordial versus debris dust mass could be calculated. Also, if this multi-planet system had a debris disk that would demonstrate that minor bodies had survived evolutionary processes in the system and contribute to our scant knowledge of planetary formation around M dwarfs. Planetessimals alone would produce that dust, and such linking evidence would offer a connection to similarities between solar-like system formation and systems in M stars. Conversely, finding no dust would show that any dust that could have formed by such colliding planetessimals was likely swept clear, most likely by Jovian-massed planets. Coincidentally, at least two of these gas giant planets are in smaller orbits about Gl 876. Having close-in Jovians makes this system a useful testbed for this postulation, which will be discussed in the main paper. The results in that paper

[127] For a solid grounding in the theory and practice of millimeter astronomy, the author referred to http://www.atnf.csiro.au/observers/manuals.html for the operation of the ATCA at 3-mm, and http://www.vla.nrao.edu/astro/ for the operation of the VLA at 7-mm. Additional references may be found in Appendix J, and useful tutorials and visualizations are also found at Burke & Graham-Smith (1997), http://www.physics.rutgers.edu/~dusan/nsiss.html, http://web.njit.edu/~dgary/728/, http://www.narrabri.atnf.csiro.au/astronomy/vri.html, and http://www.haystack.edu/edu/undergrad/materials/RA_tutorial.html.

for this postulation, which will be discussed in the main paper. The results in that paper corroborate the notion that dust disks are uncommon around stars with short-period Jovians. A disk detection might also identify inclinations, resonances with the disc & the planets, and otherwise further refine orbital dynamics put forth in Chapter 6 and in Laughlin et al. (2004), and Rivera et al. (2005). Seeing indications of an inclination of course depends on the resolving power of the collectors, and this issue is discussed further. Numerical modeling of the detected debris in the system would as well be possible, following Deller and Maddison (2005). Finally, a detection would provide an opportunity to study one of the closest disks to Earth. The closest disks known to date include a protoplanetary one about TW Hya at a distance of about 55 pc (Wilner et al. 2006), and the 50 to 210 pc radius disk found about AU Mic (Kalas, Liu, & Matthews 2004), which is at a mere distance of 10 pc.

The protoplanetary disk about TW Hya is significant to this Gl 876 research because both were observed using the VLA at 43 GHz. However, young protoplanetary disks are different from older debris disks, or exo-Kuiper belts, such as might be found around Gl 876. The dust of each is heated by the central star and, subsequently, re-radiates those energies at longer wavelengths, allowing both to be detected by their thermal radiation. Protoplanetary disks will have much more dust which makes any detection of them easier. As protoplanetary dust coalesces or is swept clean, the mechanisms attributed to mature disks take over. These are not fully understood, particularly for red dwarfs, and this issue will be discussed further. For a basic detection, the concentration of dust for both types is still sufficiently dilute that they both be considered optically thin, which means millimeter, optical, and infrared flux densities are proportional to dust density. In some limited cases, dust emission may still be optically thick in which case the flux density reveals the relationship,

$$S_{Dust} \propto 1/e^{\tau},$$

where τ is optical depth and $\tau \geq 1$. This effect occurs as the individual dust grains start blocking the passage of radiation emitted by grains behind them as a consequence of the radiation transfer equation; (Krause 1986). To detect a mature disk for any long-lived M star like Gl 876, one assumes the worse of the two cases, which is that the disk is optically thin and harder therefore to detect. Also note that the assumption was made here that protoplanetary disks and debris disks were considered to be of approximately

similar size, and the observations accordingly were made with a similar antenna configuration to those in protoplanetary disk studies.

With a disk about Gl 876 having an estimated diameter of 200 AU from the above approximations, its angular size would be ~40 arcsec using the classic small angle formula for the system's Hipparcos-derived distance of 4.69 pc[128]. Assuming a cool dust[129] temperature of 20 K, this size is reasonably matched to the millimeter bands. Although the disk around TW Hydrae is not an exo-Kuiper belt, the VLA did detect *that* disk, which indicates that VLA could potentially detect dust about GJ 876. This can be seen by scaling the dust mass sensitivity for this roughly similar source[130] inward to the distance from Earth that Gl 876 lies. In this exercise, one finds that a similar disk around the closer Gl 876 would have a dust mass sensitivity 120 times greater that TW Hydrae has now. Assuming 20 K dust, the corresponding 3-sigma dust sensitivity would be 0.00064 Earth masses beam^{-1}, and detectable by both the ATCA and the VLA.

The results given from the observations of Gl 876 necessitate an understanding of expected disk masses for exoplanetary dust. For mass comparison, the mature debris disk orbiting Tau Ceti has a dust mass of 0.0005 Earth masses while the one orbiting Epsilon Eridani is 0.016 Earth masses (Greaves et al., 2004), which is more than 10 times greater than the Kuiper Belt dust mass in our Solar System. In the research conducted here, the author assumes that a small M dwarf like Gl 876 would have a debris disk somewhat proportionately smaller than the one hosted by the most familiar G2 star, the Sun. This simple deduction rules out the presence of a massive dust ring of the sort around AU Microscopium, but offers the opportunity to discern or constrain any dust to the noise floors of the telescopes used.

Recently, Rivera et al. (2005), Chapter 6 (Shankland et al. 2006), and Appendix C disputed the inclination of Gl 876 based on photometry and radial velocity modeling, and stipulate that the inclination is ~50° rather than that posited by Benedict et al.

---

[128] via precicise parallax measurement. Also, Gl876 is estimated to be 1 Gyr old (see chapter 6), and is felt to be a "mature" system, so that dust is regenerative in nature (discussed in depth in this chapter).
[129] This temperature is typical of cold dust (Lestrade et al., 2006; Hawarden 1993; Beckwith et al., 1990) and within the 10 to 50 K range found across the literature (see the explanation in Shankland et al., 2008, which follows). The cooler temperature is based on a Rayleigh-Jeans black body 35K temperature, but one assumes less energy is transferred to the dust for re-radiation.
[130] This follows Wilner et al. (2000) .

(2002), at ~90°. As will be investigated in some depth in Section E (Shankland et al., 2008), with a resolution to put more than 5 pixels across the extent of any expected disk, the inclination of a detected disk could be inferred. Conversely, this resolution allows that a non-detection may mean the beam looked through an inclined disk which had insufficient flux at such inclination to be detected. As described later in this chapter, these observations could have missed a reasonably formed disk at such an inclination.

The results are discussed at length in the text of the refereed paper. The images of these observations were processed and deconvolved to the extent that no dust was found. The ATCA and VLA images are shown in figures 59 and 60, repsectively. Note that, while the left image (ATCA) is grey-scale, and the VLA image at right is a contour map , both

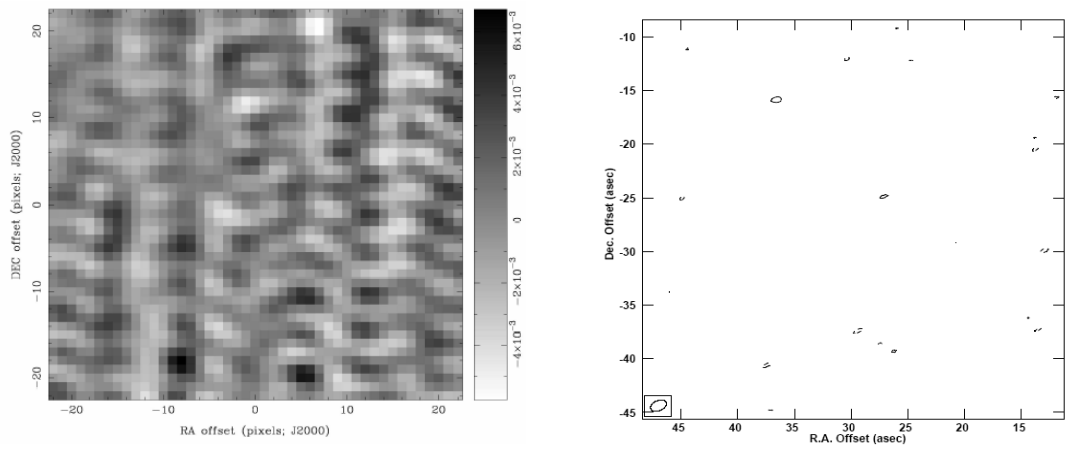

Left (*Fig. 59*): grayscale map of Concatenated 3-mm ATCA dataset at 0.9 mJy/beam noise, not cleaned. Right (*Fig. 60*): Contour map of the total intensity uncleaned image derived from the combined epochs of 7-mm VLA data. Contours are -1 and 1 times the 3σ noise in the image of 130 μJy.

show the same null result.

Section 8.C. Instrumentation and Observation

Radio interferometry is a means to fill the otherwise open aperture common to large radio arrays. Because the apertures required by radio wavelengths are much greater than for the optical band, expense and mechanical limitations begin to limit the size one can build a filled aperture. Being unfilled, interferometry sacrifices some sensitivity in order to achieve a larger jump in fidelity in order to reveal structure of celestial objects at radio wavelengths, on a plane of the sky called the *uv* plane. For the VLA this is done

along three equilaterally spaced arms at once for the research done here. The ATCA operates in two ways. In one, a linear improvement is achieved along one axis, and owing to the rotation of the earth, additional observations are temporally achieved by relying on the rotation of the earth to provide the other baseline. In the H168 configuration used for the observations of Gl 876, the five ATCA antennas form a "T shape", such that three antennas oriented east-west and two oriented north-south, and data is data is taken continuously in both axes as done at the VLA.

Because the image at this stage is interferometric, the *uv* collection is not the image itself, but is a mask on the fourier transform of the image collected. Specifically it reveals where on the Fourier plane the image was sampled. The basic data produced by the array are the visibilities, or measures of the spatial coherence function, formed by correlation of signals from the array's elements. The most common mode of operation uses these data, suitably calibrated, to form images of the radio sky as a function of sky position and frequency. Both interferometers' resolutions are generally diffraction-limited, and thus resolution set by the array configuration and the wavelength of the observation. Note that a synthesis array will not see structures on angular scales both smaller and larger than the range of fringe spacing with respect to the configuration of the antennas. Noise for both systems can be predicted using telescope-specific prediction engines, which generally follow the expected point-source RMS noise calculation:

$$\Delta I_m = \frac{K}{\sqrt{\left(N_{IF}\, T_{int}\, \Delta\nu_M\right) N\,(N-1)}} \quad \text{mJy},$$

where $\Delta\nu_M$ is the effective bandwidth, T_{int} is the total on-source integration time (hours), N_{IF} is the number of intermediate frequencies which will be combined in the output image, N is the number of antennas, and K is a system constant, which depends on the band.

The pointing parameters of the antennas are generally measured under good conditions on a periodic basis. They are then incorporated into calibration. These parameters are strongly air mass and weather-dependent (only at mm frequencies), and as deduced from the name depend on where the telescopes are pointed. As the frequency goes up, winds have an increasing deleterious effect on both this pointing, and the overall

antenna figure. Another more sensitive feature of high frequency radio astronomy is to produce adequate phase calibration. Doing so is a complicated function of source-calibrator separation, frequency, array scale, and weather as well. The effects of the troposphere dominate at the high frequencies, above the 20-cm region. At high frequencies, rapid switching between the source and the nearby calibrator is often used, and was here.

The intereferometric principles apply to the ATCA just as they do for the VLA. The ATCA has recently extended its operational in the range to 106 GHz, which makes it centrally useful to the studies here. Just as with the VLA, the high frequency portion of the spectrum requires the observer heed additional constraints not found at lower wavelengths. Approaching the ATCA's 3-mm where Gl 876 was observed, extra-galactic sources are generally too weak to be used as flux density calibrators, so a Solar system planets' blackbody emissions becomes the best choice as a flux calibrator. For Gl 876 that choice was Uranus, which is in fact the generally preferred flux density calibrator for ATCA. After primary calibration, secondary calibrators help to measure the interferometer amplitude/phase calibration, and hardware automatically corrects for real-time variations in electronics path lengths. Secondary calibration observations generally correct for phase changes in the signal due both atmospheric path changes. Temperature calibration then removes variations in electronics gain. Since it does not account atmospheric opacity, secondary calibrator amplitudes help to correct elevation-dependent opacity variations.

One reason calibration is complicated at millimeter wavelengths is owed to the high resolution which often resolves the standard flux density calibrators, such as 3C48, which is commonly used at the VLA (although PKS J2246-121 was chosen as the best calibrator for this observation). Most of the calibration problems are caused by the atmosphere, where the troposphere introduces rapid phase fluctuations between the antenna elements of the interferometer. Both effects scale with baseline length expressed in units of wavelength, but the latter also heavily depends on the current weather; phases are sometimes observed to wind on time scales of less than a minute. This causes decorrelation during calibrator and target source scans, and requires the observer determine phase-only calibration, before the flux density (i.e., gain) calibration should be attempted.

At millimeter wavelengths, the atmosphere is no longer sufficiently modeled as an ideally transparent hemisphere. Observations degrade because the atmosphere emits radiation seen at this bandpass, and this raises the telescope system temperature, and therefore the noise floor. In addition to working from an imperfect model with a raised system temperature, the atmosphere can severely attenuate the science signal in the millimeter band, creating a general opacity which must be understood and subtracted. This atmospheric opacity is removed from the signal by taking the difference of the effective system temperature measurements and the atmosphere's temperature.

Section 8.D. Synthesis Reduction

The VLA use the Astronomical Image Processing System (AIPS) software as its primary data-analysis package (Greisen, 2006). This software package is used to calibrate and edit radio interferometric data. It then calibrates, constructs, and displays astronomical images made from those data for analysis, through Fourier synthesis methods. Data can be edited in one of many ways. Reduction is first done in the aperture, or *u*-*v*, plane, and image construction is by Fourier inversion. For sufficiently strong sources, one can deconvolve the point source response by 'Clean' or 'maximum entropy' methods[131], which increase the signal to noises of the resultant image. Images can also be combined, filtered, and their parameters estimated. This can be done for the gamut of image and graphical displays. AIPS makes a record of user-generated parameters and operations that affect the quality of the derived images, as history files and can be exported along with the science image in FITS (Flexible Image Transport System) format. AIPS operates from a command line where commands run and reducing of data sub-programs directly.

Processing ATCA data is most often done sone using the Multichannel Image Reconstruction, Image Analysis and Display software, or MIRIAD (Sault & Killeen, 1993). MIRIAD is a similar toolbox which also uses large set of programs to perform

131'Clean' is an iterative algorithm that deconvolves a 'dirty beam' from the flux of a radio source. This creates a synthesized image of the source. Maximum Entropy, or MEM, is also a deconvolution algorithm, but which minimizes a smoothness function, or entrop, in the image. MEM resolution depends on S/N, so resolution is image dependent and varies across the map. It is also biased, since the average of the noise is not zero. See Clark (1980), Schwartz (1978), Hogbom (1974), http://web.njit.edu/~dgary/728/Lecture7.html.

specific tasks such as calibration, mapping, deconvolution and image analysis of interferometric data. AIPS and MIRIAD each have their advantages; AIPS is known to be quite versatile, while MIRIAD automates a number of processes for more [relative] simplicity in the reductions. As with the 7-mm band at the VLA, the ATCA 3-mm observing band is a completely different domain to the other ATCA bands. In both, the science achieved is different, meteorology has a much greater impact, and the observing modes are quite different. Not surprisingly many aspects of the data reduction are also different.

Millimeter effects reflect in both types of reduction; however, the general methods of reduction apply to millimeter astronomy. Because synthesis arrays sample the *u*-*v* plane at discrete locations, the Fourier transform of the source intensity distribution represents incomplete knowledge. By comparison the measured visibility data is essentially the true distribution. Using these, deconvolution algorithms such as 'Clean' and 'MEM' attempt to estimate what must lie in the un-sampled regions of the *u*-*v* plane. Were the image fully sampled, no sidelobes would exist because the sampling function would be constant. A Fourier transform of such a constant would then be a delta function, or in other words, a perfect beam. It can thus be seen that deconvolution attempt to reduce, if not remove, the sidelobes of the dirty beam. This is nonetheless an estimate, a guess, and not actual data in the *u*-*v* plane. Also it should be understood that the solution to a deconvolution is not necessarily unique. Image reconstruction is truly choosing the most reasonable image from the set of possible solutions that the deconvolution path has offered.

The deconvolution via whatever path produces a model of the source. 'Clean' produces a collection of delta functions of the components, while, 'MEM' creates an essentially smooth model. To improve the models produced by eliminating unmeasured high spatial frequency noise, it is usual to `Restore' after deconvolving the data, by *convolving* the model sky with a Gaussian, chosen to match the dirty beam main lobe (called now the Restoring, or Clean Beam). From here, display of the result can be done with internal software, or external programs such as *PGPlot*[132].

[132] See http://www.astro.caltech.edu/~tjp/pgplot/.

Both radio telescopes offered unique opportunities to look for the subtle thermal signatures of mature dust in any disk about Gl 876. The gist of that study produced a number of results, which are revealed in the sections that follow.

The Astronomical Journal, 135:2194–2198, 2008 June doi:10.1088/0004-6256/135/6/2194
© 2008. The American Astronomical Society. All rights reserved. Printed in the U.S.A.

FURTHER CONSTRAINTS ON THE PRESENCE OF A DEBRIS DISK IN THE MULTIPLANET SYSTEM GLIESE 876

P. D. Shankland[1,2], D. L. Blank[1], D. A. Boboltz[2], T. J. W. Lazio[3], and G. White[1]
[1] Centre for Astronomy, School of Mathematical & Physical Sciences, James Cook University, Townsville, QLD 4811, Australia; paul.shankland@jcu.edu.au, david.blank@jcu.edu.au, and graeme.white@jcu.edu.au
[2] U.S. Naval Observatory, 3450 Massachusetts Ave NW, Washington, DC 20392-5420, USA; paul.shankland@usno.navy.mil, dboboltz@usno.navy.mil
[3] Naval Research Laboratory, 4555 Overlook Avenue, SW, Washington, DC 20375-5351, USA; joseph.lazio@nrl.navy.mil
Received 2007 November 8; accepted 2008 March 9; published 2008 May 13

ABSTRACT

Using both the Very Large Array (VLA) at 7 mm wavelength, and the Australia Telescope Compact Array (ATCA) at 3 mm, we have searched for microwave emission from cool dust in the extrasolar planetary system Gliese 876 (Gl 876). Having detected no emission above our 3σ detection threshold of 135 μJy, we rule out any dust disk with either a mass greater than 0.0006 $M_\oplus$ or less than ~250 AU across. This result improves on previous detection aperture thresholds by an order of magnitude, and it has some implications for the dynamical modeling of the system. It also is consistent with the Greaves et al. hypothesis that relates the presence of a debris disk to close-in planets. Due to the dust-planetesimal relationship, our null result may also provide a constraint on the population or composition of the dust and small bodies around this nearby M dwarf.

Key words: circumstellar matter – Kuiper Belt – planetary systems – planets and satellites: general – stars: individual (Gl 876)

1. INTRODUCTION

The M4 dwarf star Gl 876 harbors one of the nearest multiplanet systems detected to date. At a *Hipparcos*-determined distance of 4.69 pc (Perryman et al. 1997), this star is orbited by three planets (Delfosse et al. 1998; Marcy et al. 1998; Marcy et al. 2001). The outer two planets are gas giants, while the innermost is likely to be of terrestrial mass (Rivera et al. 2005). The semi-major axes of these planets range from 0.02 to 0.2 AU. We first targeted Gl 876 to detect any optical transits as described in Shankland et al. (2006).

The search for and study of planetary systems and dust disks around M dwarfs is a relatively new endeavor and the results to date have not been entirely consistent. Only a few debris disks are known around M stars, and Gautier et al. (2007) found no new detections in a *Spitzer Space Telescope* search for dust disks around 123 late-type dwarfs. However, the nearby M dwarf AU Mic shows a well-resolved debris disk, whose radius is between 50 and 210 AU (Kalas et al. 2004). In addition, Gl 842.2 (Lestrade et al. 2006) was shown to have a ~300 AU disk, and Gl 182 (Liu et al. 2004) was found to have a ~120 AU one. These suggest that Gl 876 could reveal a disk if it had one.

A disk detection is important in that it would offer a better understanding of the Gl 876 system, and it would begin to provide clues about planet formation around M dwarfs. M dwarfs comprise three-fourths of the galactic population, making any detection important to understanding plant formation for this most common type. A detection would also help to characterize a particularly diverse and nearby planetary system. Separate from the potential to witness disk disturbances which might reveal planets, a disk detection would further determine whether mature dust disks signal the presence of planets in a system, and help constrain whether debris disks are the ubiquitous result of planetary formation. Conversely, detecting *no disk* would still be helpful as it would set the system's upper mass limit.

Right now the inclination in Gl 876 is not well understood, and assessing any such "tilt" would help indicate whether the inclination approaches $i \approx 50°$, or is more like $i \approx 90°$. The former is contended as a result of radial-velocity reductions, as discussed in Rivera et al. (2005) and Shankland et al. (2006). The latter is derived using astrometric data from *Hubble Space Telescope*'s (*HST*) Fine Guidance Sensor (FGS) by Benedict et al. (2002). Learning a system's inclination (presuming the disk is coupled to the plane of orbits) is invaluable to a complete understanding of systems and the true mass(es) of their planets. Optical radial-velocity measurements are limited to providing a mass limit, M (sin i). Any additional constraint on i helps constrain the M (sin i) mass (and vice versa), which can then lead to constraints on density, composition, and ultimately, habitability.

Modern millimeter interferometers (e.g., Very Large Array (VLA)[4] and the Australia Telescope Compact Array (ATCA)) offer arcsecond resolution which can give information beyond a simple detection. Such capability could also shed qualitative light on a system's dynamical inclination, as shown in Lestrade et al. (2006). If the Gl 876 system were to contain a debris disk, the extent of which exceeds just ~5 AU (which is our resolving power at 4.69 pc), then imaging observations could not only resolve the disk but also provide some geometric constraint on the inclination of the system. Of course the disk would have to have some "optical thickness" in order to observe any gradient consistent with an inclination.

Lestrade et al. (2006) found a disk around GJ 842.2, and refer to the one about Gl 182 found by Liu et al. (2004). Both disks are large enough (~100 AU) that they could be cleanly resolved by us. In their own quest for dust about our target Gl 876, Trilling et al. (2000) demonstrated their ability to discern inclination from their dust-disk observations of three *other* (G-type) stars using Cold Coronagraph with the Infrared Telescope Facility (IRTF), an instrument with less resolving power than the VLA and the ATCA. These precursor observations

[4] The VLA is operated by the National Radio Astronomy Observatory, which is a facility of the National Science Foundation, operated under cooperative agreement by Associated Universities, Inc.

assured us that some general inclination information could be extrapolated from the appearance of any disk.

Other specific issues would be clarified with an improved understanding of dust disks about M dwarfs. Since dust has a short lifespan throughout a disk due to radiation pressure, Poynting–Robertson drag and gravity, it has to be regenerated to maintain the disk. This is done by the larger bodies which collide and so shed dust. Thébault et al. (2003) assert this for β Pictoris, and such a disk about Gl 876 would infer that a solar-like Kuiper-like belt might exist. While this relationship is expected in many disks, the planetesimal-dust relationship is not so clear for M dwarfs.

A lack of dust may also support the Greaves et al. (2004) hypothesis—that debris disks are uncommon around stars with close-in giants, presumably due to the short lifetimes of the parents of debris disks and a sweeping effect. For Greaves' hypotheses, Gl 876 is a good test. A disk would also specifically imply that rocky or icy bodies exist that are left over from the system's formation. A detection would also mean any planet-inferring asymmetries could be studied, as done for the HR 4796 disk (Wyatt et al. 1999). Certainly Gl 876's radial-velocity-derived 2:1 planetary resonance between Jovian planets "b" and "c" would lead one to seek additional correlations with any of the dust disks, such as Quillen & Thorndike (2002) reported in ϵ Eridani's ring. A general census of M-star dust disks would generally improve understanding of planet formation in general, as described in Apai et al. (2007).

Our search for thermal dust emission using the ATCA at 3 mm (94 GHz) and the VLA at 7 mm (43 GHz) produced a result that offered a series of useful insights. Specifically in Section 2, we describe our ATCA millimeter search, and in Section 3, we describe similar millimeter work done with the VLA. In Section 4 we describe our combined results, and then in Section 5 we discuss the implications of our null result.

2. OBSERVATIONS

We observed Gl 876 at both 3 and 7 mm with the ATCA and the VLA, respectively. Table 1 summarizes the observing details.

2.1. 3 mm Australia Telescope Compact Array Observations

Our 3 mm ATCA observations were conducted on JD 2453626 with five of ATCA's six 22 m antennas. Uranus was observed for 15 min as the primary calibrator. The secondary calibrator (PKS B2246 + 121) was then observed for 3 min and every fourth pair of target/secondary scans was followed by a "paddle" observation for absolute calibration. The total time on the target was 2.5 h with the IFs set at 93.5 and 95 GHz. Table 1 provides further details on the observations.

Data reduction was done using Multichannel Image Reconstruction, Image Analysis and Display (Sault & Killeen 1993, thereafter MIRIAD). The data sets from both intermediate frequencies (IFs) were edited and calibrated separately, but combined in imaging in order to maximize sensitivity. From this we produced a continuum image with a restoring beam of $2.75'' \times 2.75''$ with an rms noise floor at 0.9 ± 0.01 mJy beam^{-1}. Nineteen beams were the required minimum to cover the notional disk. We found no dust emission in the image and stopped reduction there. Our image covered the $\sim 55''$ extent of a notional $\sim$200 AU debris disk.

Table 1
ATCA and VLA Configurations

Parameter	ATCA	VLA
Date (2005)	Sep 12	Oct 14 (epoch 1)
Date (2005)	...	Nov 01 (epoch 2)
Julian date	JD2453626	JD2453658 (epoch 1)
Julian date	...	JD2453676 (epoch 2)
Frequency (GHz)	93.5, 95 ($\sim$3 mm)	43.315, 43.365 ($\sim$7 mm)
Mode	Continuum	Continuum
Elements	5 of 6	23 of 27
Bandwidth (MHz)	128, 128	50
Synthesized beam (arcsec^2)	2.75×2.75	1.47×0.93
Configuration	H168	DnC, D
Time on target (h)	2.5	3.4
Cycle (s)	10	80 (source), 30 (cal)
Epochs total (h)	1×4.5	2×2
$S_{3\sigma}$ (mJy beam^{-1})	0.9 ± 0.01	0.04 ± 0.003
Phase calibrator	PKS B2246 + 121	PKS B2246 + 121
Flux density calibrator	Uranus	3C48

2.2. 7 mm Very Large Array Observations

The 7 mm observations at National Radio Astronomical Observatory (NRAO) VLA took advantage of the dynamically scheduled period during array re-configurations. Epoch 1 was centered on JD 2453658 while epoch 2 was centered on JD 2453676. Again, Table 1 details the observations. For the first epoch, we used the hybrid DnC configuration with the north arm in the C configuration while the east and west arms were in the more compact D configuration. The second epoch occurred in full D configuration. For both of our VLA epochs, we used the full complement of available antennas (23 of 27 25 m antennas), and observed for a total 3.4 h. The synthesized beam of the VLA is $1.47'' \times 0.93''$. From the VLA data we produced a 512×512 pixel image with a spacing of $0.2''$ per pixel. The resulting $\sim 100 \times 100''$ image covers the $85''$ extent of a 400 AU debris disk. We used 30 beams to cover the linear extent of the potential disk.

We reduced the two epochs using Astronomical Image Processing System (Greisen et al. 2006, thereafter AIPS) and calibrated each epoch independently. We set the absolute flux density scale using a computed flux density of 0.53 Jy for the extragalactic calibrator, 3C48. Extragalactic calibrator source, PKS B2246 + 121, was used to estimate the instrumental and atmospheric phase fluctuations. We then applied phase corrections to the target source data. Gl 876 and PKS B2246 + 121 were then imaged at each epoch and concatenated into a single calibrated data set, and then imaged again. This resultant $35'' \times 35''$ contour image from the combined data showed no apparent emission. The VLA dirty map's rms noise floor was at 44 ± 2.5 μJy beam^{-1}. Finally, we applied a variety of uv-plane tapers and ranges besides these to extract any missed detection. This additional processing also failed to produce a detection.

3. RESULTS

In this section we use our upper limits on the millimeter emission from Gl 876 to constrain the properties of any debris disk orbiting it. Following standard formulae (e.g., Lestrade et al. 2006; Dent et al. 2000), we relate the flux density upper limits to the dust mass of an optically thin debris disk as

$$S_\lambda = \frac{M_{\rm dust} B(\lambda, T_d)\kappa}{D^2}, \quad (1)$$

where S_λ is the observed flux density at the given wavelength, $M_{\rm dust}$ is the dust mass in the disk, κ is the mass opacity, and $B(\lambda, T)$ is the Planck blackbody function for dust at temperature T. To provide a new constraint on the dust mass, we solved for mass using a 3σ noise floor.

For the temperature T of the dust particles, we assume a cool $T \approx 20$ Ks (see below), and also a less radiant energy is transferred to the dust than in the ideal case. Classic 1 μm sized Lambertian, spherical dust particles are generally assumed to have an albedo a_d for the dust where $a_d \approx 0.06$ (Brown et al. 1997; Jewitt et al. 1996; Luu & Jewitt 1996).

Since the dependence of temperature with a typical star-to-dust distance is $d^{0.5}$, the temperature at 30 AU outward will differ little, so we use one temperature to approximate the disk. But since M dwarfs are less luminous than G-type stars by $L \approx 0.1$ to $0.001 L_\odot$, they irradiate their circumstellar dust to a lesser $\leqslant$20 K than for the 35–50 K expected from dust about solar-like stars (Lestrade et al. 2006; Beckwith et al. 1990). The distance D is known with a high accuracy to be 4.69 pc. For the mass opacity in the most fundamental scenario, we presume the disk to be optically thin, and thus adopt a standard value of

$$\kappa = \kappa_0 \left(\frac{\lambda_0}{\lambda}\right)^\beta, \tag{2}$$

where $\kappa_0 = 1.0\,{\rm cm^2 g^{-1}}$. Owing to the wide disparity in postulated values for the opacity spectral index from 0.2 to 3.0, we will somewhat arbitrarily assume $\beta = 1$ as a starting point. Clearly our results will depend upon the assumed temperature and mass opacity. Should debris disks around M dwarfs turn out to have dust with, for instance, significantly lower mass opacity than that around earlier-type stars, we would have underestimated the dust mass in the Gl 876 system.

To prepare for a notional detection, we first assumed a disk diameter. At the distance of 4.69 pc, 1″ equals 4.69 AU, so the resolution (the number of divisions into which our telescopes' beams are divided) is equivalent to a linear scale of 12.7 AU. One possibility is that any disk would be unresolved because of its size. The debris disk is unlikely to extend much closer in toward the star than the outermost planet, which lies at a semi-major axis of 0.2 AU. Such arrangement allows a scenario where any disk would be unresolved with our instruments. However, guided by the known debris disks around M dwarfs (e.g., AU Mic, Gl 842.2, Gl 182), we shall assume a simplistic disk diameter of ∼200 AU (or ∼42.6″) here. This assumed disk would be well within the primary beams of the VLA and the ATCA and would even allow a disk to be resolved by the 4.69 divisions spread over the extent of the beam. In fact, we made images of a much larger > 100″ region as a precaution, so that we could detect any disk as large as even 225 AU in radius.

The assumed size of the disk becomes relevant to the value of the noise floors of the VLA and the ATCA, which provide a limiting value for observed intensity. These must be related to a flux density by assuming the area of a possible disk.

It is important to understand how (and when) inclination affects any detection above the noise floor. First it is statistically unlikely that the disk will be exactly face-on, nor edge-on. There exists a higher probability of being detected at some intermediate inclination. As with visual detections of edge-on transits at $i = 90°$, the geometric *a priori* likelihood of a single inclination is given by

$$P = 0.0045 \left(\frac{1\,{\rm AU}}{a}\right)\left(\frac{R_* + R_{\rm disk}}{R_\odot}\right), \tag{3}$$

where a is the semi-major axis of the orbit, R_* is the radius of the star and $R_{\rm disk}$ is the thickness of the disk, arbitrarily chosen here to be $\sim 3 R_{\rm Jup}$. In the case of Gl 876, we also assume $R_* = 0.3 R_\odot$, and for a notional disk we choose a to be a mean 100 AU. The result is ∼2% for any given inclination about Gl 876, and a strictly geometric probability of ∼40% for a range of i from 40° to 60°. Probabilistically, it is more likely that the Gl 876 disk is not edge-on but has some lesser inclination. The lesser the disk is inclined from "edge-on" to "face-on," the more the disk surface brightness decreases, thus making a null detection more likely as the flux density drops beneath the noise floor. Also, the disk must have some optical thickness (as described for younger disks in Takeuchi & Lin 2003, 2005) in order for us to have observed a gradient, and thus infer any tilt. As the study of M-star disks is relatively adolescent, it is not clear at this point how thick Gl 876's disk might be. In any event, such an opportunity for a disk to escape detection would be consistent with previous optical observations.

We solved for the dust mass using the rms noise floor for each radio telescope as a threshold, or a minimum detectable mass. The 3σ upper limit of 135 μJy on any undetected mass then becomes 0.0006 $M_\oplus$ for the area of a nominal 200 AU radius disk, for the more stringent VLA results.

4. DISCUSSION

As previously mentioned, Trilling et al. (2000) used NASA's IRTF Cold Coronagraph (CoCo) at 1.62 μm to search for a circumstellar disk around Gl 876, and produced their own null result for this system. However, their observations were less sensitive (3.6 times less so), and moreover were restricted to a narrow, 5″ (25 AU) beam width. Based on the size of the few red dwarf disks detected since their observations, this beam width was likely insufficient to assert that any M-dwarf disk does or does not exist about Gl 876. This beam easily could have missed a disk by looking at the cleared central hole in it.

Other observations of nearby stars done by Greaves et al. (2004) in fact provided additional impetus to do similar observations for Gl 876. From their observations they estimate that the ϵ Eridani and τ Ceti dust disks have 0.016 and 0.0005 $M_\oplus$ dust masses, respectively. As further comparison, AU Mic is a much younger M star at double the distance (∼10 AU), and whose edge-on disk has a radius of between 50 and 210 AU. While the AU Mic disk is just one example, its minimum size also gave us confidence that any Gl 876 disk would also likely be resolved in our VLA and ATCA observations. Admittedly, strict comparisons between AU Mic and Gl 876 would be limited owing to the age difference, but seeing an older disk about Gl 876 would allow this age difference to be exploited in a first-time age comparison.

In the end, our improved beam width and sensitivity still proved insufficient to detect a larger, fainter disk similar to these, but we can say that our observations had a sufficient beam width to surely detect any Kuiper-like disk whose flux rose above the VLA noise floor of 44 μJy, if other factors did not cause the non-detection. In such a simplistic scenario we assert that no disk exists at the mass limit posed, if we assume that the dust is essentially optically thin.

The mass constraint that an upper mass limit puts on Gl 876 has dynamical implications worth exploring. The reasoning which allows resolved disks to be used to infer an inclination follows Lestrade et al. (2006). As noted earlier, they resolved a debris disk about GJ 842.2 at a shorter wavelength of 0.85 mm. This was done with sufficient resolution on

James Clerk Maxwell Telescope's Submillimetre Common-User Bolometer Array (SCUBA). Their results suggest that GJ 842.2 was generally inclined; for the same reasons inclination could be discernible for Gl 876.

The curious dynamics the Gl 876 system exhibits is due to its two outer Jovian planets which are locked in a 2:1 mean resonance, discussed in Laughlin et al. (2004, 2005), and Marcy et al. (2001). In 2002, Benedict et al. reported that their *Hubble* FGS astrometry of Gl 876 revealed an inclination of $i \approx 90^\circ$. However, the 2005 inner planet detection prompted Rivera et al. to revisit the inclination issue, which instead appeared to be $i \approx 50^\circ$. This more-tilted inclination was found to be consistent with 3σ photometry and radial-velocity transit reduction by one of us (Shankland et al. 2006), using reduction methods shown to be viable in Kane (2007). It is statistically likely that a positive dust detection would have probably suggested some inclination if there were some opacity—and thus support of one set of these conflicting optical observations.

On the other hand, a negative detection (as is the result here) suggests that a thin-dust mass could still exist about Gl 876 if the dust density were below the detection threshold of the individual VLA or ATCA resolution per pixel, or the overall upper mass limit. The, as yet, poorly understood dust density, temperature, spectral index, opacity, and optical thinness muddies our understanding of the mechanisms at play, and inclination would be a factor in each of these. Still, there are other possibilities for our null result. Another may be that the formation and evolution of systems (disks and planets) is different in M dwarfs. At the least, any unexpanded composition in the system would lead to misunderstood opacities, albedos, radii, or blackbody behavior.

As we have suggested, we also could have missed any disk owing to a less-than edge-on orientation that would have reduced the surface brightness in a less-than-transparent disk. Slipping under this threshold (and the noise floor of the VLA and the ATCA) at lower inclinations would be a result which favors the $i \approx 50^\circ$ scenario posited by Rivera et al. (2005) and Shankland et al. (2006). $i \approx 90^\circ$ of Benedict et al. could instead be correct if the disk were edge-on, but the mass is small, at 0.0006 $M_\oplus$. Our non-detection thus offers a two-variable constraint. Until the basis for a non-detection is constrained further, we can also at best *suggest* that Greaves' hypothesis appears to remain intact. More work clearly needs to be done to understand the properties of debris dust about M stars. Further, if these initial suppositions are correct, Gl 876's lack of dust also suggests few planetesimals in the system.

So our results suggest that further scrutiny of M stars is needed in order to understand how their systems differ from solar-type stars, particularly since M dwarfs have a demographic monopoly on the galaxy. More sensitive observations of this and other M stars would also begin a foundation for further numerical modeling of their disks (or lack thereof), as suggested in Deller & Maddison (2005). Certainly, any connection of dust to terrestrially-massed planets will fuel an interest in the increased scrutiny of M dwarfs. From the recent optical detections, the growing consensus is that red dwarfs may very well harbor the first discovered exo-Earths.

It is also worth mentioning that because of the low luminosity of M dwarfs (below $0.1 L_\odot$) that leads to cooler dust about them, sub-millimeter or millimeter telescopes may be more sensitive than mid-infrared ones in detecting such planet-associated disks. We would encourage observations at these wavelengths to be explored further. In particular, we recommend that the six M dwarfs found with planets so far be comprehensively checked for dust, to include Gl 876 (with greater sensitivity than us), Gl 436 (Butler et al. 2004), Gl 674 (Bonfils et al. 2007), Gl 849 (Butler et al. 2006), Gl 581 (Udry et al. 2007), and GJ 317 (Johnson et al. 2007). Understanding the dust in such planet-bearing systems (as addressed in Dutrey et al. 2004) may be a key not just to making a first exo-Earth detection, but will more importantly offer a broader understanding of planets and their formation about the populous M-type stars.

5. CONCLUSIONS

We used the VLA and ATCA at millimeter wavelengths to search for thermal radiation from cool dust from the GL 876 system, and achieved the null result which improved upon previous limits. We observed no such emissions to 3σ, at the 135 μJy rms detection threshold. From this we calculated that any dust mass that might still be there had to be constrained to be a mass less than 0.0006 $M_\oplus$ for a nominal 200 AU radius disk. Our 3σ noise floor was established during our most sensitive observations with the VLA, and were consistent with our ATCA observations. This constraint does not generally contravene Greaves' postulation that a system's bodies sweep out regenerated dust. Since the disk inclination affects the surface brightness (depending on our "emerging" understanding of opacity, temperature, spectral index, density, and thinness), this lent qualitative constraints on how the system might be inclined. All things being equal a non-detection is more consistent with a lower inclination than a higher one.

For Gl 876, our result most importantly places basic constraints on the limits afforded by the instrumentation, and a more stringent upper $M_\oplus$ limit on any potential exo-debris there. While a lower-mass debris belt might be found for Gl 876 with greater sensitivity, the null observations we find thus far corroborate the effects of close-in Jovian planets. For Gl 876 in particular, we offer four solutions to explain this non-detection. Alternatively the system is less dusty or is optically thinner at the more detectable $i \sim 90^\circ$, or is "dustier" yet less detectable at some less edge-on inclination. The third possibility is that this red dwarf dust is comprised of material which is not similar to comparable disks about solar-like stars (e.g., has a different spectral index, thinness, temperature or opacity), and so evades detection for now. Finally, while it would be physically very unlikely, a disk (or instead a central hole) could have been larger than ~400 AU. Answers will remain enigmatic until a more sensitive dust study of Gl 876 is done, and more generally, a robust, low-bias census of M-star systems is completed.

We thank K. Johnston, G. Laughlin, R. Gaume, and J. Pier for useful discussions, feedback or other support. We also thank the referee, whose insightful feedback greatly improved the presentation of this paper. The Australia Telescope is funded by the Commonwealth of Australia for operation as a National Facility managed by CSIRO. The National Radio Astronomy Observatory is a facility of the National Science Foundation operated under cooperative agreement by Associated Universities, Inc. NRL astronomical research is supported by Navy 6.1 funding, and USNO astronomy is supported by Navy RTDE and OMN funding. P.D.S. thanks the NRAO staff for their support at Socorro. D.L.B. thanks the staff of the ATNF for their hospitality both at Narrabri and Epping.

REFERENCES

Apai, D., Luhman, K., & Liu, M. 2007, arXiv astro-ph/0702286
Beckwith, S., Sargent, A., Shini, R., & Güsten, R. 1990, AJ, 99, 924
Benedict, G. F., et al. 2002, ApJL, 581, 115
Bonfils, X., et al. 2007, arXiv:0704.0270
Brown, R., Cruikshank, D., Pendleton, Y., & Veeder, G. 1997, Science, 276, 937
Butler, R. P., Johnson, J., Marcy, G., Wright, J., Vogt, S., & Fischer, D. A. 2006, PASP, 118, 1685
Butler, R., et al. 2004, ApJ, 617, 580
Carrol, B., & Ostlie, D. 2007, An Introduction to Modern Astrophysics (2nd ed.; San Francisco, CA: Pearson Addison Wesley)
Delfosse, X, et al. 1998, A&A, 338, L67
Deller, A., & Maddison, S. 2005, ApJ, 625, 398
Dent, W., Walker, H., Holland, W., & Greaves, J. 2000, MNRAS, 314, 702
Dutrey, A., des Etangs, A., & Augereau, J. 2004, in Space Science Ser., COMETS II, ed. R. Binzel (Tuscon, AZ: Univ. of Arizona Press) (arXiv astro-ph/0404191)
Gautier, T., et al. 2007, ApJ, 667, 527
Greaves, J., Holland, W., Jayawardhana, R., Wyatt, M., & Dent, W. 2004, MNRAS, 348, 1097
Greisen, E., et al. 2006, AIPS Cookbook, http://www.aips.nrao.edu/cook.html
Jewitt, D., Luu, J., & Chen, J. 1996, AJ, 112, 1225
Johnson, J., Butler, R., Marcy, G., Fischer, D., Vogt, S., Wright, J., & Peek, K 2007, arXiv:0707.2409
Kalas, P., Liu, M., & Matthews, B. 2004, Science, 303, 1990
Kane, S. 2007, MNRAS, 380, 1488
Laughlin, G., Bodenheimer, P., & Adams, F. C. 2004, ApJ, 612, L73
Laughlin, G., Butler, R., Fischer, D., Marcy, G., Vogt, S., & Wolf, A. 2005, ApJ, 622, 1182
Lestrade, J., et al. 2006, A&A, 460, 733
Lissauer, J. 2007, ApJ, 660, L149
Liu, M. C., et al. 2004, ApJ, 608, 526
Luu, J., & Jewitt, D. 1996, AJ, 111, 499
Marcy, G. W., Butler, R. P., Fischer, D., Vogt, S. S., Lissauer, J. J., & Rivera, E. J. 2001, ApJ, 556, 296
Marcy, G., Butler, R., Vogt, S., Fischer, D., & Lissauer, J. 1998, ApJ, 505, L147
Perryman, M., et al. 1997, A&A, 323, 49
Quillen, P. C., & Thorndike, S. 2002, ApJ, 578, L149
Rivera, E. J., et al. 2005, ApJ, 634, 625
Roccatagliata, V., Henning, Th., Wolf, S., Carpenter, J. M., & Rodmann, J. 2007, in IAU Symp. 243, Star-disk Interaction in Young Stars (Grenoble: IAU), May 21–25, http://www.iaus243.org/IMG/pdf/Roccatagliata.pdf
Sault, R., & Killeen, N. 1993, MIRIAD Cookbook, http://www.atnf.csiro.au/computing/software/miriad/
Shankland, P., et al. 2006, ApJ, 653, 700
Thébault, J., Augereau, J., & Beust, H. 2003, A&A, 408, 775
Takeuchi, T., & Lin, D. 2003, ApJ, 593, 524
Takeuchi, T., & Lin, D. 2005, ApJ, 623, 482
Trilling, D. E., Brown, R. H., & Rivkin, A. S. 2000, ApJ, 529, 499
Udry, S., et al. 2007, A&A, 469, L43
Wyatt, M. C., et al. 1999, ApJ, 527, 918

Chapter 9: Results and Conclusions

This thesis provides an explication of the exoplanet system Gl 876, and as a result, leads to better understanding of M dwarfs and ultimately, of planet formation. The objectives to do so were accomplished through observations in spectral, optical and millimeter parameter space. While null results may not provide a more satisfying "eureka" moment, the constraints imposed by finding them can be equally instrumental to understanding an individual system and possibly its spectral class. Undeniably, finding nothing very much means something.

Most importantly, the broader impact of this work reveals how this system contributes to our understanding of both the M dwarf population and the exoplanet population. The specific knowledge gained about Gl 876 has added to the scant body of knowledge available about the formation of planets in M dwarf systems. It also improves the understanding of what one may expect to find there, as increasing detections take place. This characterization of Gl 876 is integral to an initial census of M dwarfs meant to detect and describe their very low mass companions. The goal will be to constrain models describing how M dwarfs behave as parents of planets. Having constrained Gl 876, this thesis begins those steps in concert with others for the larger population.

Plans have been made to expand on the work begun here to improve our knowledge of similar, interesting examples. The main body of this work lays out several real scientific enhancements to the knowledge of Gl 876, red dwarfs, exoplanets, and their detection. Key among these are:

(1) The inclination of this system is now constrained from near 90° to ~50° due to photometric, spectroscopic, and millimeter-continuum analyses (Chapters 5, 6 and 8).

(2) A resultant mass limit is assessed, beyond the mass (sin i), which more tightly constrains Jovian planets "b" and "c" from $1.935 \pm 0.007\ M_{Jup}$ and $0.619 \pm 0.005\ M_{Jup}$, to $2.530 \pm 0.008\ M_{Jup}$ and $0.790 \pm 0.006\ M_{Jup}$. For terrestrial planet "d" the mass is further constrained from $5.89 \pm 0.54\ M_{Earth}$ to 7.53 ± 0.70

M_{Earth}. This keeps the latter among the lowest mass planets detected to date.[133] (Chapters 6 and 8)

(3) An upper limit of 0.0006 ± 0.0001 M_{Earth} for the dust mass within the system was established, which supports the hypothesis that Jovian planets orbiting close to red dwarfs sweep dust out of the system (Chapter 8).

(4) The low dust mass limit set infers a lack of dust-producing planetessimals in the system, which is consistent with the low metallicity of this system. If other reasons do not show cause for the low dust mass, certainly a low-metallicity proportionality to the dust mass is shown to be a viable cause (Chapter 8)

(5) Proved that novel network-distributed, targeted photometric detection schemes can produce rigorously scientific data, which might otherwise escape the scientific community owing to an otherwise lack of sufficient "eyes-on", dedicated instrumentation for these particular objects. Insight into the techniques and procedures pioneered provide additional opportunities to continue globally distributed, targeted surveys (Chapters 4, 5, 6 and 7)

(6) Provided the above signposts to the astronomical community as early as 2005, which indicate that M dwarfs would be the best place to seek and detect terrestrial planets in HZs (habitable zones) about their parents. This affirmation in the 2006 publication in the *Astrophysical Journal*, and the latest accepted for publication in *Astronomical Journal*, has proven to bear out. Six new planets orbiting M stars have been detected in the last 12 months, to include one orbiting in the HZ of red dwarf Gl 581 (Chapters 6 and 8).

(7) Proved that airborne video-rate photometry from the stratosphere was viable as an alternative photometric method to detect M dwarf exoplanets.[134] This device further showed that low-expense variants might prove to be useful across

[133] For reference, compare this to the planet "c" recently detected orbiting Gl 581. Gl 581c is estimated to be ~5.02 $M_{Earth}(\sin i)$. If this 'super-Earth' is eventually found to be inclined $i \leq 47.3^{N}$, its mass would be comparable or greater than Gl 876d. Gl 876's planet "d" not only still vies for diminutive status, the system is 1.57 pc closer.

[134] For TOPhAT this required transit flux depths to be above 5%.

a myriad of photometric studies requiring similar sensitivities. For its ingenuity of construction and its operational success, the Smithsonian Institute plans to include this innovative equipment in its archives (Chapter 4)

As discussed herein, the proposed efforts to continue study of M dwarf exoplanet systems does not end with writing this thesis. GEMSS Phase II expands on both the original Gl 876 transit campaigns and GEMSS Phase I which followed close behind. GEMSS Phase II will further constrain the greater population of M stars and describe their propensity to harbor anything from Jovians down to super-Earths. As shown here, even when GEMSS Phase II produces null results for a particular system that information enriches the red dwarf census and quantifies what that population may offer to the larger exoplanet census.

In parallel to such efforts as GEMSS Phase II, the author remains a principle acquisition and program manager of the Naval Observatory's space-borne astrometric satellite, called the Joint Milli-arcsecond Astrometric Pathfinder Survey, or J-MAPS system. The J-MAPS (or simply MAPS) program has been in technology development for almost 4 years, and in 2007, significant funding was appropriated for the satellite to be launched into a 900-km terminator orbit in 2013. While J-MAPS serves to fill a growing astrometric shortfall in precision celestial navigational requirements, for the exoplanet scientist it serves to enable a 1- to 3- milli-arcsecond astrometry capability, which allows the observer discern gravitational wobbles of Jovian planets about nearby M stars. More importantly, J-MAPS observations will constrain what should be observed by larger, future missions, and it has begun to path-find advanced technologies for them at its more 'palatable' mission cost. J-MAPS will also initiate a V >12 astrometric reference tie-frame that will underpin a wide assortment of astronomical programs, to include all methods of exoplanet detection and observation. As its acronym-derived name infers, MAPS will provide the back-drop as well as the principle science for much of the exoplanet science in the coming two decades. Appendix K describes J-MAPS further, and offers the reader a 2007 white paper by the principles to the U.S. National Science Foundation's Exoplanet Task Force (ExoPTF).

The radio interferometric observations of Gl 876 described in Chapter 8 provided a non-optical window through which to view that system and disclosed key aspects yet-defined

for Gl 876, such as the system's inclination (thus mass), composition, dust mass, and possible evolution. Building on this pan-spectral approach, the author also recently observed a different but equally curious exoplanet system, HD 80606. The G5 star HD 80606 system is part of a visual binary and has a highly eccentric planet orbiting it every 112 days. HD 80606 was observed from 2007 November 23 to 25, using the VLA operating at 327, and 1400 MHz. During that time, the planet "b" passed within ~0.03 AU during its periastron. At the same time, a collaborating team observed the passage in the infrared with the Spitzer Space Telescope. These radio observations are expected to reveal the level of non-thermal, magnetic, and exo-Auroral activity produced as the two bodies nearly grazed. At the same time, the Spitzer observations should reveal possible atmospheric interactions along with possible primary and secondary transits of the planet.[135] Appendix L discusses this developing project further, and contains the VLA proposal upon which the 2007 observations were based.

As became evident in the course of this research, no single exoplanet detection method can fully constrain a system. The results presented here required three methods to constrain models of Gl 876 and its planets. On-going and future observations will have to take similar multi-disciplinary approaches to completely constrain them. For Gl 876 and M dwarfs at large, new observational approaches improved the data collection possibilities. These niche approaches garnered the results expounded upon herein and expanded the tools available to describe other M star systems. Making clear those yet-to-be understood parameters for a system such as Gl 876 has been a journey of scientific discovery which is only partly complete. To achieve the fuller understanding, one must continue to inexorably heed the memorable words long-attributed to Rudyard Kipling, "I keep six honest serving-men (They taught me all I knew); their names are 'What and Why and When And How and Where and Who'." That sentiment conveys what GEMSS seeks, which is to answer both human curiosity, and deliver a more complete characterization of the nearby red dwarfs. The final achievement will be to understand their propensity to harbor earth-massed, habitable planets.

[135] For those interested, a popular discussion of these IR and radio results will be ongoing and is found at http://oklo.org/?cat=3

From what is known now, the single-most likely place to detect nearby Earth-like exoplanets is in orbits around the M dwarfs that populate the solar neighborhood, such as the multi-planet system around Gl 876. Playing a role in such discovery efforts as enjoyed herein is innately rewarding. It appeals not just to the scientific mind, but to the explorer pressing forward within each person, to...

> *"... not only to go farther than any one had been before, but as far as it was possible for man to go ..."*
>
> - James Cook, *Royal Navy, Great Britain*